TECHNISCHE UNIVERSITÄT WIEN
Vienna University of Technology

CERN

D O C T O R A L   T H E S I S

Tomographical reconstruction of the horizontal phase space of a 3rd order slow resonant extracted proton beam of the MedAustron synchrotron

submitted to the Atominstitut of the Vienna University of Technology
in cooperation with EBG MedAustron and CERN

under supervision of
Prof. Dipl.-Ing. Dr.techn. Michael Benedikt

by
Dipl.-Ing. Dipl.-Ing. Alexander Wastl

Muldenweg 14
A-9170 Ferlach, Austria

Ferlach, February 29th 2020

MedAustron
Ion Therapy Center

Abstract

The aim of this thesis is to determine the non-Gaussian particle distribution in the horizontal phase space extracted from a synchrotron accelerator via a slow resonant extraction process referred to as 'bar of charge'. A major issue associated with this undertaking is that a direct measurement of the phase space is not possible, which in this study was circumvented by using tomographical reconstruction techniques. The required input data for the reconstruction algorithms (for simulations and measurements) were gathered by making use of the Phase Shifter Stepper module – a dedicated magnet setup designed at CERN for transverse phase space adjustments, implemented in the high energy beam transfer line at MedAustron. To date, no other accelerator facility has hosted such a module or has implemented it in such a way. Thus, the empirical evidence of the module's working concept is also presented here.

The first section of this paper presents the results of tracking simulations relating to questions regarding an appropriate measurement procedure, suitable reconstruction settings, meaningful particle distribution quantification parameters and useful data correction mechanisms. The second section presents the results of measurements performed with 250MeV proton beams and the relevant tomographical reconstructions provide visual evidence of the 'bar of charge' and confirm the theoretical descriptions of the slow extraction process. Furthermore, the applicability of the procedure (combination of adapted Phase Shifter Stepper working concept and tomographical reconstruction) is demonstrated by comparison of simulated and measured particle distributions. Finally, the impact of the measurement devices used on the results, limitations of the method itself as well as an outlook on time resolved reconstruction are discussed.

Results of this thesis have been presented at the 6th *International Particle Accelerator Conference* in May 2015[1], the Slow Extraction Workshops 2016[2] and 2017[3] as well as the ABTEF seminar at CERN 2018.

Acknowledgements

First of all, I would like to express my sincere gratitude to my supervisor Prof. Michael Benedikt for the continuous support during my studies, his patience and the opportunity to come to CERN. This incredible experience introduced me to the world of accelerator physics, a field of research and work I found many friends in and am happy to continue working.

A special thanks to EBG MedAustron for providing me with the necessary machine time to perform the measurements used in this thesis. A very warm thanks to my colleagues at MedAustron for encouraging me also during more difficult periods. I am very grateful to Adriano Garonna, Fabio Farinon and Sebastian Nowak for many fruitful discussions, the enjoyable times we had in the office and proofreading of this document.

Furthermore, I want to thank Ulrich Dorda on who's idea the topic of this research bases and for the numerous invaluable discussion on accelerator physics and python - especially in the beginning of this endeavor.

Finally, my deep and sincere gratitude to my family for their continuous help and unrestricted support. To my parents for giving me the opportunity to explore new directions, sharing their experience and expertise and putting me on the right track. And of course to my wife Manuela and my wonderful children Elena and Elias for selflessly encouraging me, their countless sacrifices to help me get to this point and their unconditional love. Without them, I would not be where I am today.

Contents

i

Contents

List of Figures

List of Tables

1. Introduction and Scope

In modern cancer treatment the therapy with hadrons has become a routinely used method especially regarding the treatment of tumors close to critical organs or in pediatric care. Those particles show an advantageous behavior when propagating through tissue (see Figure 1.1): the energy deposition is focused in a dedicated penetration depth determined by the initial energy of the particle while the collateral damage created by energy deposition in the entrance channel or other surrounding tissue is reduced. This behavior is referred to as 'Bragg peak' [10].
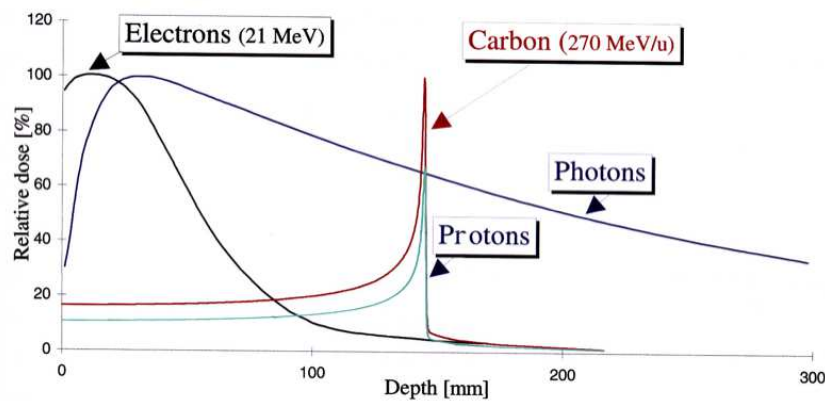
Figure 1.1.: Penetration behavior of different types of radiation showing a Bragg peak for protons and carbon ions [4]

For protons the required kinetic energies of up to 230 MeV can be achieved by e.g. cyclotron particle accelerators. However, for other light ions (but still including protons) the most frequently used type of accelerator is the synchrotron operated with a slow extraction scheme in order to achieve a quasi-continuous particle beam towards the patient [11][12][13][14][15]. Different accelerator layouts have been designed and implemented while the beam extraction typically is realized via particle excitation at the third-integer resonance. The measurements for this thesis have been performed at the MedAustron Ion Therapy facility [16] in Wiener Neustadt, Austria, where a betatron core is used to accelerate the beam into the resonance.

Due to the nature of the extraction process the particles in the horizontal phase

space (x, x')[1] of the extracted beam towards the irradiation areas populate a narrow rectangular-like, non-Gaussian shape known as *bar of charge*. Typically this phase space distribution is not directly measurable though still of interest e.g. for the qualification of the extraction process or as beam characterization for further simulations[18].

The MedAustron High Energy Beam Transfer line (HEBT) hosts a dedicated section to rotate this bar of charge which in the PIMMS[11][12] concept is used to adjust the horizontal spot size of the beam in the irradiation room isocenter[19]. For this thesis this section is used to rotate the beam by 180° and perform beam profile measurements from various angles using a scintillating fiber grid monitor (SFX). Based on this compilation of data the horizontal phase space can be computed via a tomographical reconstruction method similar to a CT or PET in medical imaging [2].

The following chapters will describe the process of the slow resonant extraction from the MedAustron synchrotron, the tomographical methods used to reconstruct the horizontal HEBT phase space, the identification of appropriate measurement settings found via simulations as well as the measurements itself and the comparison to the simulation. The **scope** of this thesis is to

1. empirically proof the 'bar of charge' concept

2. demonstrate the method of transfer line phase space determination by tomographical reconstruction applied on measurement data achieved by phase space rotation via the Phase Shifter Stepper concept.

1.1. State of the Art overview

Tomographical reconstruction has become a beam diagnostic technique used frequently especially in Free Electron Laser (FEL) facilities[20][21], synchrotron accelerators [22][23] but also transfer lines[24][25][26][3]. Considering the tomography in transfer lines of hadron accelerators, two methods are commonly used:

1. Multiple monitors installed in different positions of the transfer line with quadrupole magnets in between. The magnets rotate the particle distribution in phase space and via the monitors beam distribution profiles are recorded. Reggiani et al[28] showed that via this setup and the reconstruction algorithm

---

[1]The coordinate system definition for this thesis is following the MADX convention.[17]

[2]While in a CT scanner the patient remains static and the detector is moved around the patient, in this setup the monitor is static and the beam is rotated. For the reconstruction algorithm this is no difference.

[3]Stratakis et al[27] showed that at a FEL using an optimized setup an error between simulation and measurement of less than 10% can be achieved.

MENT[29][30][4] the phase space of a proton beam extracted from cyclotrons and synchrotrons can be reconstructed.

2. One or multiple quadrupoles are used to rotate the particle distribution in phase space on a single monitor downstream the magnets. Typically in such scenarios not only the phase advance is changed but also the beta functions are scaled for the various quadrupole settings. This approach is used for this thesis.

1.2. MedAustron

MedAustron is a synchrotron based cancer treatment and research facility located in Wiener Neustadt, Austria. For clinical applications proton beams up to 250MeV as well as carbon ion beams up to 400MeV/nucleon[5] can be provided to five different beam lines [6] while for nonclinical research proton beams up to 800MeV are available in a dedicated irradiation area[31][32][33]. The accelerator layout bases on the CERN PIMMS study and the first patient has been treated in December 2016.

The injector hosts up to four Electron Cyclotron Resonance (ECR) ion sources, a Radio Frequency Quadrupole (RFQ) and an Inter-digital H-mode linear accelerator (LINAC) with an output energy of 7MeV/nucleon. In the following the multiturn injection fills the particles into the 77.6m circumference synchrotron which hosts a linear lattice composed of 16 dipoles powered by a common power supply as well as 24 quadrupoles combined in two focusing and one defocusing family. Four sextupoles placed in dispersive section of the lattice are used to control the chromaticity while a dedicated (resonant) sextupole in a dispersion-free section is used to drive the slow extraction process.

By increasing the magnetic fields of the magnets and synchronously accelerating the particles with a wide-band Radio Frequency cavity (RF), the beam energy is increased to the desired extraction (flat top) energy. After being extracted (chapter 2.2) the particles traverse the High Energy Beam Transfer line (HEBT)[34] towards the irradiation rooms[35]. The design foresees $1x10^{10}$ protons and $4x10^8$ C^{6+} ions in the irradiation room per pulse extracted in a time window between 0.1 - 10 seconds.

Figure 1.3 shows a flattened synchrotron layout on top indicating the position of the resonant sextupole (MR08000MXR), the electrostatic extraction septum (MR14000ESE) as well as the magnetic extraction septum (EX00000MST). The bottom charts show the horizontal and vertical β-functions and the horizontal dispersion.

---

[4]The distribution function matching best to the few profiles measured is identified by evaluating the maximum entropy.

[5]Those energies correspond to a penetration depth in water of about **36**cm.

[6]Three horizontal fixed beam lines, one vertical fixed beam line as well as a rotating gantry.
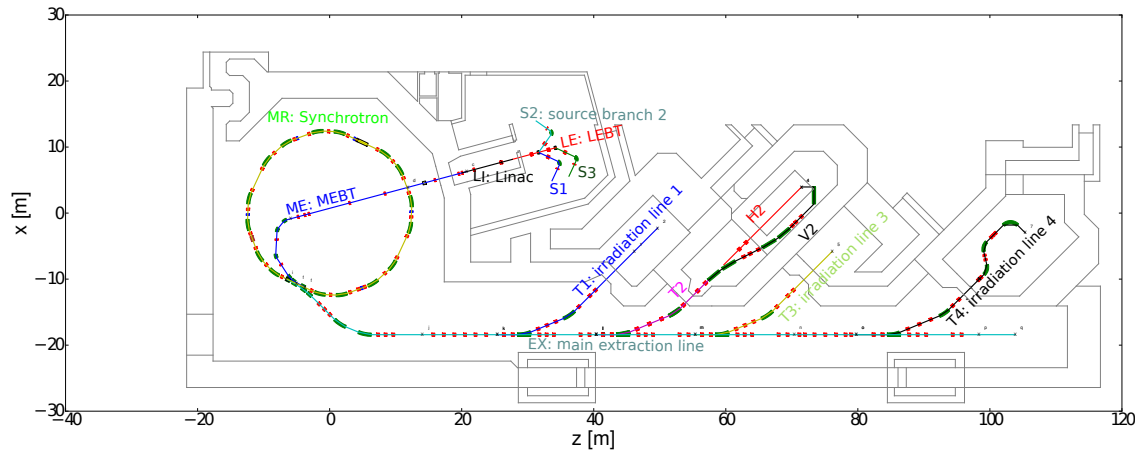
Figure 1.2.: Layout of the MedAustron ion therapy accelerator[5]
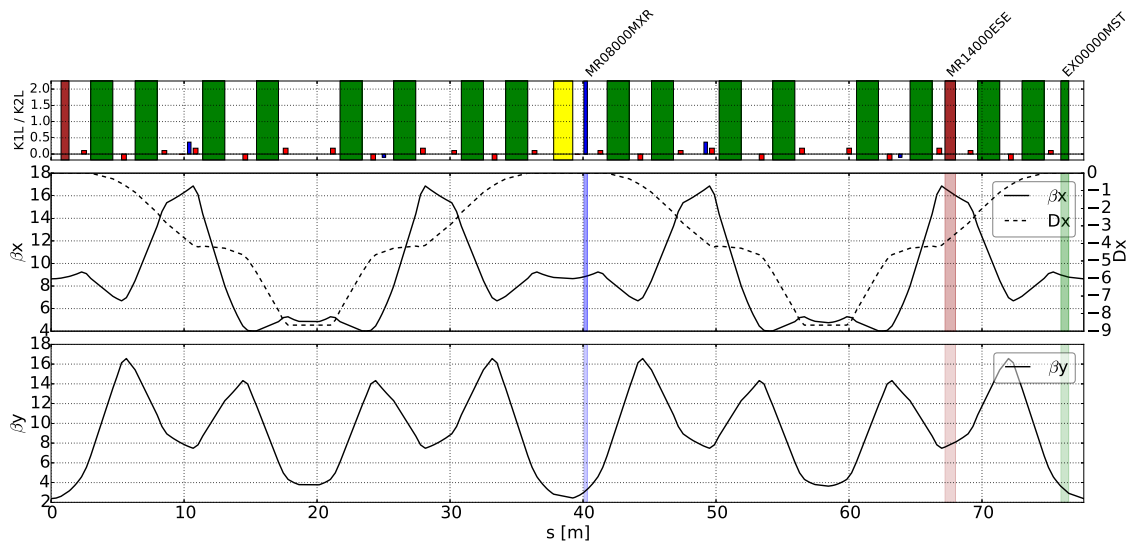
Figure 1.3.: Beam optics of the synchrotron

2. Theoretical background

This chapter describes selected topics of accelerator physics (section 2.1)[7], introduces the basic concepts of resonant slow extraction (section 2.2) and the 'bar of charge', pictures the phase shifter stepper concept (section 2.3) and gives an overview of tomographical reconstruction techniques (section 2.4) to establish a context for the content of this thesis.

2.1. Accelerator physics

2.1.1. Transverse motion

The transverse motion of particles traversing through the linear lattice of a synchrotron can be parametrized and described by a pseudo harmonic oscillation[43][36]:

$$z(s) = A\sqrt{\beta(s)}\ \cos\mu(s) + B \tag{2.1}$$

with

$$\mu(s) = \int_0^s \frac{ds}{\beta(s)} \tag{2.2}$$

The constants A and B are determined by the initial coordinates of the particle. The *beta amplitude function* $\beta(s)$ and therefore also the *phase advance* $\mu(s)$ are defined by the optics of the lattice. Further parameters that can be deduced from the beta function are:

$$\alpha(s) = -\frac{1}{2}\frac{d\beta}{ds} \tag{2.3}$$

$$\gamma(s) = \frac{1+\alpha^2}{\beta} \tag{2.4}$$

---

[7]For detailed descriptions and mathematical proofs the reader is referred to specialized literature[36][37][38][39][40] and lectures of dedicated programs like CAS[41] or USPAS[42].

These three parameters (α, β, γ) are called *Courant-Snyder parameters* or *Twiss functions*. Another important parameter in transverse optics is the phase advance over one revolution in the synchrotron called the *(betatron) tune* Q $(2\pi Q_z = \Delta\mu)$. It describes the number of betatron oscillations around the closed orbit per turn.

Extracting and eliminating the phase term of equations 2.2 and 2.3 leads to the definition of new *normalized coordinates*

$$Z(\mu) = A\cos(\mu + B) = z(s)\frac{1}{\sqrt{\beta}} \qquad (2.5)$$

$$Z'(\mu) = -A\sin(\mu + B) = z'(s)\sqrt{\beta} + z(s)\frac{\alpha}{\sqrt{\beta}} \qquad (2.6)$$

This *Floquet transformation* is linear and therefore it is often convenient to rewrite it in matrix form

$$\begin{pmatrix} Z \\ dZ/d\mu \end{pmatrix} = \begin{pmatrix} 1/\sqrt{\beta} & 0 \\ \alpha/\sqrt{\beta} & \sqrt{\beta} \end{pmatrix} \begin{pmatrix} z \\ dz/ds \end{pmatrix} \qquad (2.7)$$

$$\begin{pmatrix} z \\ dz/ds \end{pmatrix} = \begin{pmatrix} \sqrt{\beta} & 0 \\ -\alpha/\sqrt{\beta} & 1/\sqrt{\beta} \end{pmatrix} \begin{pmatrix} Z \\ dZ/d\mu \end{pmatrix} \qquad (2.8)$$

Eliminating the phase advance μ from equations 2.5 and 2.6 leads to an invariant describing an ellipse in (real) phase space (z,z') and a circle in normalized phase space (Z, Z') (see Figure 2.1):

$$\frac{\epsilon}{\pi} = A^2_{norm} = \gamma z^2 + 2\alpha z z' + \beta z'^2 = Z^2 + Z'^2 (= constant) \qquad (2.9)$$

The constant ϵ equals to the area covered by the ellipse (in real and normalized phase space) and for a single particle is referred to as *single particle emittance*. The shape of the ellipse varies for different locations in the lattice while the area remains constant[8].

---

[8]The emittance does change e.g .in the presence of space charge or if the particle is being accelerated ('adiabatic damping'). In a plain linear lattice however the area remains constant (=Liouville's theorem).

6

real phase space

normalized phase space
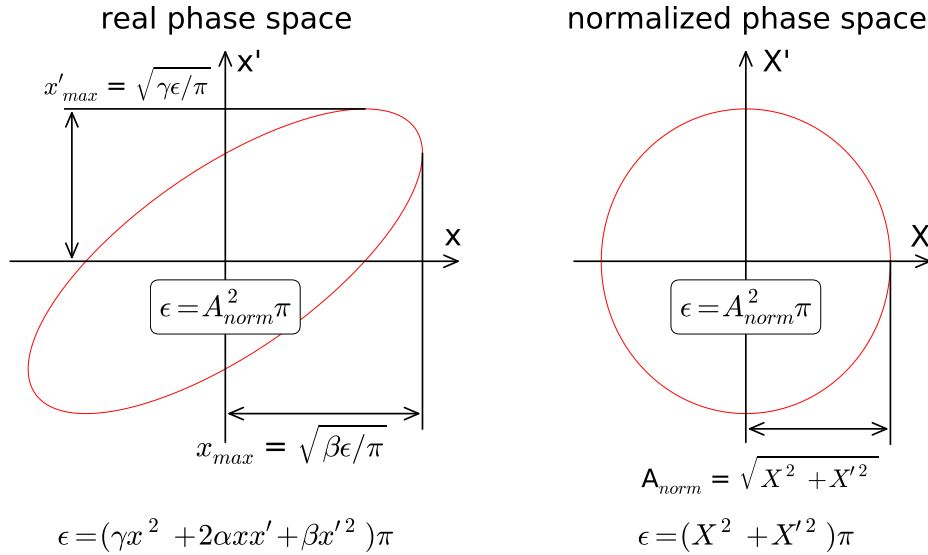
Figure 2.1.: Transverse real and normalized phase space

2.1.2. Dispersion and Chromaticity

Equation 2.1 describes the motion of an on-momentum particle through the lattice oscillating around the *central* or *reference (closed) orbit*[9]. A particle with a relative momentum shift $\delta p/p = (p_{part.} - p_0)/p_0$ with respect to the reference particle oscillates around a shifted orbit ($=design\ orbit$). To first order and only small $\delta p/p$ this shift is a product of the the momentum deviation and *dispersion function D(s)* created by dipoles.

$$\Delta x(s) = D(s)\frac{\delta p}{p_0} \tag{2.10}$$

$$\Delta x'(s) = D'(s)\frac{\delta p}{p_0} \tag{2.11}$$

Furthermore, also the tune of the particles are affected by their momenta as the focal strength of the quadrupoles in the linear lattice are dependent on the particle momentum. The correlation between the tunes of an off-momentum and an on-momentum particle is called *chromaticity* Q'_z.

$$Q'_z = \frac{\Delta Q_z}{\delta p/p_0} \tag{2.12}$$

---

[9]An on-momentum, on-axis, zero beta amplitude particle passing through the optical axis of the lattice components is referred to as *reference particle*.

2.2. Slow extraction

In order to extract the particles slowly from the synchrotron (hundred thousands of turns), an often used approach is to drive the particles into a resonance in a controlled manner. Assuming the particle motion as a harmonic oscillation, a resonance can be described as a perturbation with a harmonic coinciding with the eigenfrequency (=single particle tune) of the particle[37]. The particle will become unstable, increase its betatron amplitude and eventually be 'lost' into the extraction channel.

2.2.1. Third integer resonance

For a non-linear perturbation represented by a sextupole the third integer resonance is excited. Figure 2.2(a) shows the process of amplitude increase schematically: A particle with a betatron tune (=eigenfrequency) meeting the condition $3Q_H =$ integer and a non-zero emittance receives a kick passing through the sextupole. As indicated in Figure 2.2(b) all particles with $X \neq 0$, $X' = 0$ are exposed to a kick in the same direction. The blue points in Figure 2.2(a) represent six consecutive turns: when passing through the center of the sextupole, the particle receives no kick while in all other cases it does and therefore increases its amplitude (increasing the radius of the green circle in normalized phase space)[10] .

(a) Amplitude growth of a particle with a fraction tune of $1/3$ caused by a sextupole[6]

(b) Schematic of field lines and Lorentz force vectors for a normal sextupole[44]
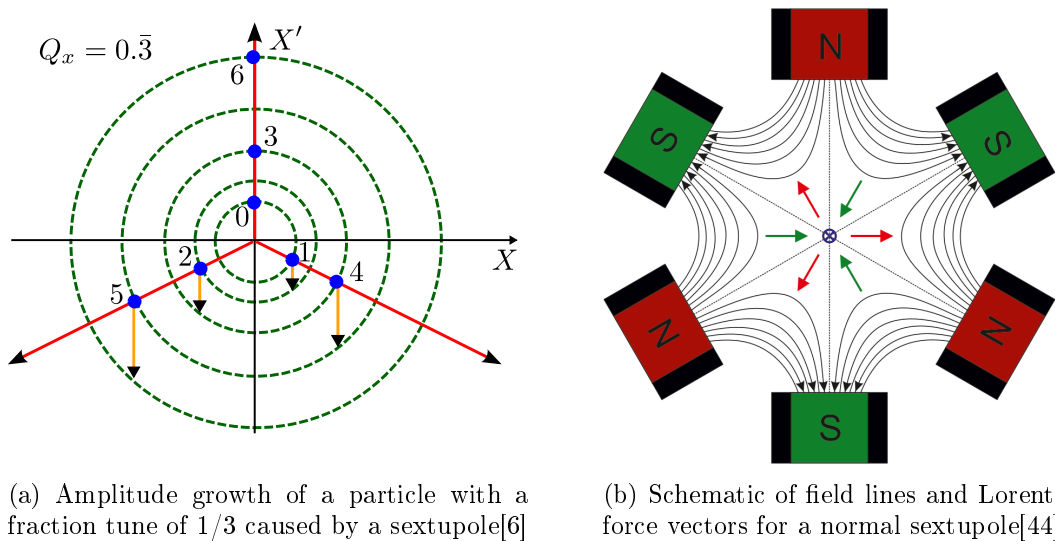
Figure 2.2.: Sextupoles create a non-linear perturbation and therefore resonances that can be used to slow extract the particles.

---

[10]Point 1 and point 4 represent the same particle three turns later with increased amplitude. If the amplitude has increased to a certain point, between point n and point n+1 there is an electrostatic septum installed guiding the particle into the extraction channel.

If the resonance condition is not met, the particle would also receive kicks in the $X' > 0$ half of this chart kicking the particle 'back'. Over many turns, the area of the ellipse does not increase while the shape might get deformed.

2.2.2. Extraction preparation

In the case of the MedAustron accelerator, the process of the extraction is prepared the following way: the horizontal lattice tune Q_H is 5/3 which is exactly the resonance condition of a sextupole while Q_V is 1.789 and therefore in safe distance to any resonance. The central beam momentum is off-momentum at flat top by -3.5E-3 while the momentum spread of the particles within the beam is ± 2.0E-3. Because of the chromaticity Q'_H of about -4.0 the beam tune is slightly above the resonance and the beam is waiting to be extracted.[11] Only now the resonant sextupole is ramped to excite the third integer resonance strongly.[12] These steps are visualized in the Steinbach diagram in Figure 2.3(a) showing the ramping of the resonant sextupole.

(a) Ramping resonant sextupole   (b) Ramping resonant sextupole
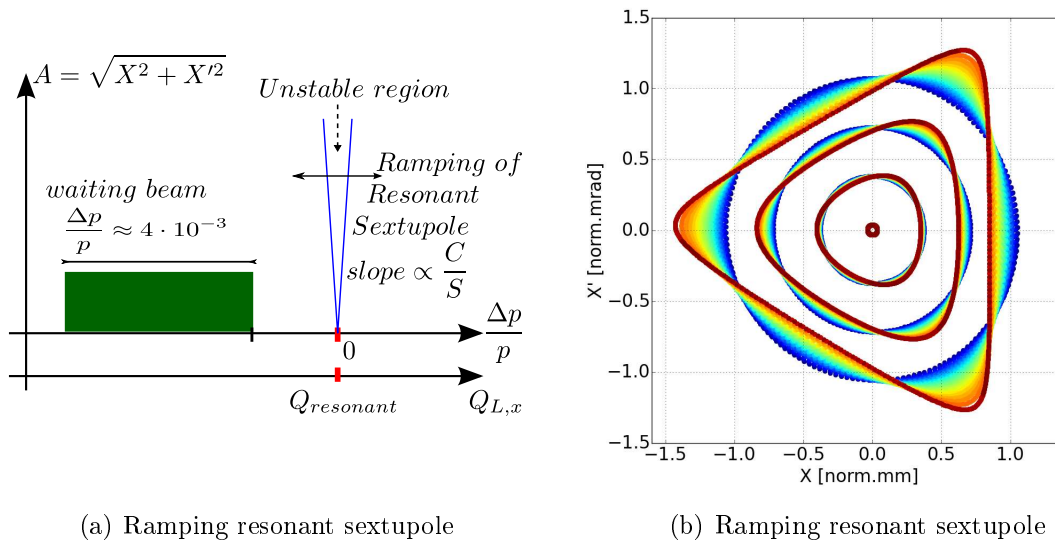
Figure 2.3.: Steinbach diagrams showing the last preparatory steps before extraction[6]

Mathematically, particles passing through a simplified thin lens sextupole receive the following kicks[13]:

---

[11]Because of the dispersion $D_H(s)$ the beam is also shifted in position. Only in locations where the $D_H = 0$ like at the resonant sextupole the design orbit is equivalent to the reference orbit.

[12]Because of it being located in a dispersion-free region ($D_z = D'_z = 0$) this ramp in first order doesn't affect the chromaticity.

[13]The following semi-qualitative description of the slow extraction provides only an overview of the

$$\Delta x' = \frac{1}{2} l_s k' (x^2 - y^2) \tag{2.13}$$

$$\Delta y' = -l_s k' xy \tag{2.14}$$

with l_s as the magnet length and k' as the normalized sextupole gradient.

$$k' = \frac{1}{|B\rho|} \left(\frac{d^2 B_z}{dx^2} \right) \tag{2.15}$$

In normalized coordinates, the kicks are described as

$$\Delta X' = S \left(X^2 - \frac{\beta_y}{\beta_x} Y^2 \right) \tag{2.16}$$

$$\Delta Y' = -2S \frac{\beta_y}{\beta_x} XY \tag{2.17}$$

with S as the normalized sextupole gradient

$$S = \frac{1}{2} \beta_x^{3/2} l_s k' \tag{2.18}$$

Figure 2.3(b) shows the effect of the resonant sextupole ramping in normalized phase space at the location of the resonant sextupole for four particles of different emittance. The blue circular movement of the particle gets deformed towards a triangular shape if the ramping is performed adiabatically (=slow with respect to the revolution time).

Assuming that Y is small with respect to X (especially concerning that the extraction takes place in horizontal plane X) leads to the equations

$$\Delta X = \Delta Y = \Delta Y' = 0 \ \ and \ \ \Delta X' = SX^2 \tag{2.19}$$

Based on the assumptions so far, the motion of a horizontal particle with a particle tune close to the third integer resonance ($6\pi\delta Q$ = modified tune distance ζ[14]) can

---

process. As the MedAustron accelerator represents an implementation of the CERN PIMMS study, detailed descriptions can be found there [11][12][8][45]

[14]Typically in the literature the letter ϵ is used for the modified tune distance as well as for the emittance. For clarity in this document ζ is used for the modified tune distance.

be approximated by a simplified *Kobayashi Hamiltonian*[46] describing the motion in a linear lattice with a sextupole perturbation[15]:

$$H = \underbrace{\frac{\zeta}{2}(X^2 + X'^2)}_{\text{unperturbed harmonic oscillation}} + \underbrace{\frac{S}{4}(3XX'^2 - X^3)}_{\text{sextupole perturbation}} \tag{2.20}$$
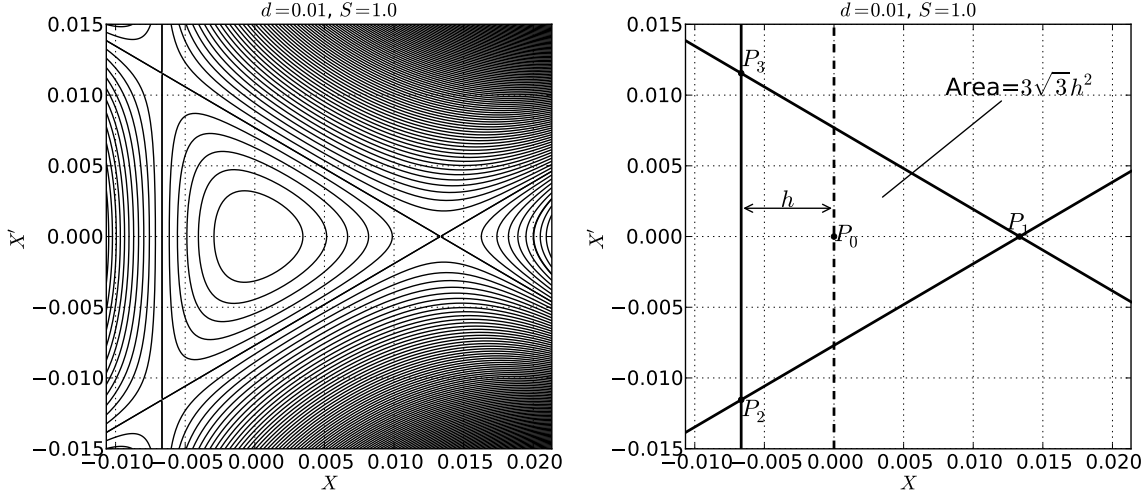
Figure 2.4.: Left: Particle trajectories in normalized horizontal phase space (S = 1.0, ζ = 0.01). Right: The stable triangle defined by the separatrices and fixed points P_0-P_3 ($h = \frac{2\zeta}{3S}$)[7]

In case $H = (2\zeta/3)^3/S^2$ the Hamiltonian can be factorized into three lines referred to as separatices describing the borders between stable and unstable regions in normalized phase space (see Figure 2.4). Moving along the ring in normalized phase space rotates the orientation of the triangle but the size indeed remains the same.

$$\left(\frac{S}{4}X + \frac{\zeta}{6}\right)\left(\sqrt{3}X' + X - \frac{4\zeta}{3S}\right)\left(\sqrt{3}X' - X + \frac{4\zeta}{3S}\right) = 0 \tag{2.21}$$

The area of the largest stable triangle is called *acceptance*

$$acceptance = \frac{48\pi\sqrt{3}}{S^2}(\delta Q)^2\pi \tag{2.22}$$

Stable particles therefore have to fulfill

---

[15] Typically there are multiple sextupoles installed in a synchrotron. For the description of the extraction process the strengths can be combined to one *virtual sextupole*[11].

$$\epsilon_{stable} = \sqrt{X^2 + X'^2}\pi = A_{norm}^2 \pi \leq acceptance \tag{2.23}$$

This results in the following equation for the *resonance line*:

$$A = \sqrt{48\sqrt{3}\pi}\left|\frac{\delta Q}{S}\right| = \sqrt{48\sqrt{3}\pi}\left|\frac{Q'}{S}\right|\left|\frac{\delta p}{p}\right| \tag{2.24}$$

This is visualized in Figure 2.5(a) by the two blue lines: particles below the lines are stable while particles above are unstable.

(a) Waiting beam with strong resonance

(b) Driving the beam into the resonance
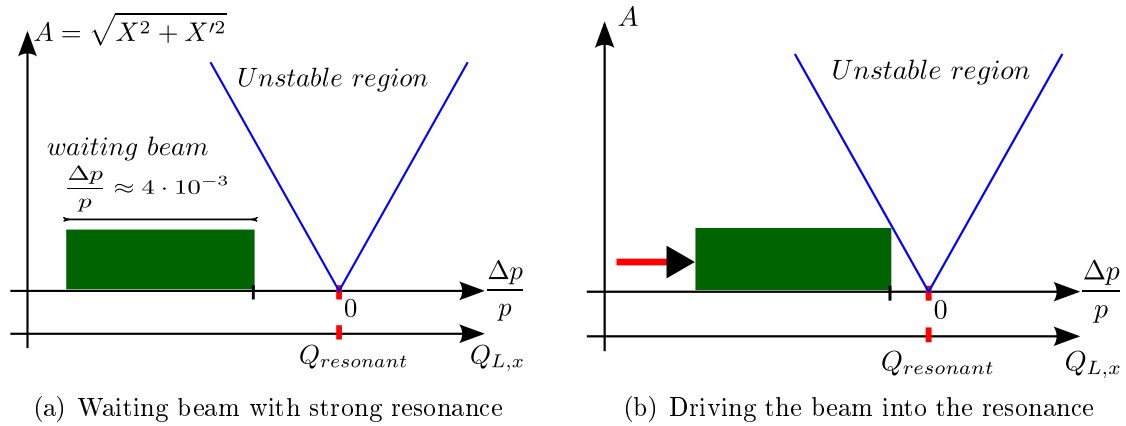
Figure 2.5.: Steinbach diagrams just before extraction[6]

So far all particles are stable and the beam is 'waiting' to be extracted. At MedAustron, the selected mechanism of driving the beam into the unstable region (resonance) is by accelerating the entire beam with an inductive component called *betatron core*[16]. Figure 2.5 graphically shows the effect of this device: the entire beam is moved towards the resonance.

2.2.3. Extraction

Due to the driving mechanism stable particles will at some point reach the resonance line and become unstable. In Figure 2.4 the particles move from the so far closed trajectories inside of the stable triangle (set up by the three separatrices) towards the open trajectories outside. They start 'jumping' from one separatrix to the next returning every third turn but on a further outwards amplitude[17]. The change of

---

[16]The particles pass through this ring-shaped magnet along the central axis similar to a tunnel. The magnetic field of the device is ramped inducing an electric field parallel to the beam via Maxwell's 3rd equation $\nabla \times \vec{E} = -\frac{\delta \vec{B}}{\delta t}$

[17]Indeed the particle remains on the same separatrix all the time but as the fractional tune is 0.333, it seems the separatrices are stable in phase space and the particle is jumping.

position and angle over three turns are referred to as *spiral step* and *spiral kick* respectively:

$$\Delta R = \Delta X_3 = \zeta X_0' + \frac{3}{2} S X_0 X_0'$$

$$\Delta R' = \Delta X_3' = -\zeta X_0 + \frac{3}{4} S(X_0^2 - X_0'^2)$$

(2.25)
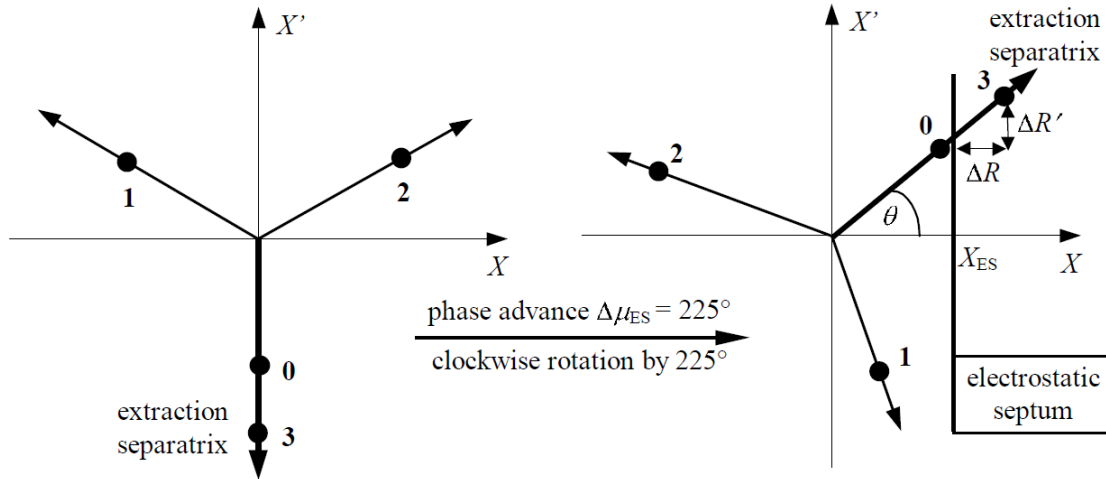
Figure 2.6.: Amplitude increase during the last three turns before extraction[8].

Figure 2.6 visualizes the increase of the amplitude caused by the kicks of the sextupole schematically. With the layout of the accelerator appropriately designed, the phase advance between the sextupole and the electrostatic septum is setup that only one separatrix is affected by the septum and the angle Θ is optimized. The particle at position 0 just passes the septum on the inside while three turns later (point 3) it 'jumps' behind the septum, receives a kick by the voltage and is deflected lightly (=change of X'). In Figure 2.7 this is shown graphically on the left side.

Typically the kick of the electrostatic septum is not sufficient to immediately extract the particle but a magnet is required. However, the kick the to-be-extracted particles have received from the electrostatic septum develops into a position offset when rotating the phase space by a dedicated phase advance μ as the particle travels further downstream. A magnetic septum well positioned where the created gap is sufficiently large can apply a strong kick to the particles and therefore represents the physical start of the High Energy Beam Transfer line (HEBT)[18].

So far only a single particle has been considered. An entire particle beam however consists of particles of various emittance and a certain momentum spread. As described by equation 2.24 and visualized in Figure 2.8(a) particles of certain emittance

---

[18]Optically the HEBT starts at the electrostatic septum.
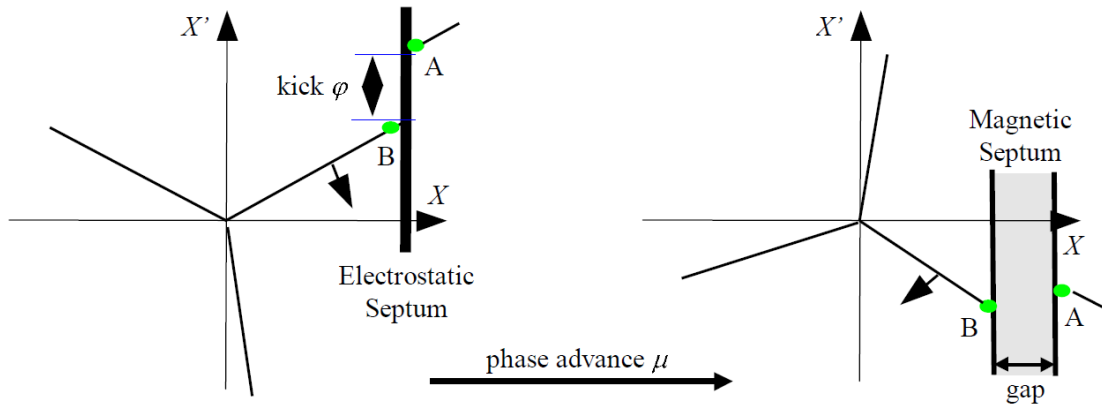
Figure 2.7.: Kick of the electrostatic septum in normalized phase space[8].

interact with the resonance line at a certain tune distance which via the chromaticity is equivalent to a momentum shift (equation 2.12).

In e.g. a dispersion-free region the geometric centers of the various triangles created by different emittances overlap. Consequently the separatrices of those triangles do not overlap (see Figure 2.9(a)) which indeed induces particle losses at a electrostatic septum placed in such a region as well as unfavorable beam characteristics. As shown in Figure 2.8(b) there actually is one accelerator and beam configuration that yields a minimum of particle losses[19].
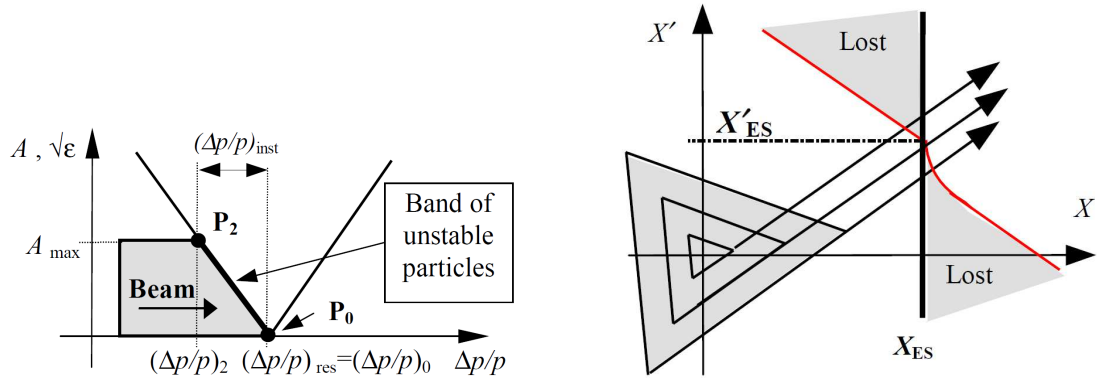
(a) Correlation of extracted momentum and particle emittance

(b) Electrostatic septum, Hardt-condition fulfilled

Figure 2.8.: Extraction considerations triggered by varying particle parameters within a beam[8]

---

[19]Due to the finite thickness of the electrostatic septum particles will be lost hitting it frontally. Furthermore due to the physical length of the septum particles just passing the septum entrance on the inside but with an outwards pointing angle will collide with the septum from the side. The same is true for extracted particles with an inwards pointing velocity vector. These two cases are represented by the 'lost' areas and the red line in Figure 2.8(b)

One way to optimize this situation is to superimpose the extraction separatrices of the various triangles at the electrostatic septum and minimizing the losses for this common separatrix. Figure 2.9(b) illustrates an example of such an arrangement of separatrices.

(a) Resonant Sextupole, $D_x = D'_x = 0$

(b) Electrostatic septum, Hardt-condition fulfilled
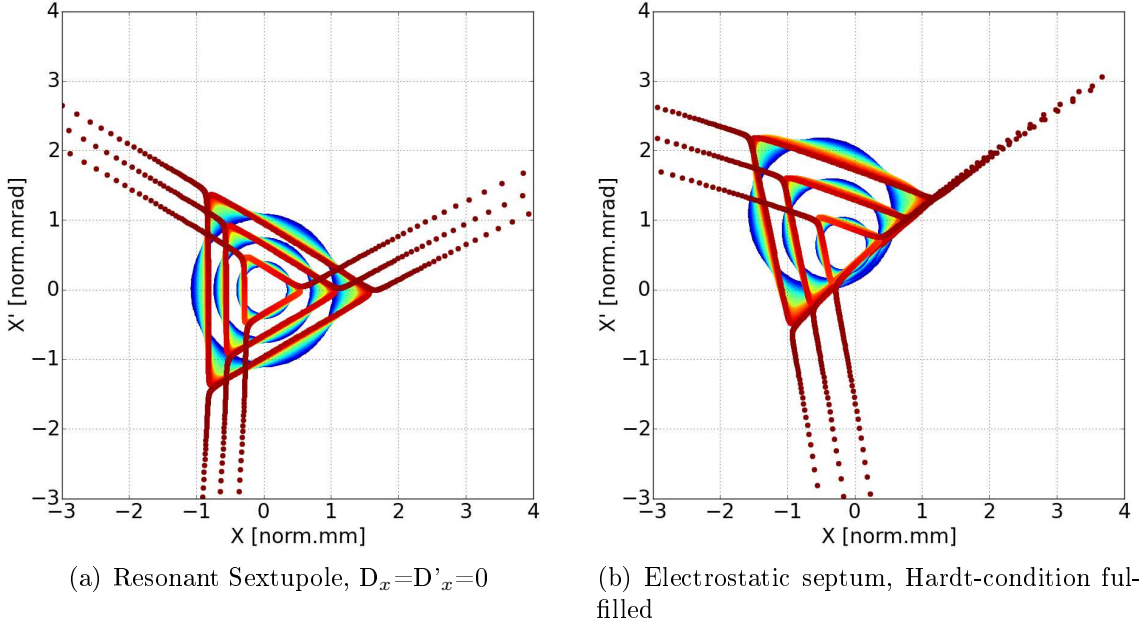
Figure 2.9.: Phase space movement of three particles being extracted at different locations in the synchrotron.

The superposition bases on the facts that particle emittance at extraction correlate to a momentum shift (as described above) and the presence of dispersion (=correlation of momentum shift and position/angle shift). Mathematically this results in the so called *Hardt condition*

$$D_n cos(\alpha - \Delta\mu) + D'_n sin(\alpha - \Delta\mu) = -\frac{4\pi}{S}Q' \qquad (2.26)$$

with (D_n, D'_n) as the normalized dispersion vector at the electrostatic septum, α as the orientation of the separatrix at the sextupole, $\Delta\mu$ as the phase advance from the sextupole to the septum and S as the normalized sextupole strength. The result of a simulation illustrated in Figure 2.10(b) clearly shows a non-Gaussian distribution referred to as 'bar of charge' (BoC). Due to higher order effects the superposition of all separatrices cannot be achieved perfectly.

(a) Last turns of multiple particles of common emittance; red = extracted beam segment (BoC)

(b) Details of the BoC incl. momentum distribution
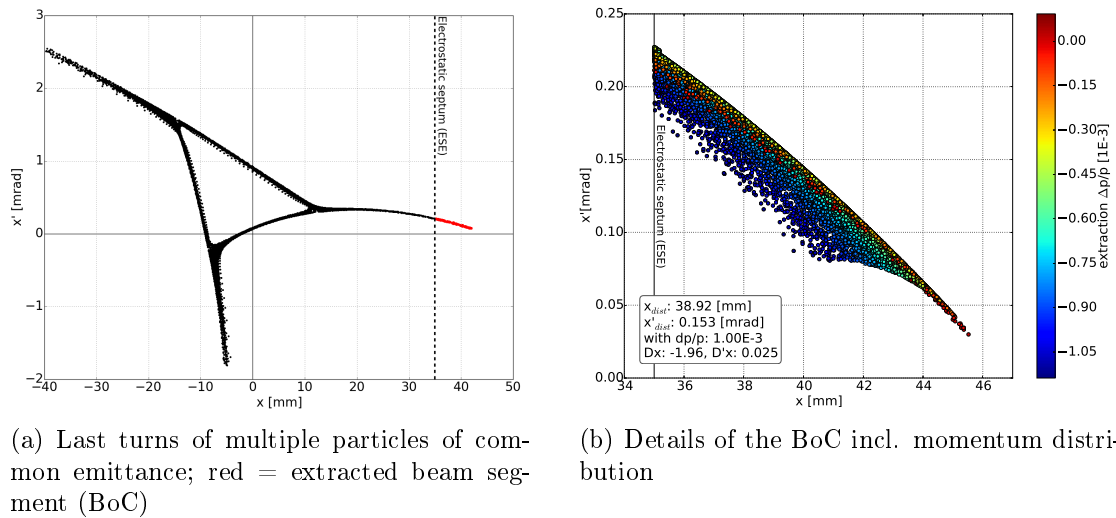
Figure 2.10.: Simulation of slow extraction resulting in the 'bar of charge (BoC)' (10000 particles)

Figure 2.11 shows some details of the extraction process resulting in the bar of charge. In both graphs the color-code reflects the emittance of the single particle. The left plot shows that high amplitude particles are extracted earlier in time and with a certain momentum shift than quasi-on-momentum particles with a very small emittance[20]. The right chart shows that small (almost zero) emittance particles jump behind the septum furthest while the spiral step of high emittance particles is shorter.
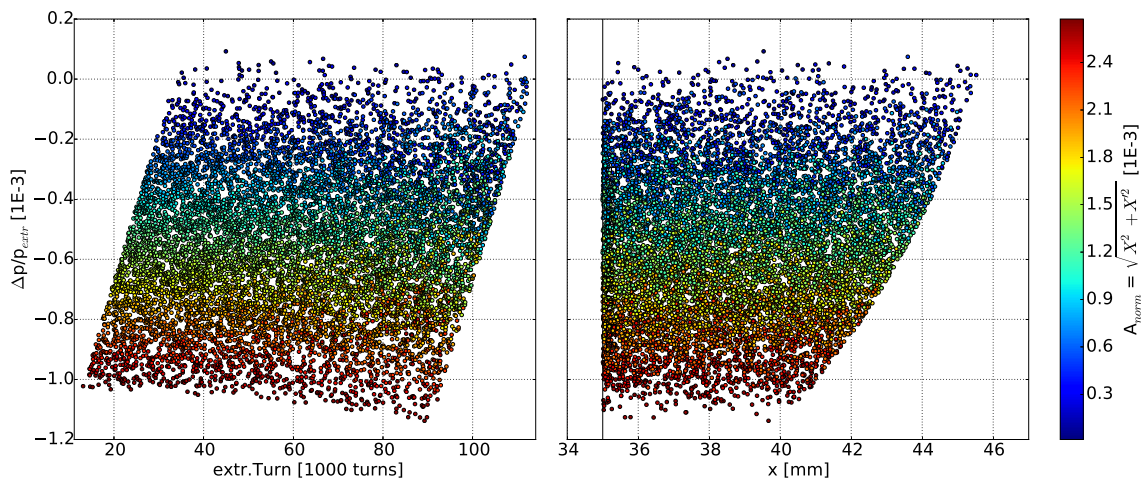
Figure 2.11.: Details of the extraction process leading to the BoC shown in Figure 2.10(b).

---

[20]For treatment the first part of the extracted spill (in this chart < 35000 turns) as well as the last part (>90000 turns) is dumped and not delivered to the patient.

2.3. HEBT and Phase Shifter Stepper (PSS)

Even though physically still part of the synchrotron the High Energy Beam Transfer line (HEBT) from beam optics perspective starts at the electrostatic septum. Due to the non-Gaussian nature of the bar of charge the precise description of the beam via the Twiss formalism is not correct[19]. As shown in Figure 2.10(b) the separatrices for on-momentum and off-momentum particles are almost parallel but shifted. This momentum dependent shift vector (x, x') of the geometric centers of the on-momentum and the $\Delta p/p = 1E-3$ separatrices divided by the momentum difference can be interpreted as an initial dispersion of the HEBT (see bottom corner of Figure 2.10(b)).

In order to be able to use standard beam optics computation algorithms it is comfortable to fit an (quasi-empty) ellipse to the bar of charge. As described above, the Twiss parameters of this ellipse will not describe the beam shape as illustrated in Figure 2.1. Therefore, at MedAustron, the (therefore freely selectable) initial Twiss parameters were determined with $\beta_x = 5m$ and $\alpha = 0$. This selection is still useful as for example at a position $n * 180$ degrees phase advance downstream the electrostatic septum, the width of the bar can be expected to be scaled with $x_{ESE} * \sqrt{\beta/\beta_{ESE}}$.

The first section of the HEBT downstream the extraction septa is setup as a dedicated functional module to close the dispersion (D_x=0) mentioned above and therefore optimize the beam shape at the isocenter as well as eliminate momentum-induced position offsets in most of the transfer line. The momentum rigidity[21] $B\rho$ of the HEBT is set up that the central momentum of all extracted particles is on-momentum[22]. Within the HEBT the momentum distribution therefore is not $[0, 1E-3]$ but rather $[-0.5E-3, 0.5E-3]$. The effect of the closed dispersion is illustrated in Figure 2.12(a): The momentum dependent (x, x') shift vector is zero and the geometric centers of the separatrices of all extracted momenta overlap. The bar further downstream therefore has a rather trapezoidal shape.

After the dispersion suppressor section, a straight section of the beam line hosting six quadrupoles is used to control the beam sizes in horizontal and vertical plane (see Figure 2.12(b)). In horizontal plane this is performed by the rotation of the bar of charge in phase space which in the accelerator is realized by adapting the horizontal phase advance at the end of this section keeping the horizontal beta function constant. As the beam size (width) is represented by the projection of the phase space onto the abscissa (position coordinate) a more upright standing 'bar' corresponds to a small beam size while a horizontally laying 'bar' corresponds to a large beam size.

---

[21] $B\rho = \frac{p}{q}$; originates from *centrifugal force = Lorentz force* and defines on-momentum p_0.

[22] On-momentum in the HEBT is shifted by $0.5E-3$ w.r.t the synchrotron.

In vertical plane the beam size can be adapted easily by scaling of the vertical beta function because of the Gaussian distribution in vertical phase space (not shown). Therefore this section is referred to as the 'Phase Shifter Stepper (PSS)'[11].
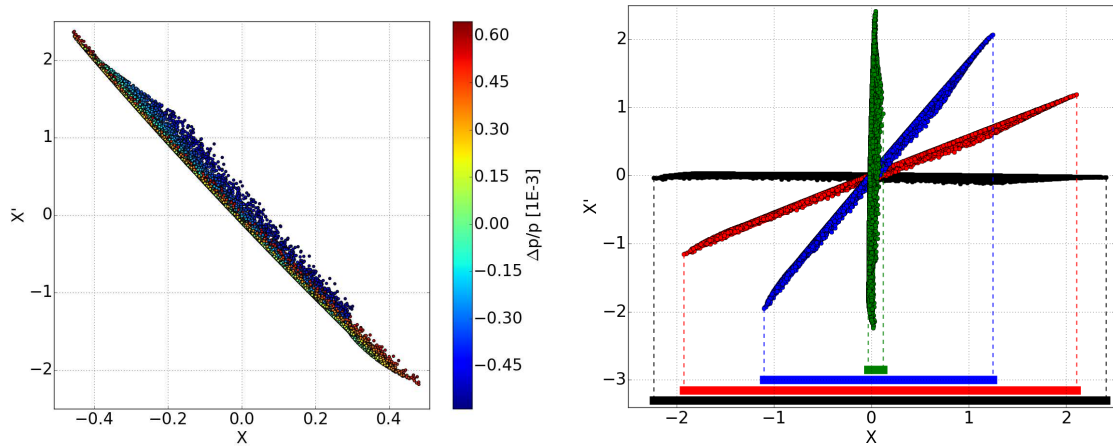
(a) Colorcoded momentum distribution within the BoC at EX01003SFX

(b) Four different spot sizes by different BoC rotation angles. The colored bar below indicates the according spot size

Figure 2.12.: Bar of charge (BoC) at the end of the Phase Shifter Stepper (PSS) in normalized phase space for different settings.

Figure 2.13 shows the design optic for various beam sizes. The six quadrupoles of the PSS are indicated above in red, two beam position monitors (SFX) in blue with EX01003SFX being the most relevant monitor for the measurements in this thesis as well as two corrector dipoles in gray.

In the horizontal plane the β-functions are identical at the entrance and the exit of the module, only the phase advances are different. Though, in principle every phase advance can be achieved which for this thesis is the main functionality of the PSS. An adaption of the β-function corresponds to an optical 'zoom' on a measurement performed downstream.

2.4. Tomography

Tomography is the process of determining the inside of an object in a 2D domain by assembling information of 1D-dimensional projections gathered from outside of the domain[47]. Mathematically this concept bases on the *Radon transformation*[48] while the reconstruction of the initial domain represents the inverse transformation. A well known implementation of tomography is the x-ray computed tomography (CT) or the positron emission tomography (PET) in medical applications. The resulting image of the initial domain is called *tomogram*.
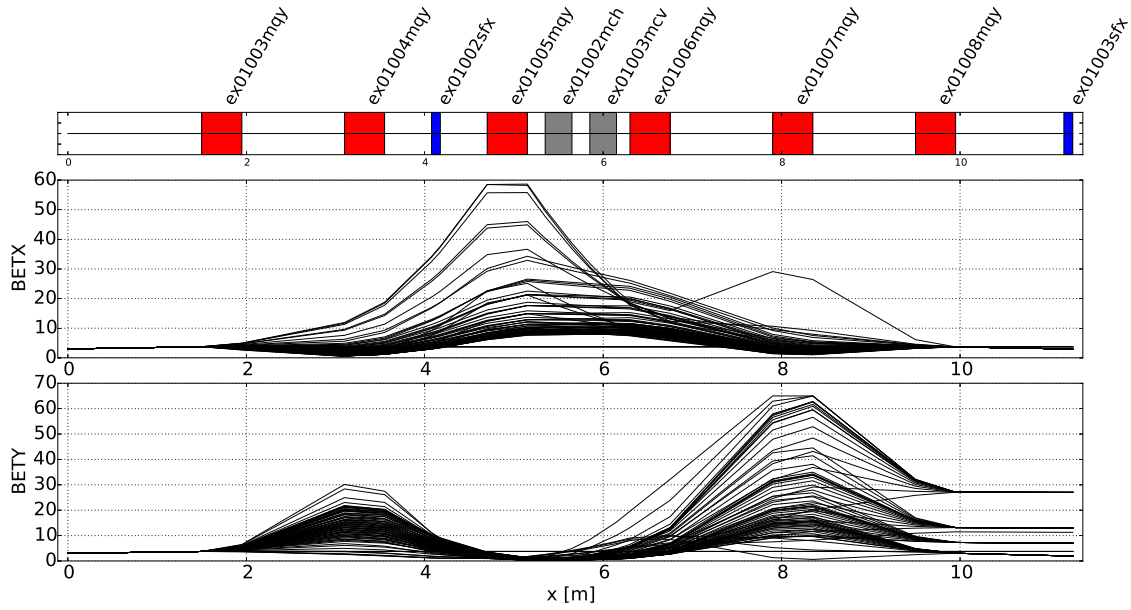
Figure 2.13.: Horizontal phase advances shift and vertical beta stepping for various beam size settings (design optics)

The following sections describe the Radon transformation, give an overview of the concept of reconstruction as well as describe the two reconstruction algorithms used in this thesis: *Filtered Back Projection* as well as the iterative approach *(Simultaneous) Algebraic Reconstruction Technique.*

2.4.1. Radon transformation - Sinogram

Assuming an object of interest as a function $f(x,y)$ in $\mathbf{R}^2$ and γ a detector line defined by the angle Θ with respect to the x-axis and the distance s to the origin outside of the object. Then one measurement representing a projection of the object onto the detector line by line integrals of parallel lines g perpendicular to the detector line is shown in Figure 2.14(a) and 2.14(b) and defined as

$$p_\Theta(s) = \int_g f(x,y)dl \tag{2.27}$$

with the parametrization of the integral line g

$$g = x\cos\Theta + y\sin\Theta \tag{2.28}$$

This projection can represent the attenuation of x-ray intensity in a CT or the counts of photons in PET. In this thesis a projection will be a beam distribution measurement via a beam position monitor.

19

(a) A single projection line g along which a line integration is performed representing a single point in the new projection domain

(b) Parallel integration lines resulting in a projection on the detector line
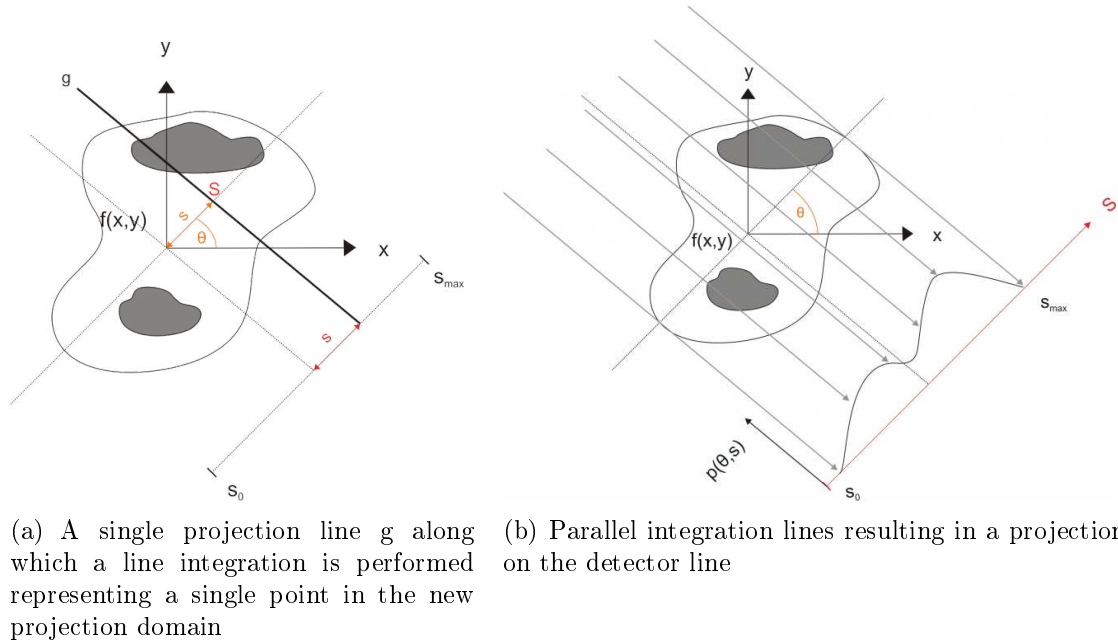
Figure 2.14.: Sketches of the principle of the radon transformation[9]

Considering all projection angles $0 \leq \Theta \leq \pi$ and distances $s_0 \leq s \leq s_{max}$ defines the *Radon transformation*

$$Rf(\Theta, s) = \int_g f(x, y) dl = p(\Theta, s) \tag{2.29}$$

with the graphical representation of the created projection domain (stack of projections all projection angles) called *sinogram*[23]. Figure 2.15 shows an example of an initial distribution as well as the according sinogram.

2.4.2. Reconstruction

In the continuous case (infinite number of angles, infinite steps in s) the object domain can be reconstructed entirely via the following concept:

- Each projection (Radon transform) can be 1D Fourier transformed representing a single line passing through the origin of the frequency domain at the projection angle $\Theta = Central\ Slice\ Theorem$

---

[23]The term sinogram originates from the fact that a point-like initial distribution represents a sinusoidal wave in the projection domain.

(a) Initial distribution in object domain

(b) According sinogram (127 angles) in projection domain
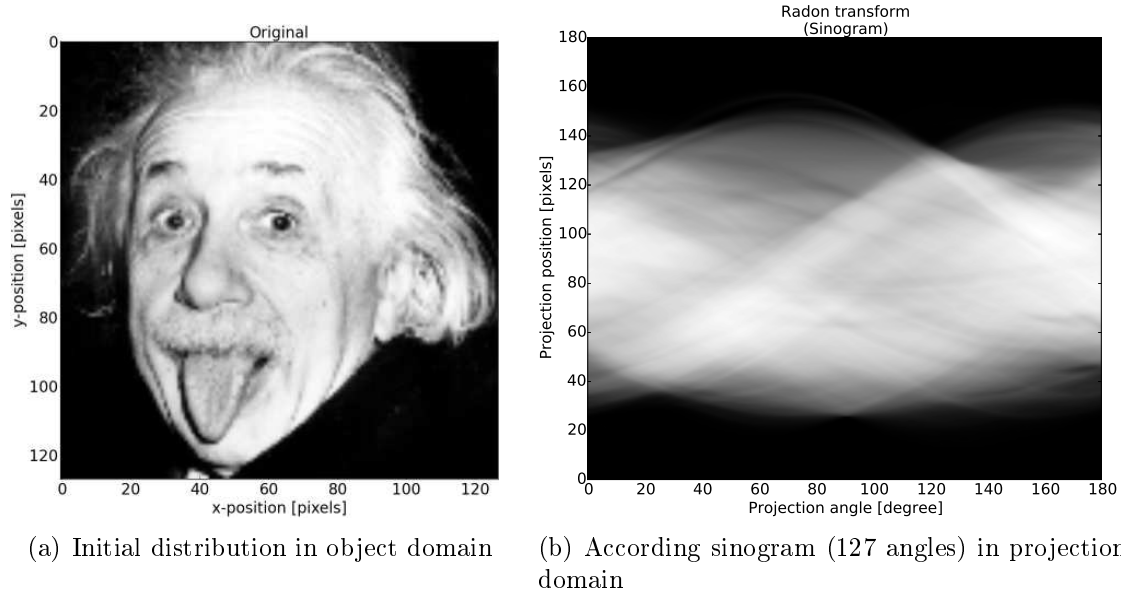
Figure 2.15.: Illustration of an initial distribution and its sinogram

- Because in the continuous case the frequency domain is complete, a 2D inverse Fourier transformation can be computed reconstructing the initial distribution in the object domain

In practice, the immanent problem of incomplete sets of data occurs: 1) the number of projection angles Θ is finite (typically a few single up to a few hundred angles) and b) detectors to acquire the projections have a minimum spacial resolution resulting in s being discrete. Therefore, Fourier space is not complete and any reconstruction requires some kind of approximation introducing artifacts (=systematic discrepancy between initial object and tomogram) in the reconstruction leading to a $f(x, y)$-similar distribution $g(x, y)$. Different algorithms including different approximations have been established with the most popular being Filtered Back Projection (FBP), different kinds of Algebraic Reconstruction Techniques (ART, SART, SIRT, ...) or Maximum Entropy Reconstruction.

2.4.3. Filtered Back Projection (FBP)

The most simple method to reconstruct the initial distribution $f(x, y)$ is called *back projection* which basically means 'smearing' out each profile along Θ over an initially empty objection domain grid. After all projections via all angles have been processed, the content of each cell of the grid is summed. As the result is strongly blurred and shows a large amount of artifacts, this method is basically not used. One can imagine the situation as followed: the limited number of lines in frequency domain (Fourier space) result in a higher data point density close to the origin

representing low frequencies while further outwards the data point density is lower. Therefore edges and boundaries are not well represented.

This major disadvantage in the FBP is counteracted by applying a high pass filter attenuating low frequency contributions and therefore emphasizing edges. This filtering is achieved by Fourier transforming each profile, applying an according filter (convolution of the data with e.g. a Ram-Lak, Hann or Shepp-Logan filter; see Figure 2.18(a)) and transforming back resulting in a changed profile then used for back projection.
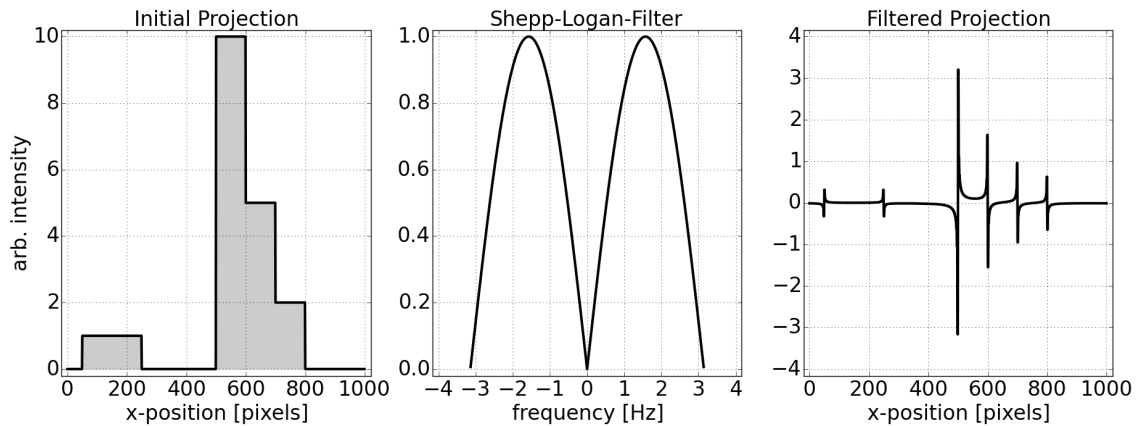
Figure 2.16.: Example for an unfiltered projection, the Shepp-Logan filter function and the filtered projection

Figure 2.16 (left chart) shows an example for an unfiltered projection used with back projection. The middle chart shows the according Shepp-Logan filter function attenuating low frequencies and a high frequency cut-off to reduce noise. The right chart illustrates the filtered profile used with FBP. Edges are strongly pronounced with respect to plateaus.

Figure 2.17 shows the reconstructed tomogram of the previous example sinogram using FBP with different numbers of projection angles. While Figure 2.17(a) shows the single filtered projection, Figure 2.17(b) shows a reconstruction based on projections of 32 angles. The initial distribution can be identified but also the artifacts are clearly visible. Figure 2.17(c) uses 127 which means one projection angle per projection pixel (127 angles, 127 pixels).

Mathematically, FBP can be summarized in the following equation:

$$g(x,y) = \int_0^\pi d\Theta \left[\int_{-\infty}^{\infty} d\omega |\omega| P(\omega) e^{2\pi i \omega s} \right]_{s = x\cos\Theta + y\sin\Theta} \tag{2.30}$$

with

(a) 1 angle   (b) 32 angles   (c) 127 angles
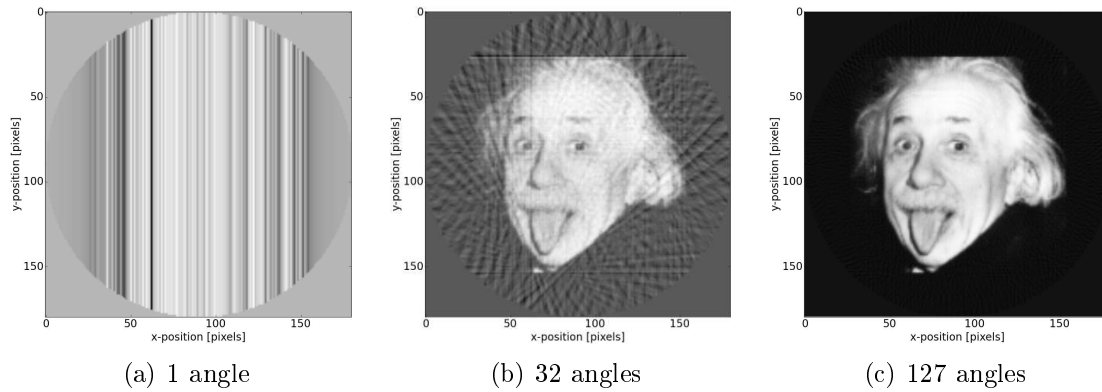
Figure 2.17.: FBP reconstruction for different numbers of projection angles Θ

- $P(\omega)$: the Fourier transform of $p(\Theta, s)$

- $|\omega|$: the ramp filter

- $\int_{-\infty}^{\infty}$: the inverse transformation

- [...]: the back projection

- $\int_0^\pi$: the sum over all filtered projections

The back projection represents the reverse process of the projection shown in Figure 2.18(b): The value of the filtered profile point $P(\Omega, s)$ contributes to the entire (x,y) domain. In a pixel-driven approach, the discrete data point of $P(\Omega, s)$ typically doesn't pass the center of the domain pixels its contributing to. Therefore, the value is interpolated via different approaches (e.g. linear, nearest, cubic or spline).

2.4.4. Algebraic Reconstruction Technique (ART)

The Algebraic Reconstruction Technique ART[24] and its derivatives like SART (Simultaneous Algebraic Reconstruction Technique) or SIRT (Simultaneous Iterative Reconstruction Technique) interpret the Radon transform as a system of linear equations basing on the fact that the initial object domain is discretized by the detector resolution anyway and therefore represents a 2D matrix. The projections can be described mathematically as

---

[24]ART described by Gordon, Bender and Herman 1970[49] was the first algebraic reconstruction technique and bases on the Kaczmarz method[50] of solving linear equation systems.

(a) Window filter functions

(b) Back projection of the filtered profile onto the pixel-based space domain
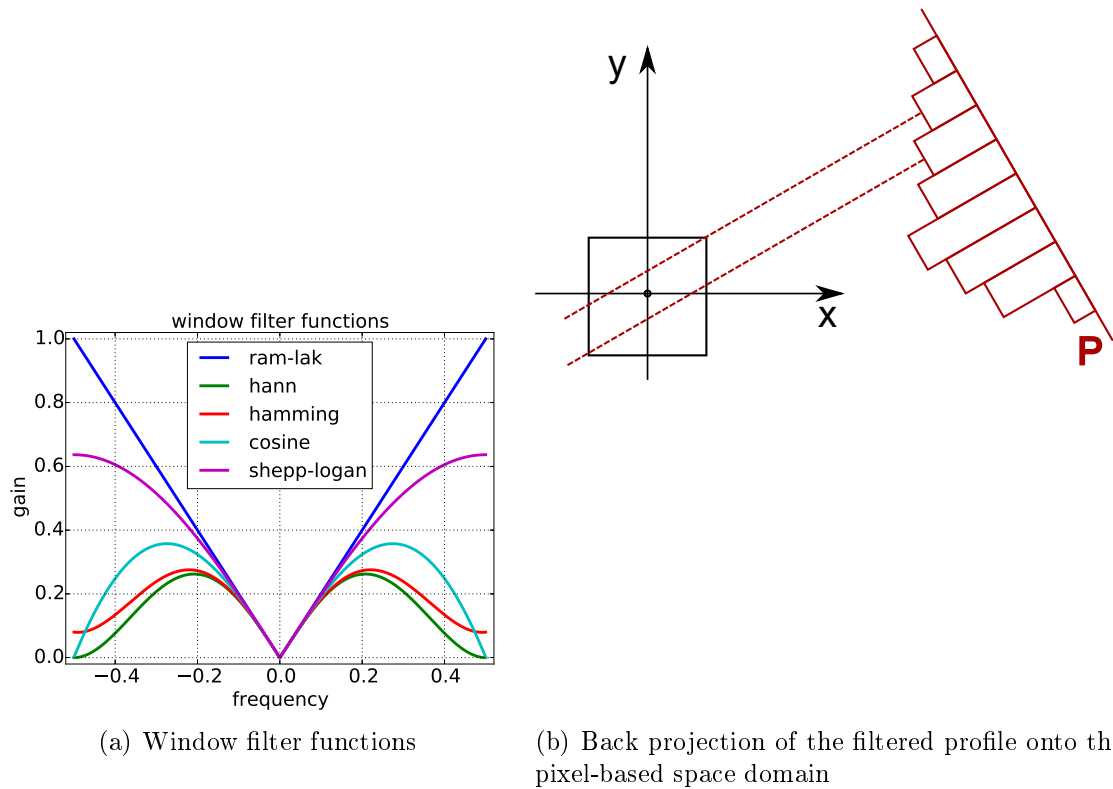
Figure 2.18.: Visualization of various filter functions and graphical interpretation of back projection illustrating the need of interpolation.

$$
\begin{aligned}
w11f1 + w12f2 + w13f3 + ... + w1nfn &= p1 \\
w21f1 + w22f2 + w23f3 + ... + w2nfn &= p2 \\
... & \\
wm1f1 + wm2f2 + wm3f3 + ... + wmnfn &= pm
\end{aligned}
\tag{2.31}
$$

with f_j as a one dimensional vector representing the pixel values of the matrix of length N^2, w_{ij} as a matrix of the weights of the cells of size M by N^2 and p_i as the projection value of length M.

The weights can be interpreted as the contribution of a single cell value to the projection and two examples are shown in Figure 2.19: the 'line kernel' as the length of the projection ray within a certain cell (points A to B) and the 'strip kernel' as the area within a cell contributing to a certain detector strip.

From this system of equations $\mathbf{p}=\mathbf{wf}=\sum_i w_{ij}f_j$ the parameters $\mathbf{p}$ and w_{ij} are known with typically $f_j=\mathbf{W}^{-1}\mathbf{p}$ not being solvable as $\mathbf{W}$ is too large to be inverted. ART algorithms therefore solves this problem iteratively with the following concept:

- start with an initial guess of $\mathbf{f}^{(0)}$ (often a zero-matrix or the result of a FBP)
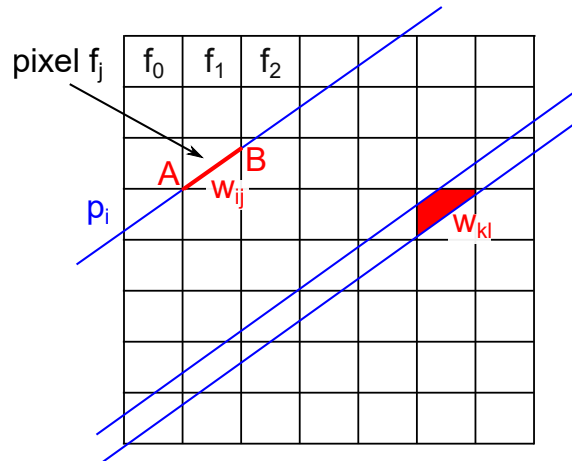
Figure 2.19.: ART matrix with different types of weights (line and strip)

- compute the forward projections as described in equations 2.31

- update $\mathbf{f}^{(1)}$ according to equation 2.32

$$\mathbf{f}^{(k+1)} = \mathbf{f}^{(k)} + \mathbf{C}\mathbf{W}^T\mathbf{R}(\mathbf{p}_m\text{-}\mathbf{W}\mathbf{f}^{(k)}) \tag{2.32}$$

with

- $\mathbf{W}\mathbf{f}^{(k)}$ as the forward projection of the current solution

- $\mathbf{p}_m$ as the measured projections

- $\mathbf{R}$ as a weight $r_{ii} = 1/\sum_{j=0}^{n-1} w_{ij}$ (short rays have a higher contribution; required for convergence)

- $\mathbf{C}\mathbf{W}^T$ as the back projection weighted by $c_{jj} = 1/\sum_{i=0}^{m-1} w_{ij}$

One iteration is complete when all equations of ray projections have been used exactly once [51]. While ART updates the values of the cells of the 2D matrix after every equation, SIRT only updates the matrix at the end of every iteration with the average of all computed cell contributions. With SART, the matrix cells are updated after all projections of one projection angle have been computed. As typically the projection information of neighboring angles are highly correlated, the order of used angles is selected randomly.

For data consisting of high resolution (detector pixels as well as projection angles) and good signal-to-noise ratio, FBP typically is the favorable algorithm as it is much faster than the resource-intensive ART algorithms[25]. However, for noisy, lower resolution data typically ART algorithms deliver much better results[52].

---

[25]Therefore also in nowadays x-ray CT scanners FBP is used as reconstruction method.

3. Simulations

This chapter contains details and results of simulations that have been performed prior beam measurements to a) proof the concept of tomographical phase space reconstruction via the Phase Shifter Stepper module, b) identify appropriate data acquisition settings, c) test the developed software to be ready for measurement data processing as well as d) create reference results for comparison. For the simulations of particle distributions and all required beam optic computations the CERN[53] particle accelerator software MAD-X[54] was used. Furthermore, a dedicated Python[55] software framework was developed to gather the input data, create a sinogram required as input for the reconstruction, handle the reconstruction and process, filter, quantify and visualize the output data. For the reconstruction itself the Python *skimage*[56] module was used.

On the next pages the terms sinogram and tomoscope are explained, parameters to quantify a sinogram or tomoscope are introduced, potential reconstruction algorithms are compared, the effect of noise and the number of projections is shown as well as errors due to imperfect trajectory steering including their correction mechanisms are presented.

3.1. Quantification parameters

In order to describe and compare different 2D scalar data like sinograms and tomoscopes (definition in section 3.3 and 3.4; hereafter referred to as *maps*), certain quantification parameters are required.

- **beam cells**: cells of a map containing beam information

- **empty cells**: maps of simulated data (distributions and sinograms) that only contain noise or artifacts. Therefore all cells but beam cells are empty.

- **artifact cells**: the reconstruction intrinsically introduces artifacts in all cells. While in beam cells the scalar value representing beam information (typically intensity) is modified, non-beam cells only contain artifact data[26].

---

[26] Real measurement data typically contain some kind of noise in all cells. A distinction between artifact and noise is not easily possible.

- **delta map**: cell-wise difference of two maps (map1 - map2)

Mean Absolute Error (MAE[57]) The average of all absolute values of the delta map in a) beam cells or b) artifact cells result in the MAE_{beam} resp. MAE_{arti}

$$\text{MAE}_{\text{cells}} = \frac{1}{\text{number of cells}} \sum^{\text{cells}} |\text{cell error value}| \qquad (3.1)$$

The alternative parameter 'root mean square error (RMSE)' implies a weighting of the errors which is not adequate for these analysis and therefore is not used in this study.

Emittance via threshold analysis (EMT) Often emittance is referred to as area in transverse phase space shaped as an ellipse covering a certain fraction of the intensity of a Gaussian distribution. However, the object of interest of this study is a non-Gaussian particle distribution (the 'bar of charge') and it has already been shown that various ellipses can be found trying to describe the same phase space density distribution varying in size[11].

Therefore, this study for this definition of emittance follows Conte and MacKay ('...emittance somehow specifies an area of a region of transverse phase space where the beam is located at some instant of time.', p335 [38]) and Wiedemann ('...one might define the beam emittance containing 95% of the total beam intensity or whatever seems appropriate.', p292 [37]) but generalizes it to also sinograms.

The definition does not base on any shape of the distribution nor determines if the area has to be locally connected. The value of EMT defines the number of cells of a map containing a certain percentage of the entire map intensity. It is evaluated by 1) computing the cumulative sum of the intensity-sorted cells and 2) counting the number of cells above a certain threshold of the maximum. The acronym EMT20 describes the number of cells computed as described above with a threshold of 20%.

Emittance via SCUBEEx analysis (EMS) The Self-Consistent Unbiased Elliptical EXclusion analysis method[58] assumes a localized beam distribution and surrounding background in transverse phase space. The computation of the emittance follows an iterative process increasing the boundaries of a virtual area (ellipse) each iteration computing the average intensity (offset) outside the area, subtracting this offset from the inside data and evaluating the rms emittance[27] inside the area. When the size of the area has been increased to contain the entire beam distribution, the two curves (rms emittance and offset vs. area size) stabilize on a plateau. The resulting area describes the unbiased estimate for the rms emittance from which the Twiss functions can be computed. For more details, the interested reader is referred

---

[27]$\epsilon_{rms} = \sqrt{\langle x_i^2 \rangle \langle x_j'^2 \rangle - \langle x_i * x_j' \rangle^2}$

to the literature[59][60][61][62] including the description of the implementation used in this thesis[63].

Number of cells above threshold (CAT) The CAT describes the number of cells with a value above a certain threshold. The CAT10 represents the number of cells with a (intensity, amplitude) value above 10% of the maximum value of the entire map.[28]

3.2. Beam optics

For all following simulations and measurements the optics of the PSS described in chapter 2.3 has been adapted in order to enlarge the particle distribution on EX01003SFX which is the used beam profile monitor (BPM) in this study. As shown in Figure 3.1 the horizontal beta functions (BETX) have been matched to be 40m at the BPM for all used phase advances which corresponds to a maximum length of the bar of charge of $x_{ESE} * \sqrt{\beta/\beta_{ESE}} = 10\text{mm} * \sqrt{40/5} \approx 28\text{mm}$ instead of $\approx 8\text{mm}$ at design optics. The horizontal alpha functions (ALFX) indeed are varying for various phase advances but a) the normalization of the beam profiles requires BETX only and b) for measurements the beam will indeed be lost which is expected and acceptable. Constraints on the matching of the vertical beta and alpha functions at the BPM are not applied.
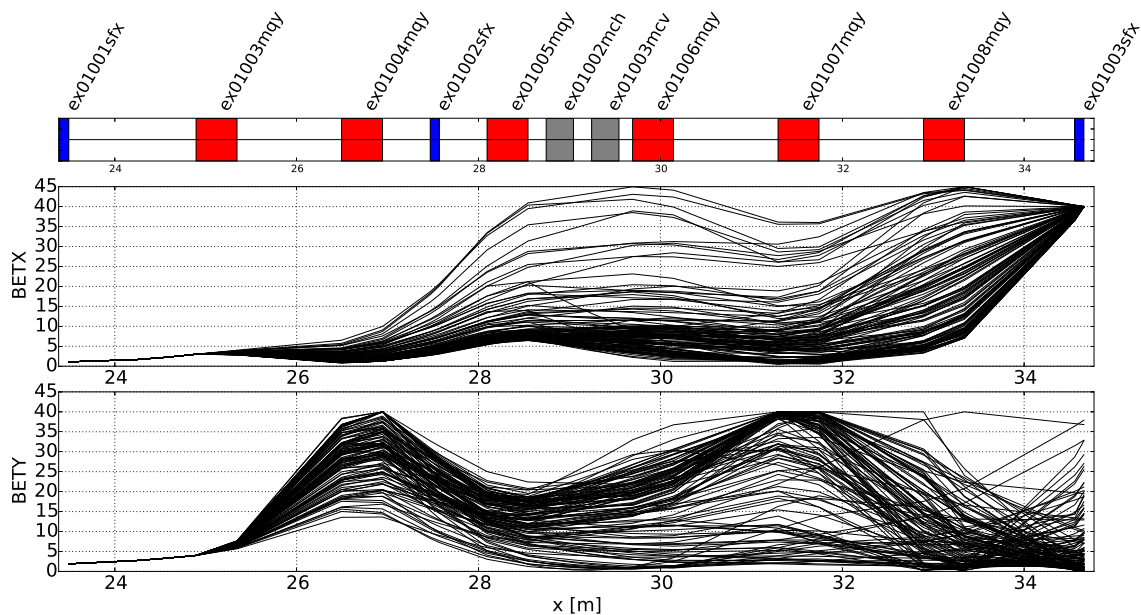

Figure 3.1.: Zoomed PSS optics

---

[28] Also the EMT represents a number of cells above a threshold but with the threshold being based on intensity rather than absolute values.

The aperture in this section of the transfer line is ±33mm therefore a further increase of BETX could be performed resulting in gathered beam profiles of higher resolution. However, it has to be avoided that particles are lost inside the PSS in both planes. The bar of charge naturally has 'sharp' edges where as in vertical plane the Gaussian distribution beam tails are more critical. Given an empirical vertical emittance[64] and considering a beam cut at ±3σ the vertical beta function is limited to 40m.[29]

3.3. Sinogram

Projections of the density of a 2D object from various angles (sinogram) are the input required to compute a tomography independent of the used reconstruction algorithm. The simulations in this study base on three different methods that are used to generate the projection data which are also compared to each other later on. Input for this part of the thesis is the *bar of charge* distribution shown in Figure 2.12. Figure 3.2 shows the distribution in real and normalized phase space sampled in 2D with the 1mm resolution of the monitor EX01003SFX[30] .
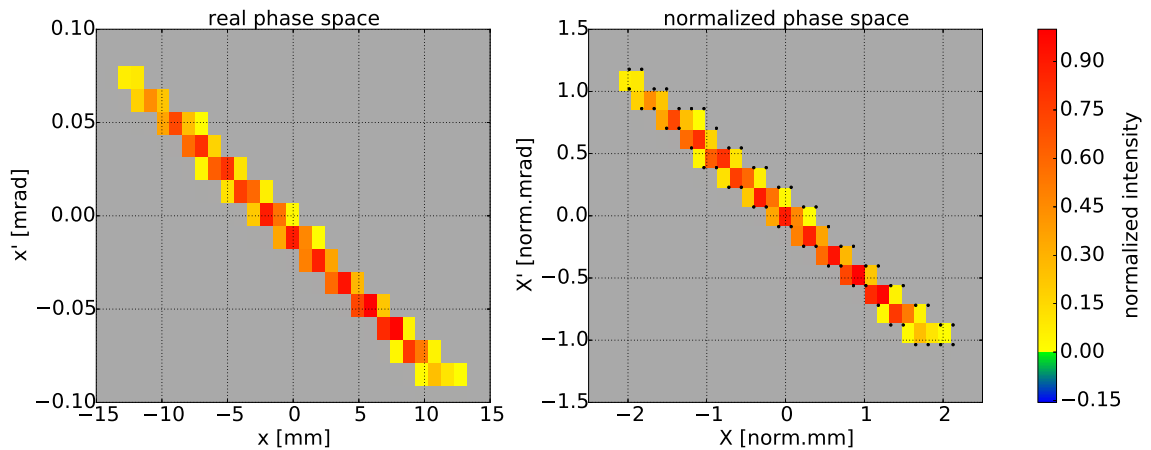

Figure 3.2.: Sampled initial distribution in real and normalized phase space

Remark: the units of both axes in normalized phase space is $[m^{1/2}]$. However, for clarity and to avoid mixing up with real phase space diagrams, in this thesis X'-axis typically is indicated with the unit *norm. mrad* and the X-axis with *norm. mm*. The abbreviation *norm* indicates the normalized phase space while mrad identifies X' (10^{-3}) and mm X (10^{-3}).

---

[29]More figures on the beam optics are available in the appendix A.2, A.3.

[30]The used scintillating fiber monitors (SFX) consist of 64 scintillator fibers of 0.9mm width each separated by a 0.1mm aluminum spacer. Optical fibers guide the light generated by particles interacting with the scintillator to a CCD camera which counts the interactions.

3.3.1. Rotorgram

As described in 2.1.1, in normalized phase space particles of same emittance describe a circle rather than an ellipse like in real phase space. Therefore it is possible to mathematically rotate those particles by a) transforming their Cartesian to cylindrical coordinates, b) changing the angle which corresponds to a required phase advance keeping the radius constant and c) transforming the coordinates back to the Cartesian system (see 3.3, right figure).

By performing this procedure for an entire particle distribution[31] for various phase advances, one for each iteration can compute a histogram of the X-coordinates of the particles representing the binned projections of the distribution onto the X-axis. This mathematical sinogram in this thesis is referred to as *rotorgram*.

3.3.2. PSS rotated particles

For this study the single particle tracking module PTC MAD-X is used. This software amongst others provides the option to place virtual particles in an accelerator lattice, simulate their behavior passing through the accelerator and store their position parameters (transverse and longitudinal) at dedicated observation points. This process is called *(particle) tracking*.

Therefore, this software is used to track the known particle distribution through the PSS section for different quadrupole strengths configurations representing different phase advances μ_x (see section 3.2). The resulting data contains particle coordinates at the end of the PSS in real phase space. In order to be able to compare the results to the results of 3.3.1, the coordinates have to be normalized (see Floquet transformation, equations 2.5 and 2.6). Then the same procedure of binning of the normalized results of the tracking for the various phase advances can be used to determine a sinogram.

---

[31]The initial reference coordinates are achieved by tracking(see section 3.3.2).
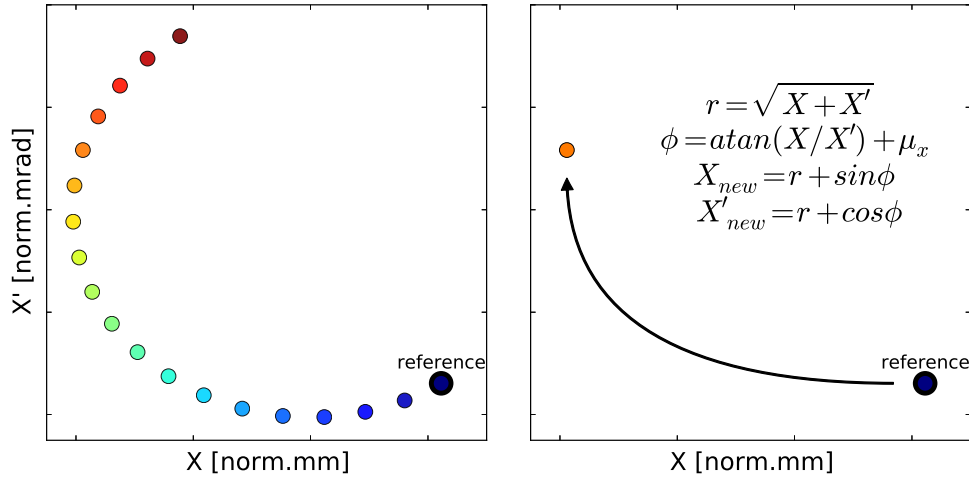
Figure 3.3.: Visualization of PSS rotated particles (left) and rotorgram (right) principle in normalized phase space

The left chart of Figure 3.3 shows the principle of PSS rotated particles. The color-coded points represent the tracking results of the same initial particle for different phase advances. The used phase advance range of the PSS is $0.25 - 0.75$ $[2\pi]$ (blue to red)[32].

Figures 3.4 and 3.5 show rotorgrams and sinograms for the same particle distribution for three different phase advances. Furthermore histograms below represent the projections of the distribution density onto the X-axis. Visually the two methods produce identical results while numerically the average difference between the two methods for the same particle is reasonably small ($< 10^{-8}$m).
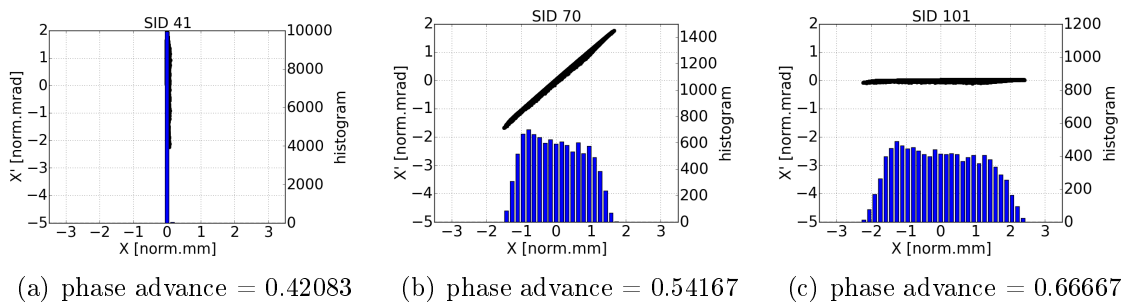

(a) phase advance = 0.42083   (b) phase advance = 0.54167   (c) phase advance = 0.66667

Figure 3.4.: Distributions for three phase advances achieved via PSS rotating the particles (tracking)

---

[32]The mechanical length of the PSS is ~11m and the beta functions are non-zero. Therefore, there is always a minimum phase advance. The maximum is limited by the quadrupole strength respectively the maximum acceptable beta functions.
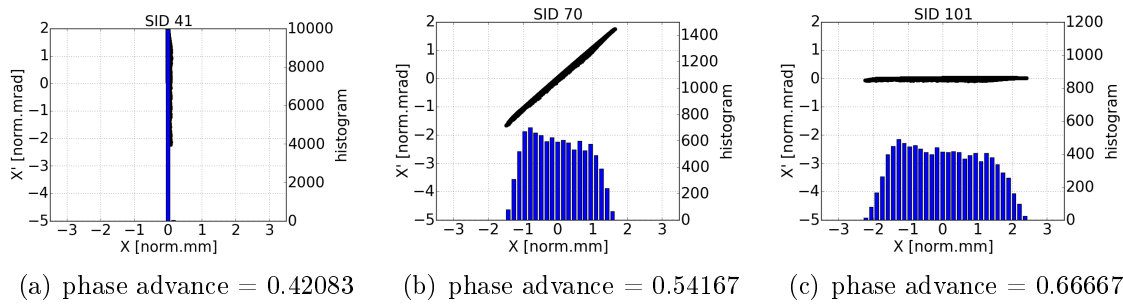
(a) phase advance = 0.42083   (b) phase advance = 0.54167   (c) phase advance = 0.66667

Figure 3.5.: Distributions for three phase advances achieved via normalized phase space coordinate rotation (rotorgram)

This finding validates a) that the MADX models match the mathematical concept, b) that the normalization mechanism works as expected and c) the resource consuming tracking for a large number of particles can be replaced by fast rotorgram computations in certain situations.

3.3.3. PSS rotated profiles

The result of a beam profile measurement typically is a binned intensity signal with a resolution limited by the used measurement device. This signal is equivalent to a binned X-axis projection of the real phase space (X' information is lost).

The third method to receive density projections of the particle distribution is using the same tracking results as in 3.3.2, performs the binning of the x-coordinates in real space and then transform the resulting profile into normalized phase space (in contrary to 3.3.2 where first the x-coordinates are normalized and then a profile is generated).

As the data during the normalization process don't change, the normalization process basically represents a linear transformation of the axis.

Figure 3.6 shows a comparison of the sinograms (normalized X-position vs. phase advance) of the three mechanisms described above. The rotorgram (left chart) is used as reference and its contour (black dots enveloping the non-grey shape) is projected to the other charts. The central chart is the sinogram resulting from the projections received by PSS rotated particles. Already the conclusions acquired from figures 3.5 and 3.4 indicated that also the sinograms should be identical.

The right chart of Figure 3.6 shows the result of the third method representing beam profile measurements (real phase space) that are transformed to normalized

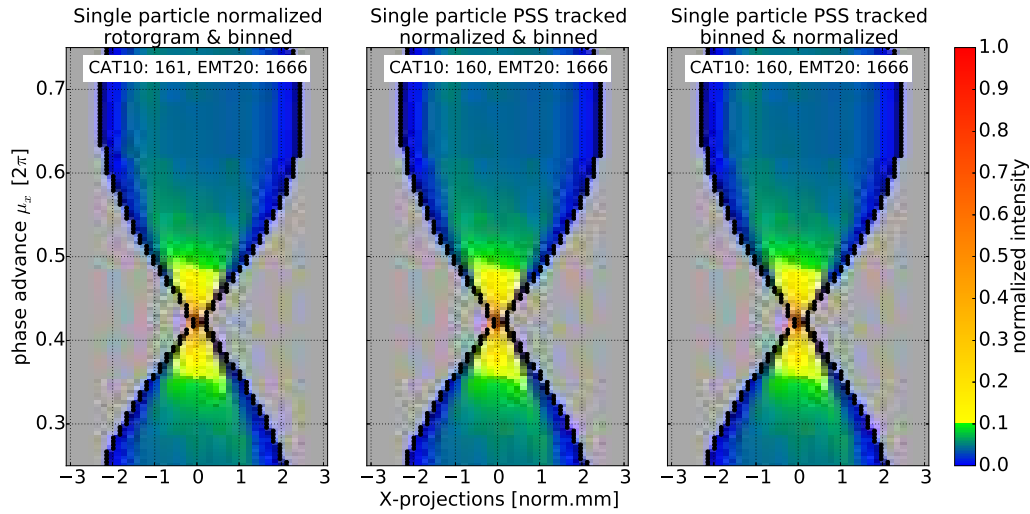phase space (PSS rotated profiles). All three sinograms visually and analytically are identical[33].

Figure 3.6.: Comparison of the results of the three mechanisms (rotorgram, PSS rotated particles, PSS rotated profiles).

3.4. Reconstruction comparison

Different reconstruction algorithm and data acquisition settings result in tomoscopes of varying quality. In the following, those settings are studied to identify a setup to be used for real measurements. In order to be able to quantify the quality of the reconstruction, typically the contour of the reference is indicated in the maps (black dots) and the parameters EMT, CAT and EMS are given as ratio w.r.t. the reference which is represented by the 2D sampled, not reconstructed particle distribution. Figure 3.7 shows 3D figures of this reference in side and frontal view.

The used reconstruction module provides the option to perform the reconstruction via the two techniques described in chapter 2.4.2: Filtered Back Projection (FBP) and Simultaneous Algebraic Reconstruction Technique (SART). While the SART algorithm doesn't provide adjustable parameters to affect the reconstruction, for FBP the window filter (see Figure 2.18(a)) and the interpolation method ('linear', 'nearest', 'cubic') can be selected.

---

[33]Differences in the CAT between the three sinograms most likely originate from a numerical limitation caused by the limited number of tracked particles (10000).

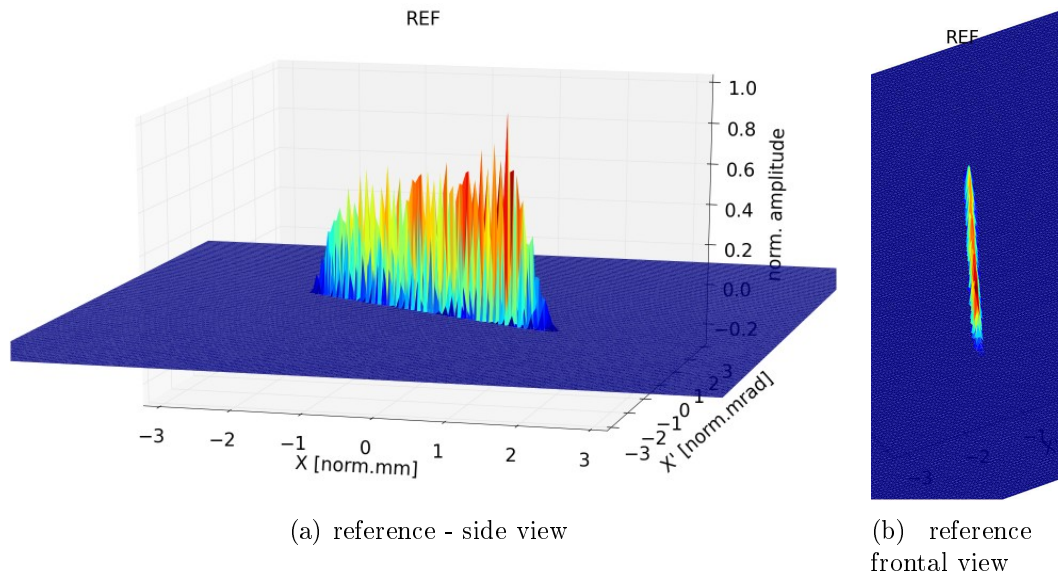(a) reference - side view

(b) reference - frontal view

Figure 3.7.: 3D illustration of the 2D sampled reference distribution

Figure 3.8 shows a result of EMT, EMS and CAT for the various combinations of the parameters. While EMS and CAT consistently overestimate the reconstruction, EMT for the combination of a ramp (Ram-Lak) filter and a cubic interpolation seem to well match the reference. Therefore these options are used as default.[34]
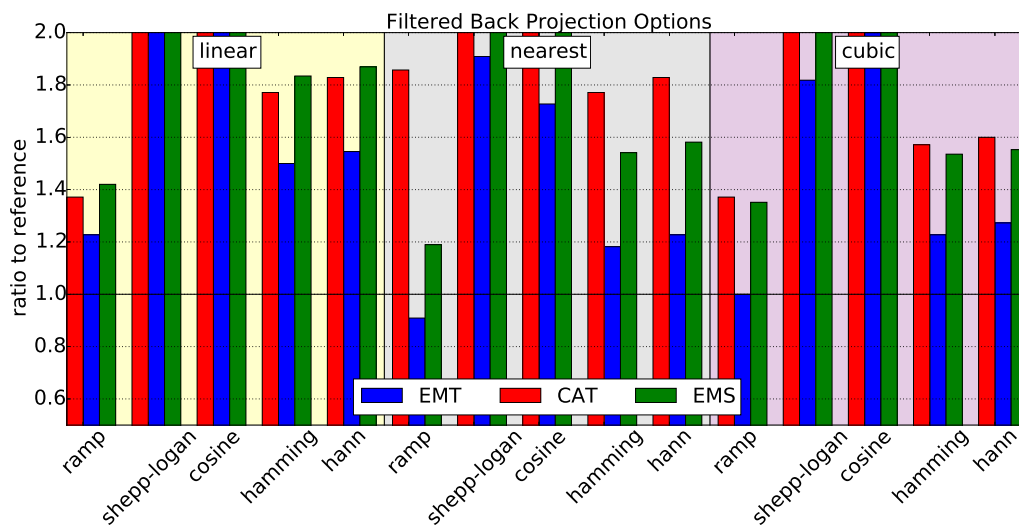

Figure 3.8.: Reconstruction quality of FBP for various options (filter, interpolation)

Figure 3.9 shows the 3D result[35] of the FBP reconstruction. While to the sides

---

[34]The result plot of the SCUBEEx analysis is shown in the appendix A.5.

[35]The following 3D charts only have a qualitative character and therefore are computed with a

(short axis) the edges are well shaped and sharp, along the long axis pronounced artifacts are created. The artifact amplitude reaches up to 20% of the maximum amplitude and therefore might affect the analysis parameters (EMT, CAT, EMS).
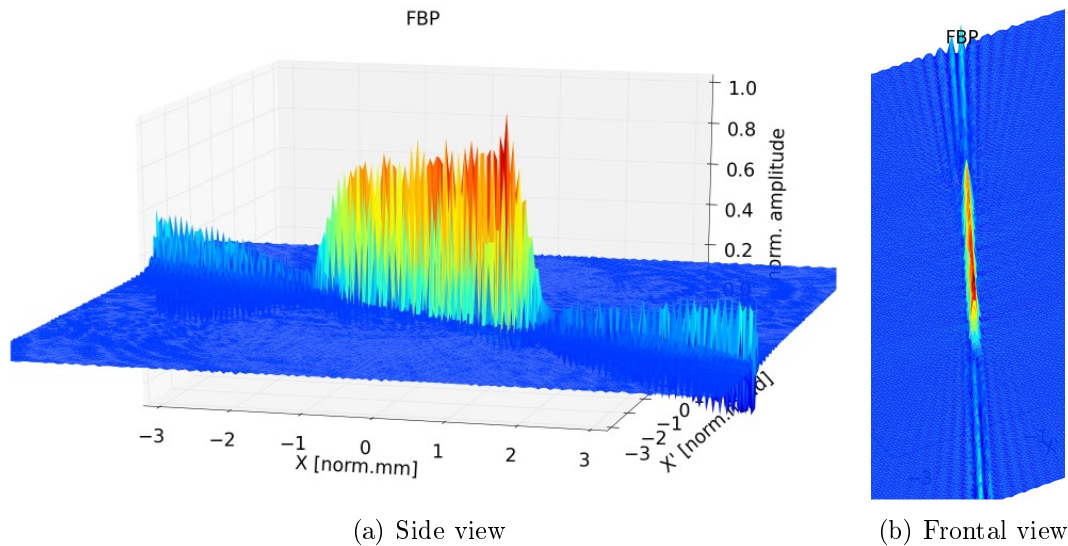

(a) Side view

(b) Frontal view

Figure 3.9.: 3D reconstruction via FBP

On the other side, the SART reconstruction (Figure 3.10) results in far lower artifact amplitudes than FBP, especially along the long axis. However, in the top view one can identify more smeared out and less sharp edges along the flanks (short axis).

---

resolution of 3 x the SFX resolution = 1/3 mm.

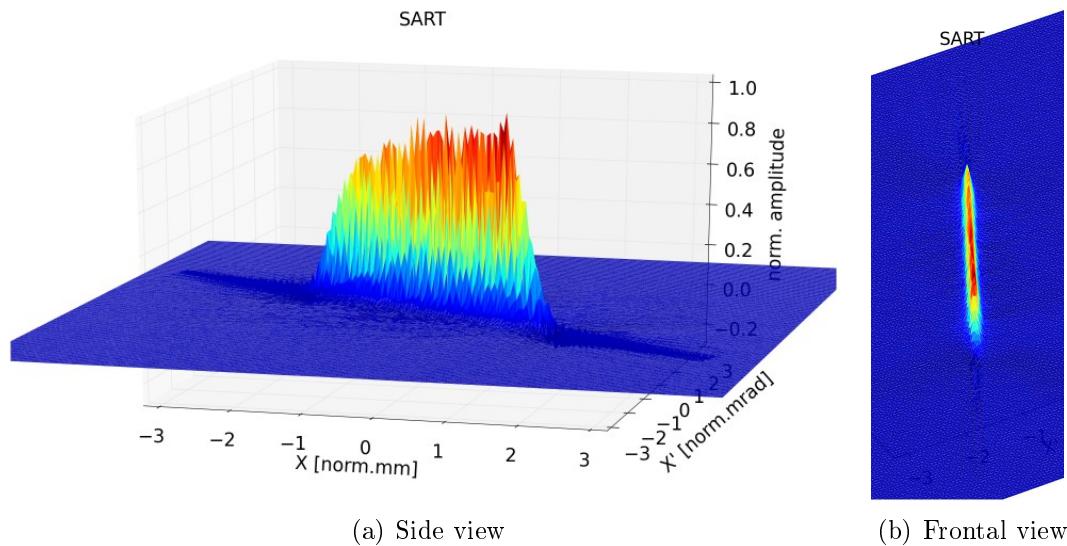(a) Side view   (b) Frontal view

Figure 3.10.: 3D reconstruction via SART

As the deficiencies of the two reconstruction techniques seem kind of complementary[36] a third 'virtual' reconstruction is created cell-wise multiplying the reconstruction maps of SART and FBP. The different artifact patterns via the multiplication operation minimize and result in a reconstruction very similar to the reference with sharp flanks and minimized artifacts along the long axis (see Figure 3.11). In the following, the acronym for this 'virtual' reconstruction is 'MULT'.
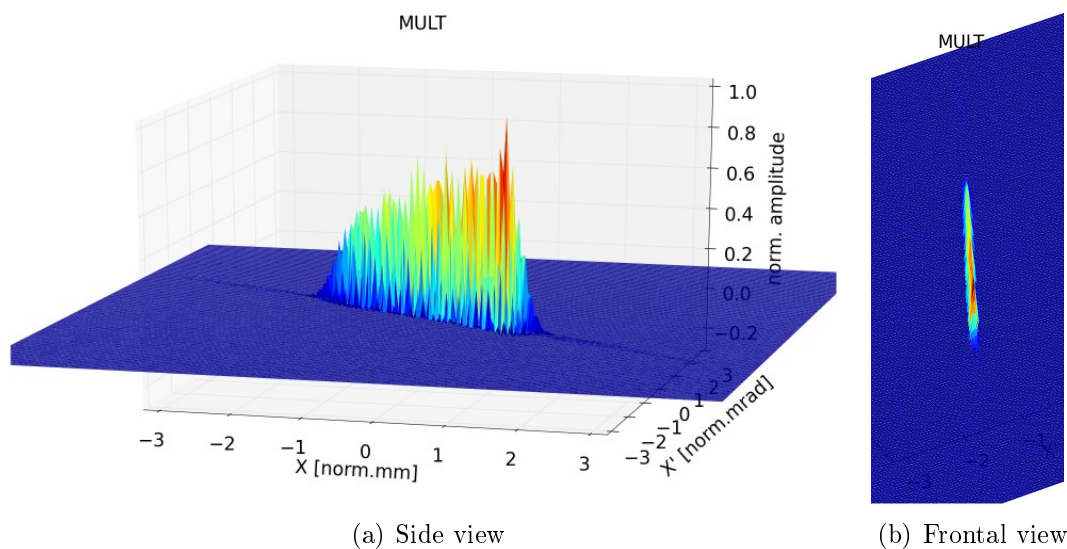

(a) Side view   (b) Frontal view

Figure 3.11.: 3D reconstruction via MULT

---

[36]Pronounced FBP artifacts are located in a region where the SART reconstruction is very close to zero while the at the SART artifact locations the FBP data is close to zero.

The result of the quantitative evaluation of the reconstructions are shown in Figure 3.12. The mean absolute error of beam cells (MAE_{beam}, indicated in blue) for SART and MULT are higher ($\approx 15\%$) than for FBP ($\approx 13\%$). As indicated already in the qualitative 3D charts, the mean absolute error of non-beam cells (MAE_{arti}, indicated in red) for FBP is the highest followed by SART and the smallest for MULT.
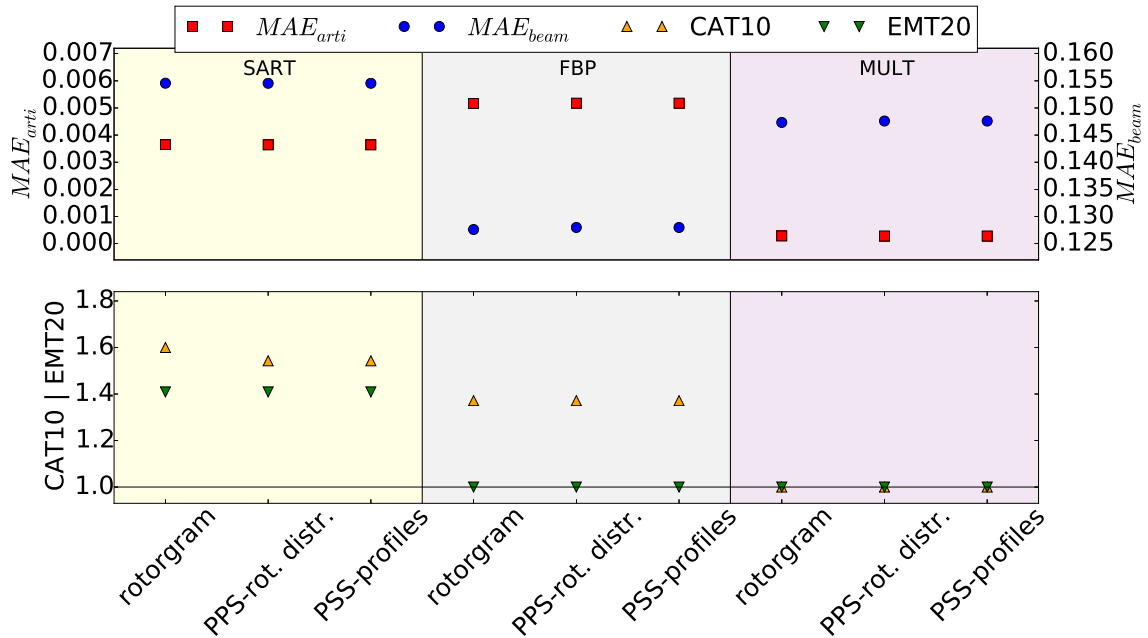

Figure 3.12.: Quantitative comparison of the three reconstruction algorithms (EMT, CAT, MAE_{beam}, MAE_{arti})

While the CAT evaluation for SART and FBP result in an overestimate w.r.t. the reference ($+60\%$ and $+40\%$), for MULT it is basically a match. The EMT evaluation for FBP and MULT fits very well and only SART again results in an overestimate of $+40\%$.

In the following, the results of the different reconstructions are discussed in more detail. Figure 3.13 shows the initial distribution as well as the tomograms via the three reconstruction mechanisms[37]. The black dots in all charts indicate the edge of the distribution in the reference map and are mirrored into the other charts[38]. This figure visualizes the interpretations so far and supports the MULT concept as for this particular distribution the tomogram matches best.

---

[37] Cells with an amplitude value of less than 5% of the maximum are colored in gray to guide the eye.

[38] Some points already for the initial distribution are not perfectly following the shown contour. This is a result of amplitudes <5% not being shown in those charts.
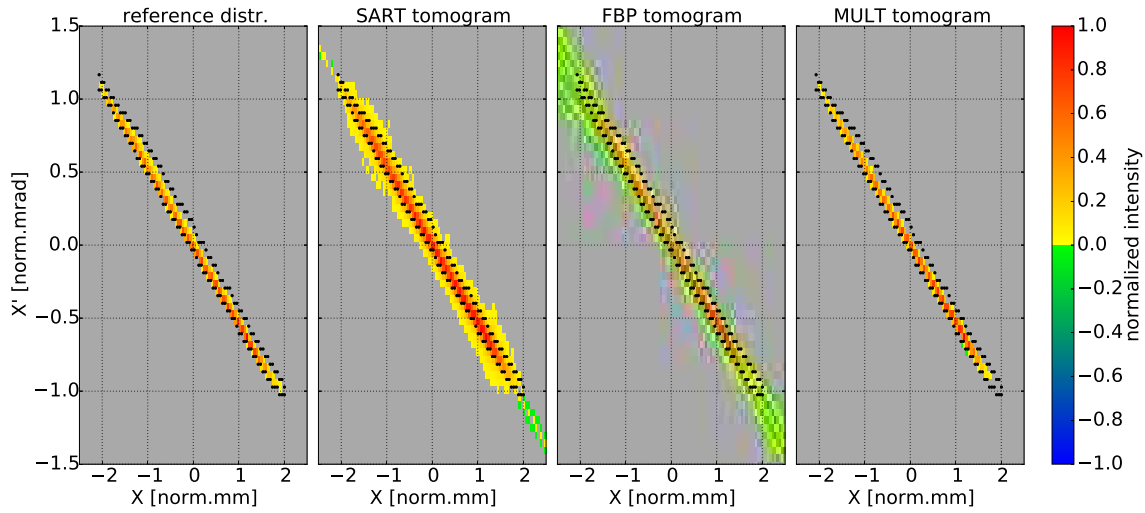
Figure 3.13.: Reconstruction comparison (3 x higher resolution)

Figure 3.14 presents the statistical evaluation of the FBP reconstruction. The left chart shows the amplitude distribution of beam cells of the reference and FBP data. While the high amplitudes (>0.5) are slightly overestimated, the lower amplitudes are underestimated. EMT20 fits very well while CAT10 and EMS result in a too high value.
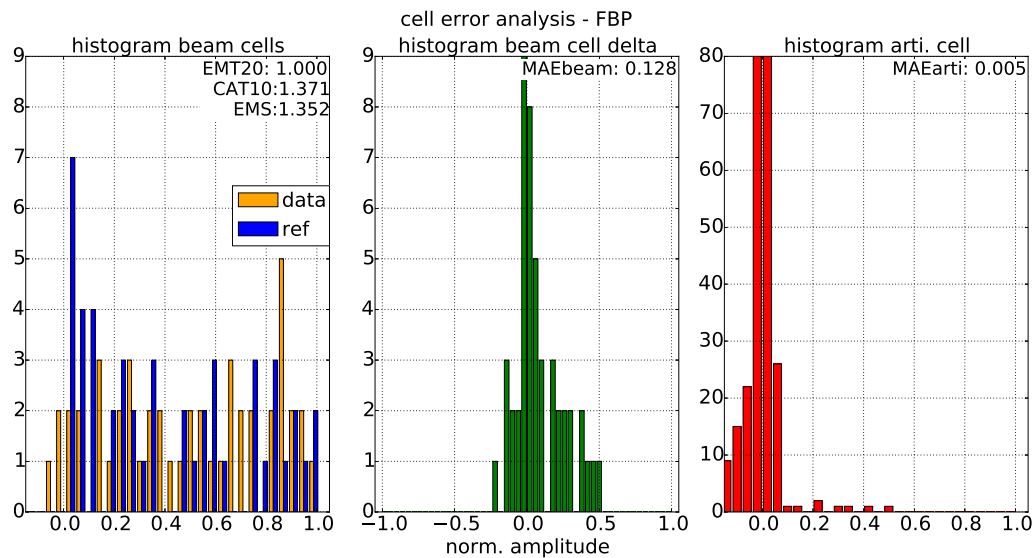

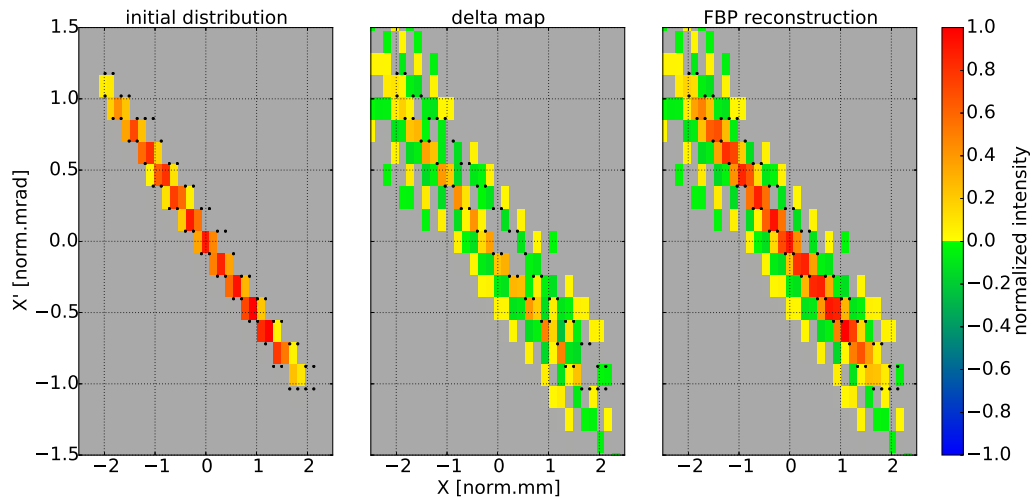Figure 3.14.: Statistical details of the FBP reconstruction

Figure 3.15.: 2D maps of the FBP reconstruction

Figure 3.15 shows three maps: the initial reference (left), the FBP reconstruction (right) and the delta map (center; reconstruction - reference). The delta map shows an overestimate along the 'lower' side of the distribution (brown/orange) as well as the pronounced artifacts (green/yellow).

Figures 3.16 and 3.17 show the same analysis for the SART reconstruction. Here an overestimate of high and middle amplitudes is visible, especially along the 'lower' side of the distribution.
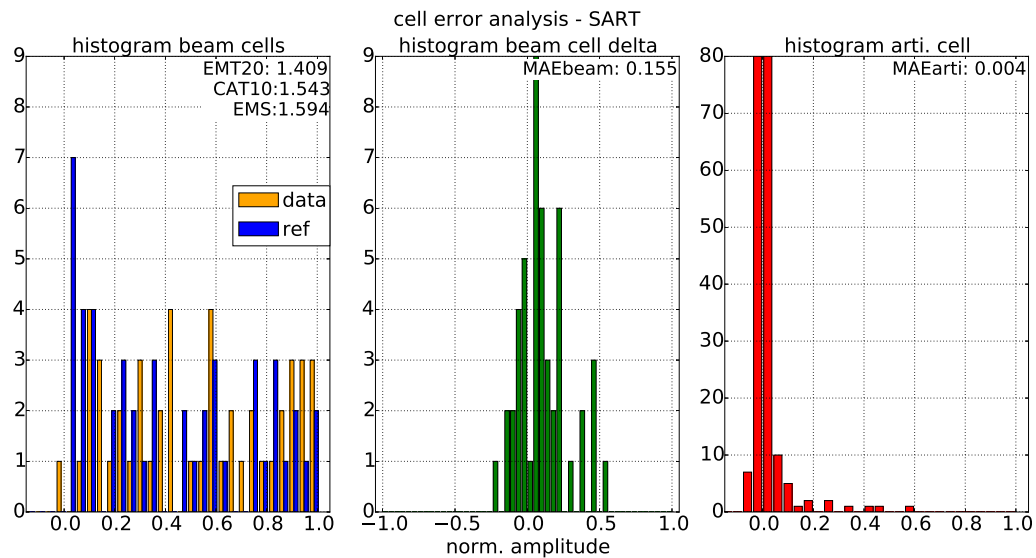

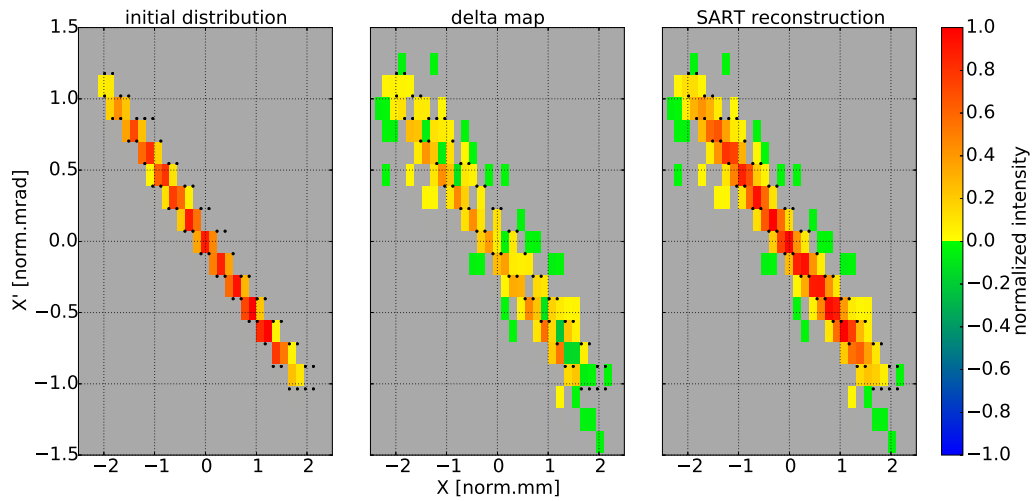Figure 3.16.: Statistical details of the SART reconstruction

Figure 3.17.: 2D maps of the SART reconstruction

The results of the MULT analysis (figures 3.18 and 3.19) shows a well matching histogram with some mismatch in the medium ranged amplitudes.
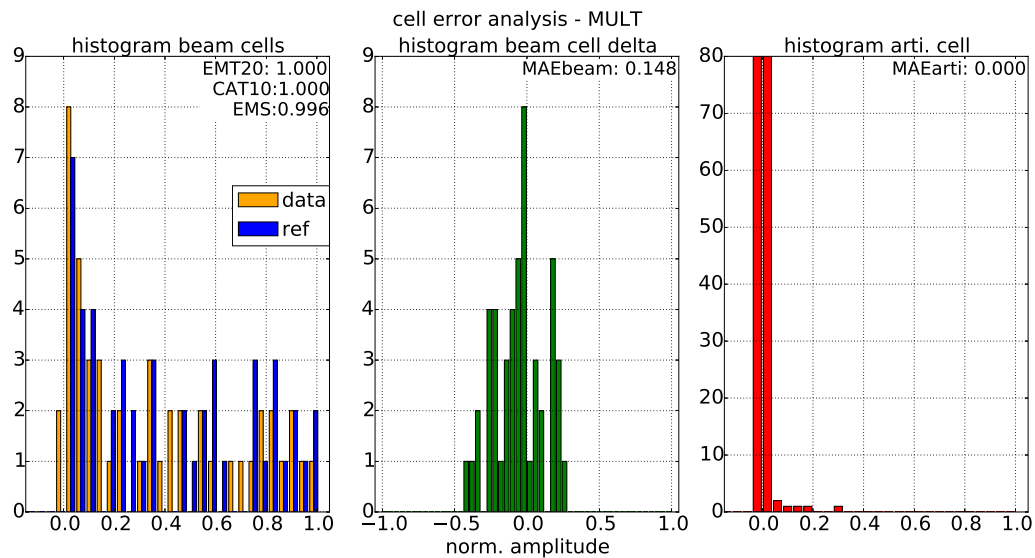

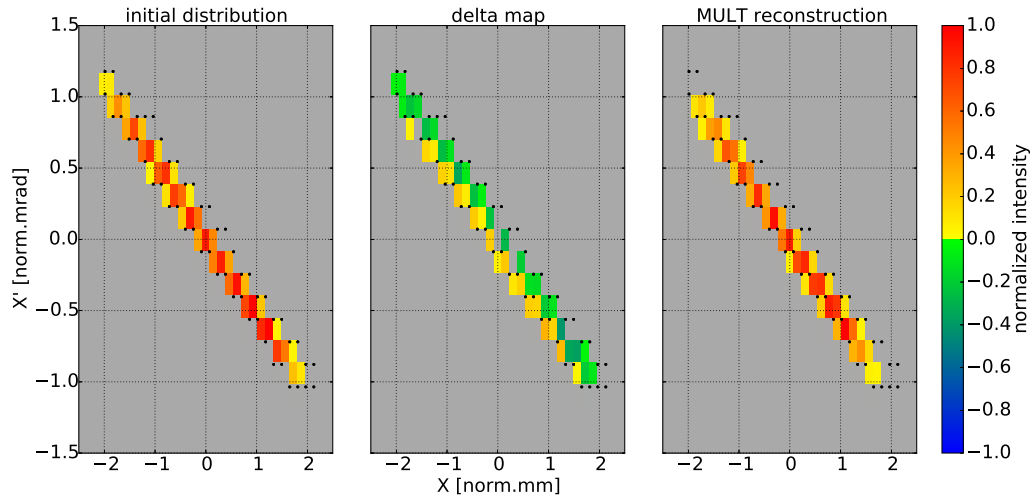Figure 3.18.: Statistical details of the MULT reconstruction

Figure 3.19.: 2D maps of the MULT reconstruction

The conclusion of this comparison of reconstruction algorithms is that

- MULT[39] provides the closest CAT, EMT and EMS ratio w.r.t the reference

- FBP for the given resolution results in the lowest reconstruction error inside the distribution (MAE_{beam}) and a well matching EMT value[40]

- SART provides a smeared-out overestimated result with the largest errors

Therefore, in the following, CAT and EMS are evaluated based on the MULT reconstruction while the EMT and MAE_{beam} bases on the FBP result.

3.5. Reconstruction stability

Various data acquisition and reconstruction parameters like the number of projections or the EMT and CAT thresholds affect the quality of the reconstruction. In the following, some of those parameters are studied and their robustness with respect to the presence of noise in the sinogram data is investigated. Finally, the effect of a non-centered particle distribution as present for real measurement data and the according correction mechanisms are shown.

---

[39]cell-wise multiplication of SART and FBP result

[40]For the reconstructions provided by the **3 x higher resolution** (Figure 3.13) the (MAE_{beam}) of the FBP is 0.118, for MULT 0.099 and SART 0.249.

3.5.1. Number of projections

The number of projections affects the details of the contour of the reconstruction: a larger number results in a more precise contour; a lower number results in a more blurred tomogram. However, typically increasing this number is not limited technically but rather organizational as an increase of measurements correlates to a larger accelerator machine time required.

Figure 3.20 shows the results of a simulation study varying the number of projections equally distributed between 0 and 180 degrees. Less than 40 angles result in CAT, EMT and EMS values factor 2 larger than the reference. The curves of all three evaluation parameters are very close to the reference (single percent) in a range of 110 to 140 angles. In this range also MAE_{beam} and MAE_{arti} are very stable (see Figure 3.21).
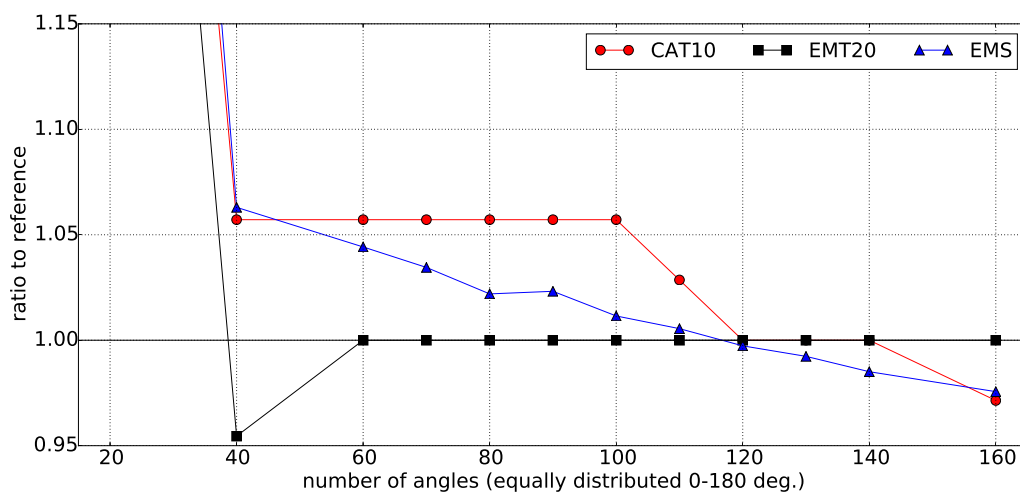

Figure 3.20.: Comparison of different number of projections w.r.t. EMT, CAT and EMS
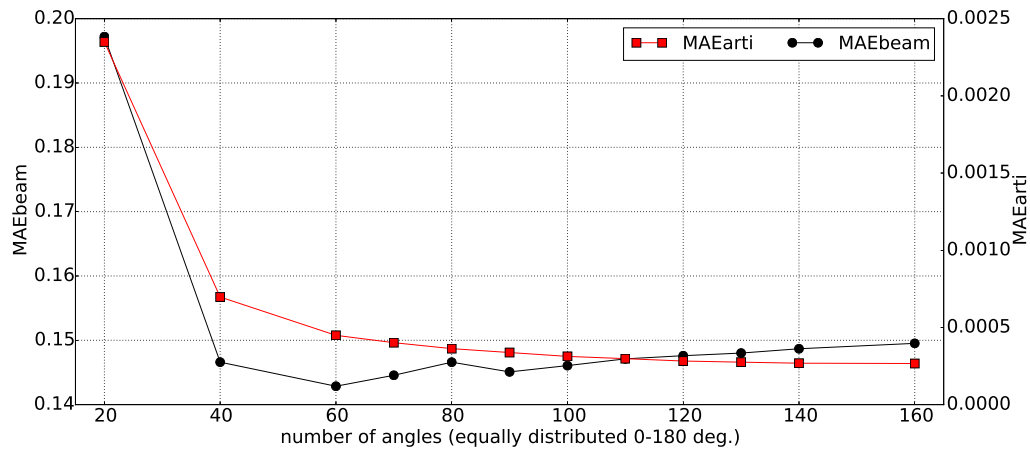
Figure 3.21.: Comparison of different number of projections w.r.t. MAE

Based on the results of these simulations 120 projection angles equally distributed between 0 and 180 degrees are used.

3.5.2. Thresholds

The thresholds used for the computation of CAT and EMT affect the resulting values as more or less artifacts are considered. However, as the bar of charge populates a small area in phase space only (given the used SFX-equivalent resolution of 1mm in real space), a high threshold results in the contribution of single cells to the CAT/EMT only. The parameter then becomes unstable easily.
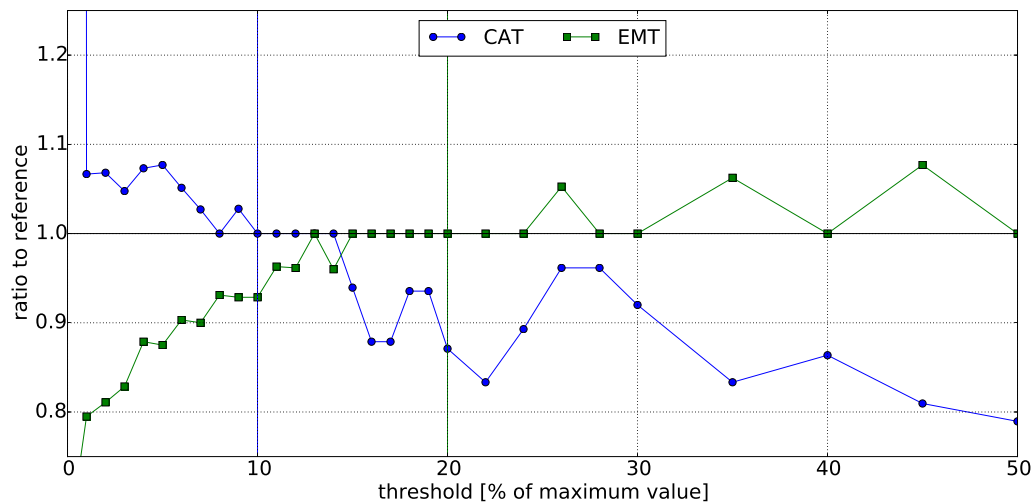

Figure 3.22.: Comparison of different thresholds of CAT and EMT

Figure 3.22 shows that the CAT presents a stable plateau at the correct reference

value in a threshold range of 8% to 14% and the EMT between 15% and 24% respectively. Therefore, CAT10 and EMT20 are used further-on.

(a) CAT10 evaluation (based on MULT)
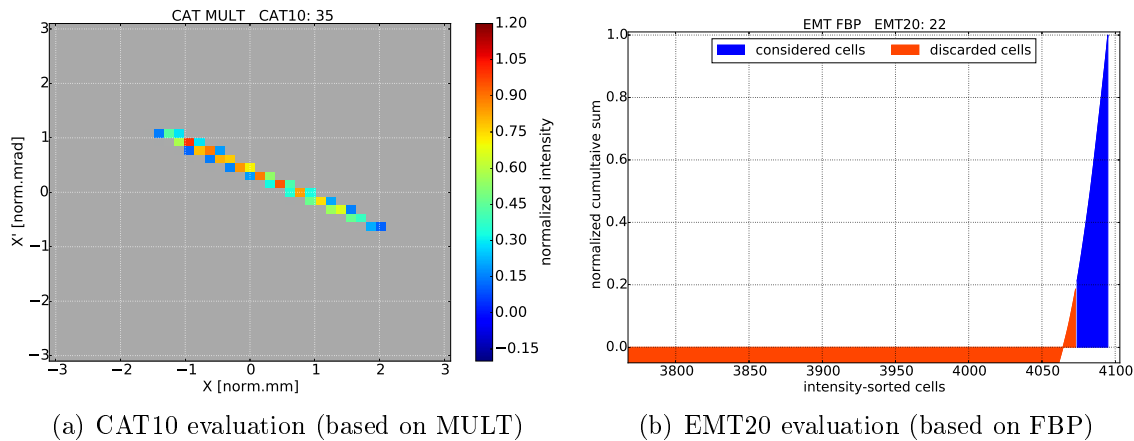
(b) EMT20 evaluation (based on FBP)

Figure 3.23.: Reference threshold charts

Figure 3.23(a) shows the resulting MULT reconstruction with all cells less or equal to 10% of the maximum indicated in gray. 35 cells (=CAT10) present a normalized amplitude larger than this threshold. Figure 3.23(b) shows the normalized cumulative sum versus the intensity-sorted cells zoomed to the beam containing cells. Due to the sorting of the cells, the cumulative sum becomes negative first, reaches a minimum and then raises again. The negative cell values all originate from artifacts while some of the small positive values might also be cells with very small beam contributions. The EMT20 for the show distribution results in 22 considered cells.

3.5.3. Noise robustness

Noise is an inherent component of real measurement data and therefore affects the data analysis. In the following, the behavior of the three reconstruction algorithms w.r.t different noise levels and kinds of noise (uniform and Gaussian distributed) is shown. The simulation of every noise level was performed 10 times with different random noise contributions. The error bars of the curves represent the standard deviation of those simulations.

Figure 3.24 shows the evaluation parameters as a function of uniformly distributed noise amplitudes (% of the maximum data signal; Gaussian noise shown in the appendix A.9) for FBP. CAT10 is very unstable and for 7% of noise increases to factor 7 of the reference (= no noise) value (not shown here). EMT20 for a low noise level (up to 7%) on average remains close to the reference value with a standard deviation of up to ≈15%. EMS and BETX however up to 7% noise seem to be very robust though the EMS's average stays around +40%.
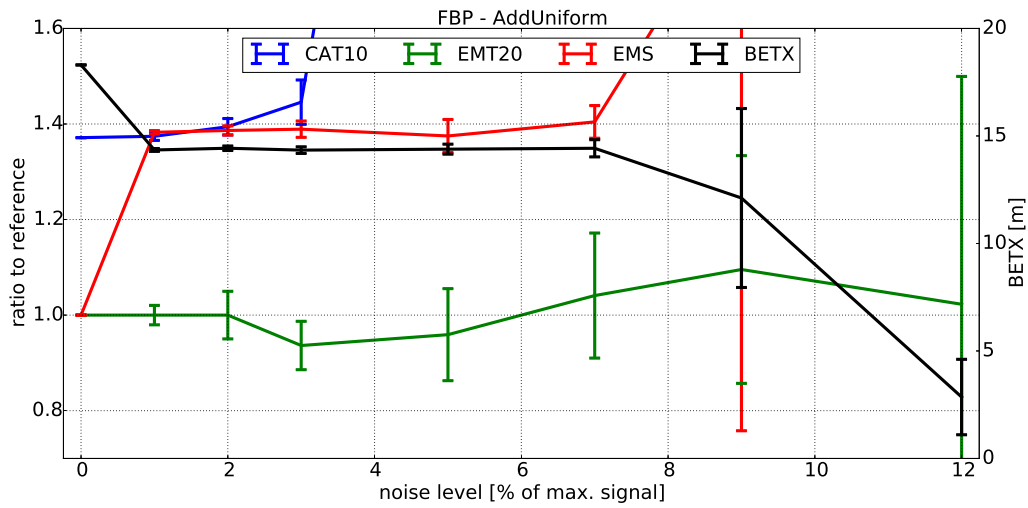
Figure 3.24.: FBP evaluation parameters for increasing noise amplitudes

Figures 3.25 and 3.26 show the sinogram and tomogram for none and 5% noise (amplitudes below the CAT10 level are colored in gray). The statistically higher artifact amplitudes of FBP superimpose with the noise and therefore more cells exceed the CAT threshold. The CAT10 raises from 48 to 116.
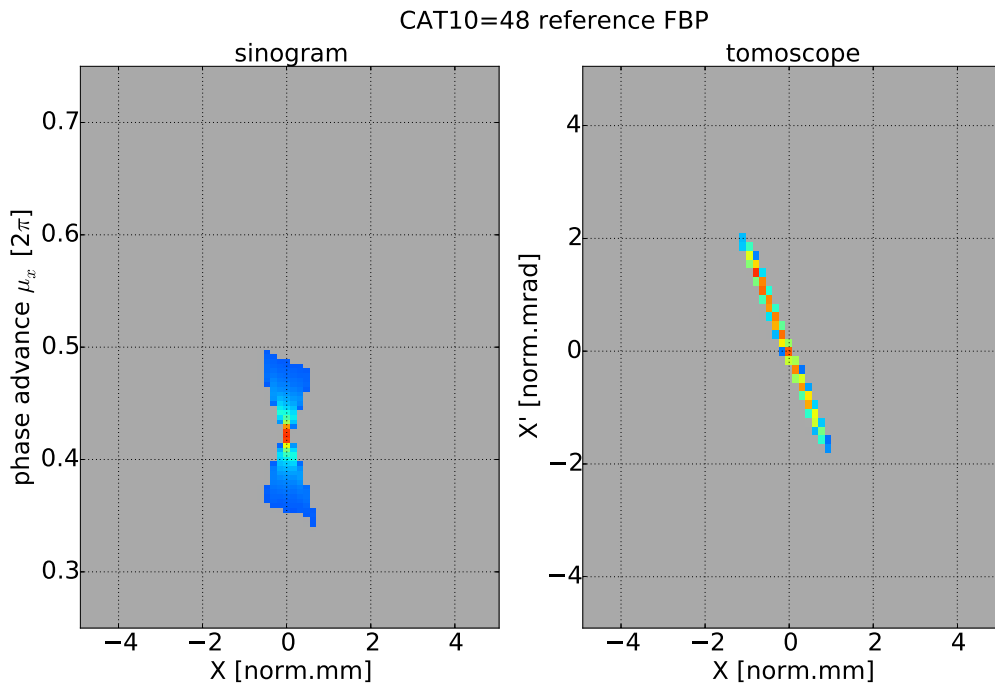

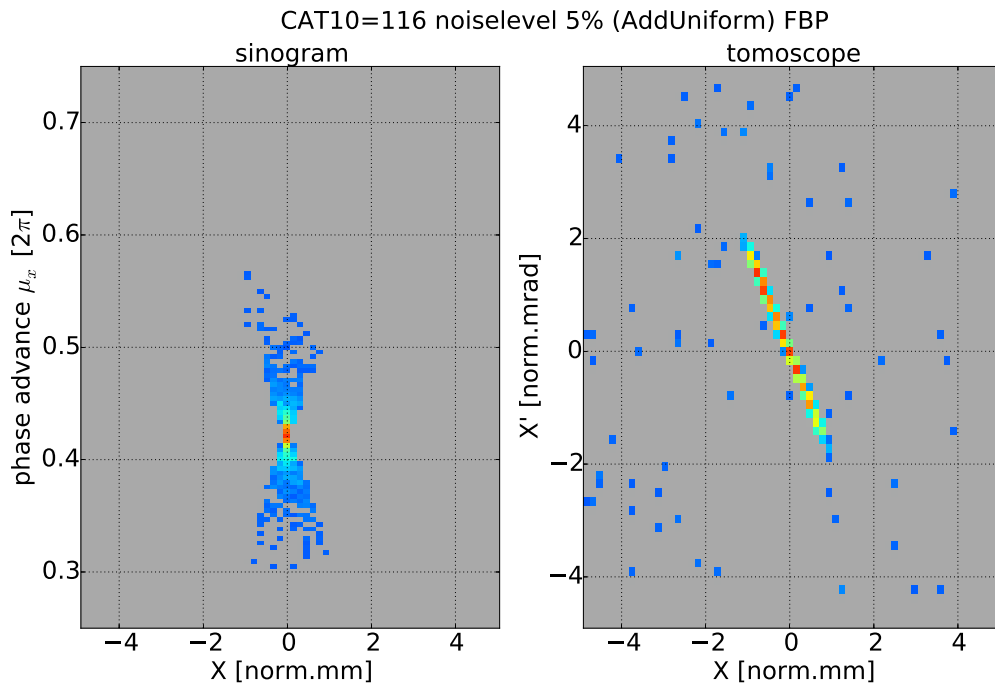Figure 3.25.: FBP sinogram and tomogram for 0% noise added

46

Figure 3.26.: FBP sinogram and tomogram for 5% noise added

The result for the MULT simulations (Figure 3.27 and A.10 in the appendix) compared to FBP are very stable. CAT10, EMS and BETX show a standard deviation of single percent up to noise levels of 9%. Figure 3.28 shows that even a very pronounced noise pattern of 12% noise amplitude in the sinogram results in an increase of CAT10 from 36 to 38 only. However, EMT20 becomes unstable very fast. Figure 3.29 shows the cumulative sum with 5% noise added and w.r.t. the reference (Figure 3.23(b)) the EMT20 raises from 22 to 41.

Figure 3.27.: MULT evaluation parameters for increasing noise amplitudes
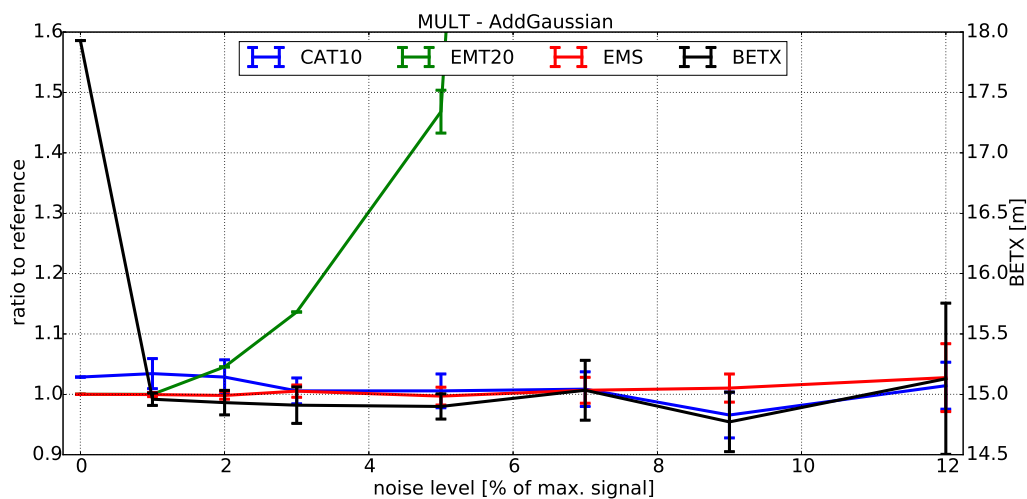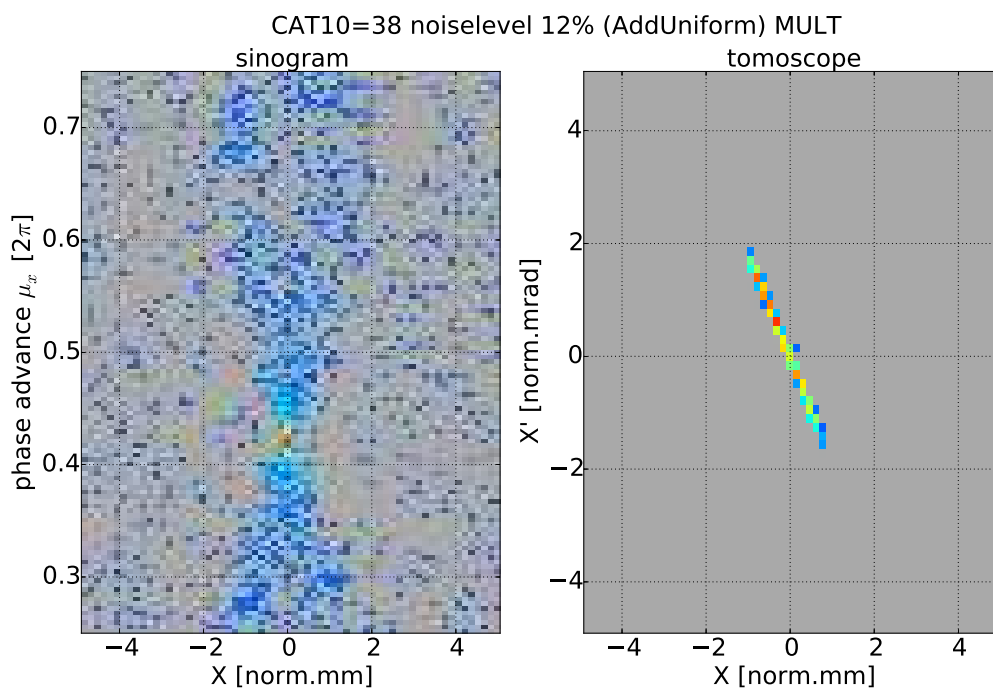
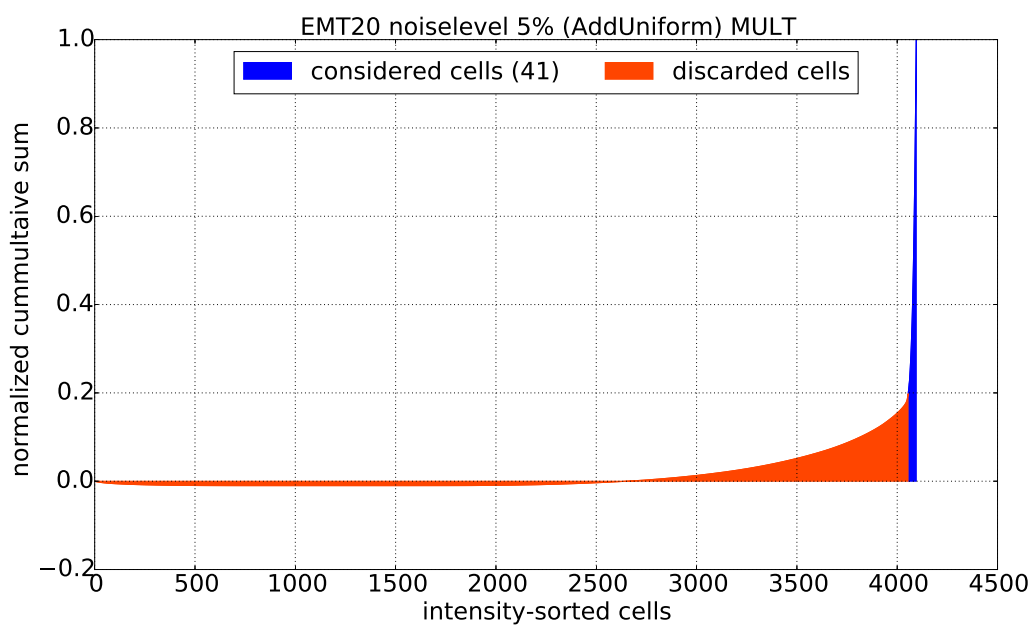Figure 3.28.: MULT sinogram and tomogram for 12% noise added

Figure 3.29.: MULT cumulative sum for 5% noise added

The SART reconstruction (Figure 3.30 and A.11 in the appendix) shows a stable behavior for EMS (+60%) and BETX, CAT10 becomes unstable with increasing noise while EMT20 remains at $\approx +40\%$ but with a larger standard deviation than FBP.
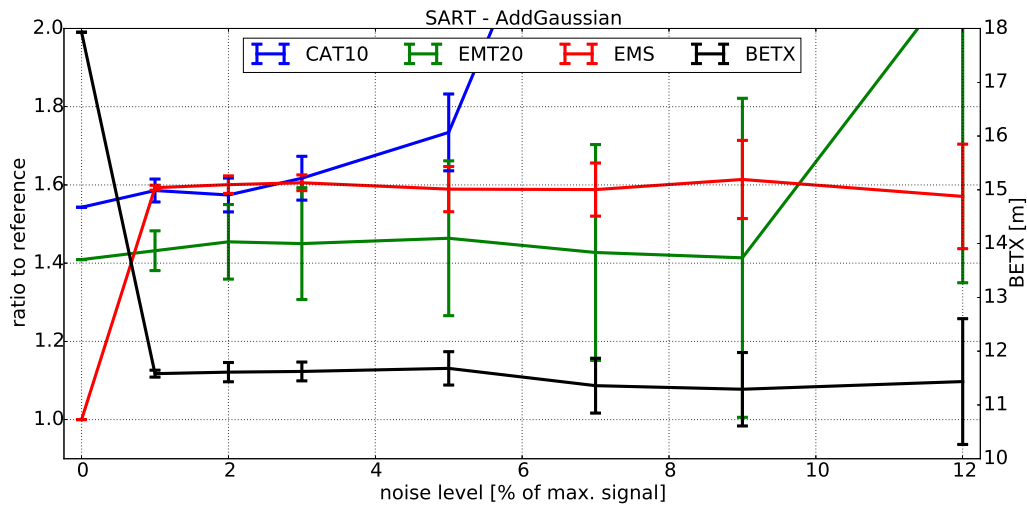
Figure 3.30.: SART evaluation parameters for increasing noise amplitudes

Table 3.1 summarizes the results of the simulations so far and provides reference values.

RECON	CAT10	EMT20	EMS	BETX	ALFX
SINO	160	1364	n.a.		
REF	35	22	5.5E-8	17.9	9.6
FBP	unstable	22	stable but +40%		
SART	unstable	+40%	stable but +60%		
MULT	35	unstable	5.5E-8	15.1	8.0

Table 3.1.: Simulation reference data

3.6. Profile centering

A particle entering the PSS module off-axis $(x/x' \neq 0)$ exits the module with varying phase space coordinates for the various PSS phase advances (rotation angles). Furthermore, due to magnet alignment errors, manufacturing inaccuracies or the limited amount of steering magnets or beam monitors a perfect on-axis beam setup for all rotation angles is impossible to achieve in reality. As a consequence the precondition of a common rotation axis for all projection angles is not fulfilled anymore[41].

---

[41]In a classical medical CT this would e.g. correspond to a moving patient while examination.

Therefore it is required to correct the achieved sinogram before reconstruction. Neglecting higher order effects of the quadrupole magnets of the PSS, the profiles can be 'realigned' to a common rotation axis by shifting the individual profiles appropriately. In this study, two mechanisms have been tested and evaluated: The projection profiles in the sinogram are centered either by centering the **center of gravity (CoG)** or the **geometric center (Geo)** of the profile. In both scenarios errors introduced by an asymmetry of the beam distribution are not considered. Furthermore, the profiles can only be centered by shifting the data of the profile in terms of entire bins[42].

For the Geo mechanism, a threshold is required again. Like for the CAT, the geometric center is computed at a certain amplitude level given as percentage of the maximum. For this study, 30%, 50% and 70% are used.

Figure 3.31 shows the result of centering the reference sinogram. Ideally this sinogram is not changed which is the case for the CoG mechanism. The Geo-corrected sinograms show a shift of some projections by one pixel.
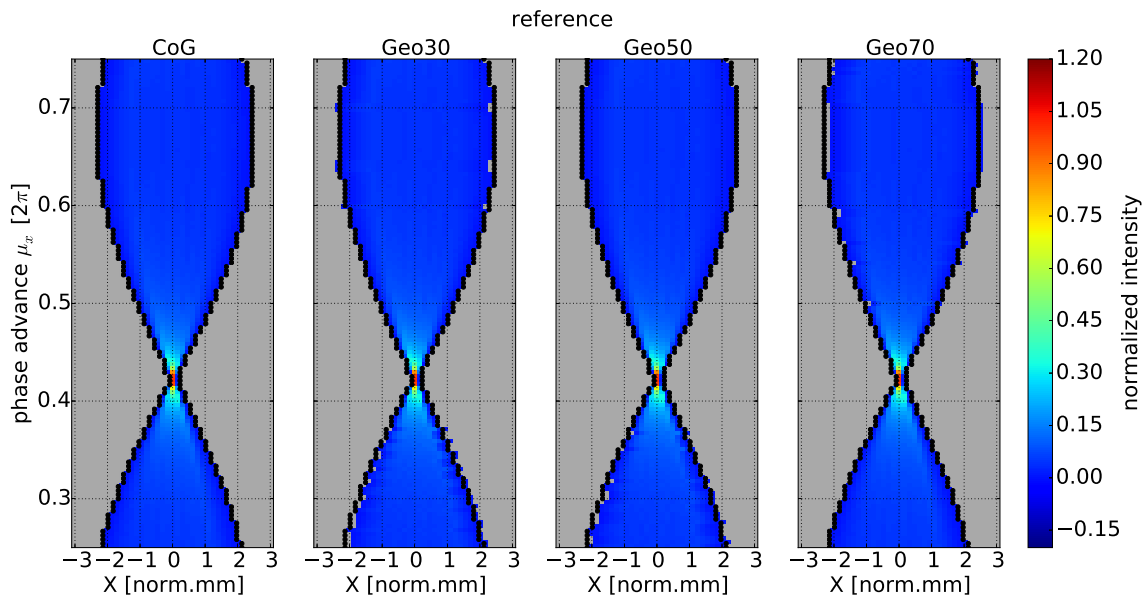
Figure 3.31.: Sinograms resulting of centering the reference sinogram

The results of the evaluation of the resulting tomograms are shown in Figure 3.32. Whereas EMT20 and CAT10 are not or only slightly affected, the values for EMS, BETX and ALFX change by about 10%. From the centering perspective, all mechanisms provide very similar results.

---

[42]Reflecting to the used SFX model, only shifts of 1mm (real space) = one fiber are allowed.
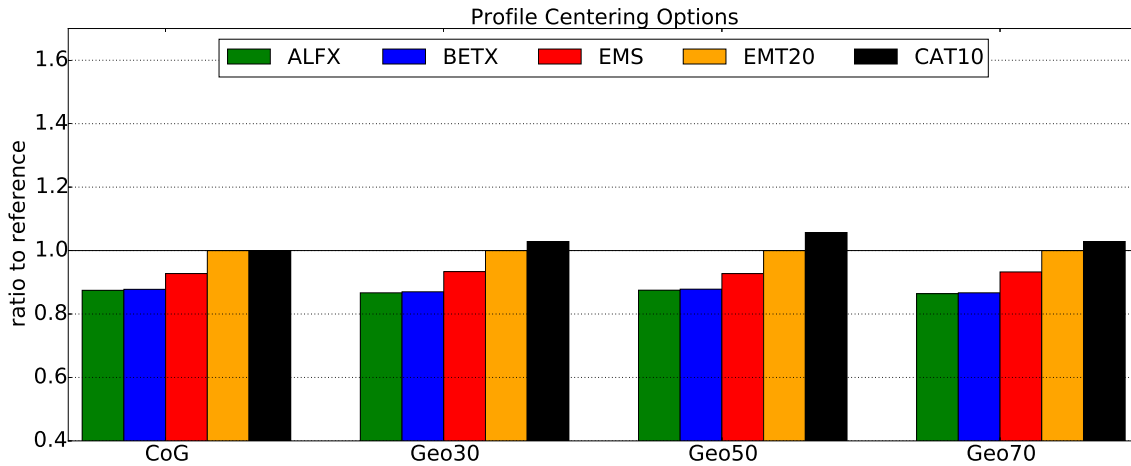
Figure 3.32.: Comparison of reconstruction parameters vs. centering mechanisms after centering the reference sinogram

Furthermore, the centering mechanisms have been tested with a particle distribution intentionally misplaced at the beginning of the transfer line by 200urad and 1mm. The resulting uncorrected sinogram is shown in Figure 3.33 (center). The right chart of this figure shows the resulting sinogram after CoG correction.
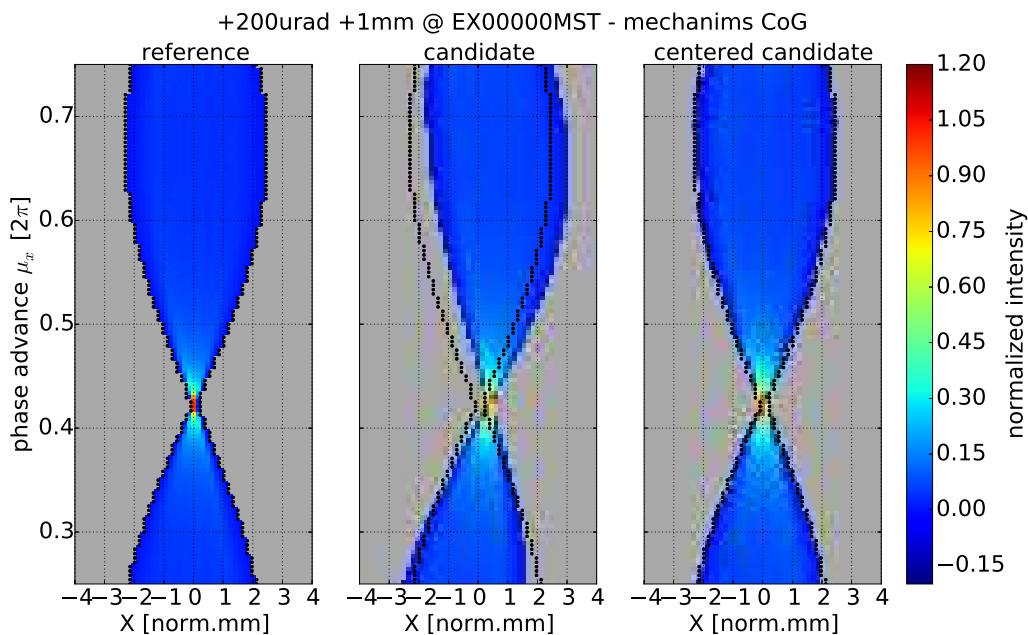

Figure 3.33.: Reference, uncorrected and CoG corrected sinogram of an off-axis particle distribution

Figure 3.34 presents the sinograms of the off-axis particle distribution corrected by the four mechanisms (CoG, Geo30, Geo50, Geo70). All of them present a straight-

ened sinogram with some projections shifted by single pixels w.r.t the centered reference.
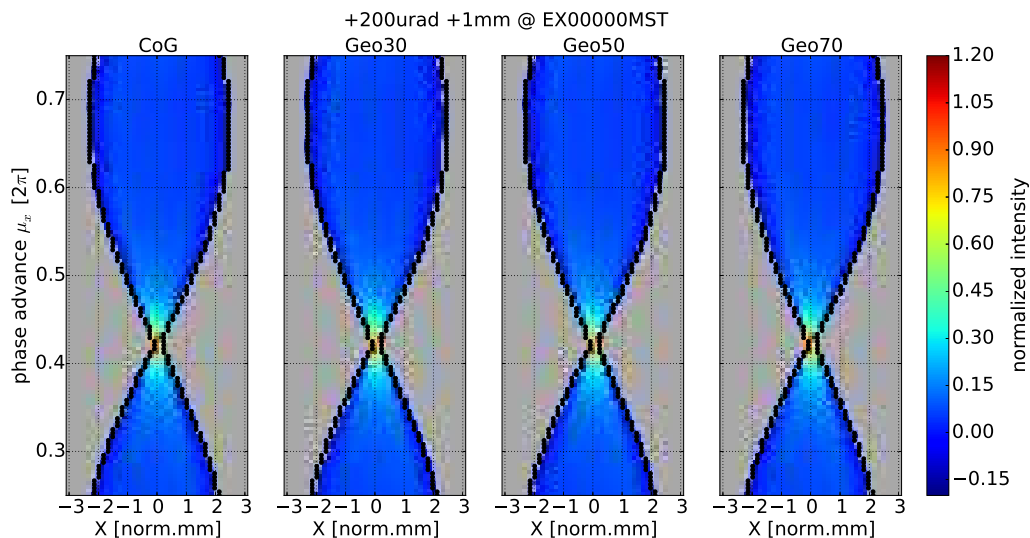
Figure 3.34.: Sinograms resulting of centering the off-axis sinogram

After computing the reconstruction for the various cases however, it turns out that the evaluation parameters are affected a lot (see Figure 3.35). EMT20 for all centering mechanisms are increased by $\approx 50\%$ while BETX and ALFX values are decreased by $\approx 40\%$. In this comparison, the CoG mechanism provides the best reconstruction but still EMS ($+12\%$) and CAT10 ($+22\%$) are affected.

Figure 3.35.: Comparison of reconstruction parameters vs. centering mechanisms after centering the off-axis sinogram

Visually, the reference (Figure 3.36(a)) and the CoG-centered tomogram of the off-axis distribution (Figure 3.36(b)) present a quite high similarity. This indicates

that the selected evaluation parameters CAT, EMT and EMS (with BETX/ALFX) are not robust w.r.t. the centering process.
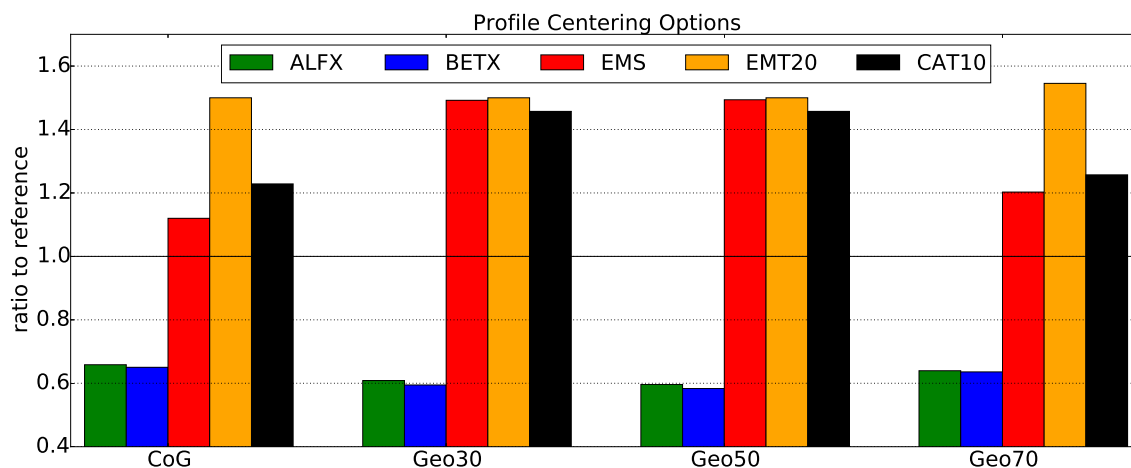

(a) Tomogram of reference particles

(b) EMT20 evaluation (based on MULT)
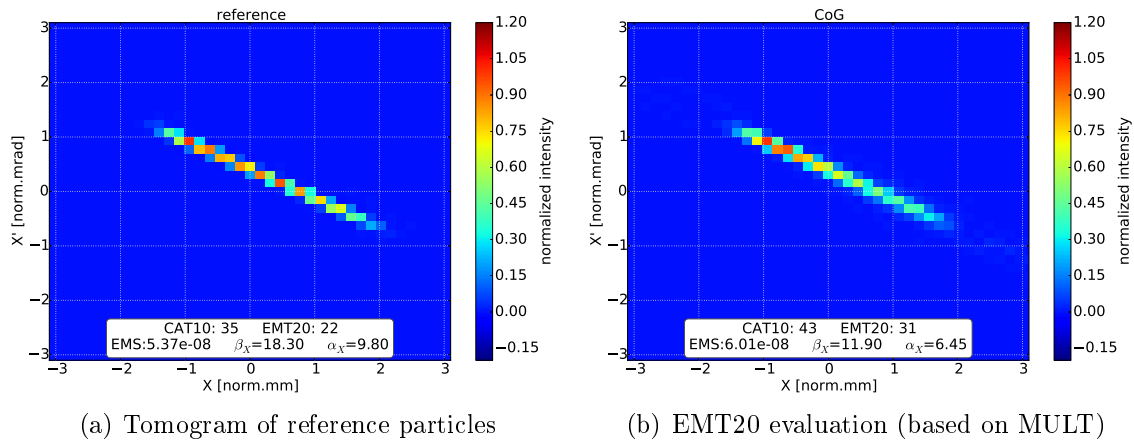
Figure 3.36.

More details on this phenomenon are shown in Figure 3.37: in these simulations the binning of the BPM is shifted in a range of ± 1.4mm which corresponds to the particle distribution being detected in different intensity patterns (depending on how the particle distribution is distributed on the monitor fibers). The chart shows a repetitive wave-like structure repeating every millimeter which correlates to the 1mm binning of the used SFX fiber grid. As already shown before the centering mechanism worsens the result of the evaluation parameters (Figure 3.38).

Figure 3.37.: Evaluation parameters as a function of bin shift - not centered

Figure 3.38.: Evaluation parameters as a function of bin shift - centered (CoG)

4. Measurements

The following chapter describes the beam measurement results performed at the MedAustron synchrotron measuring on two separate monitors. Furthermore, a time resolved analysis is presented.
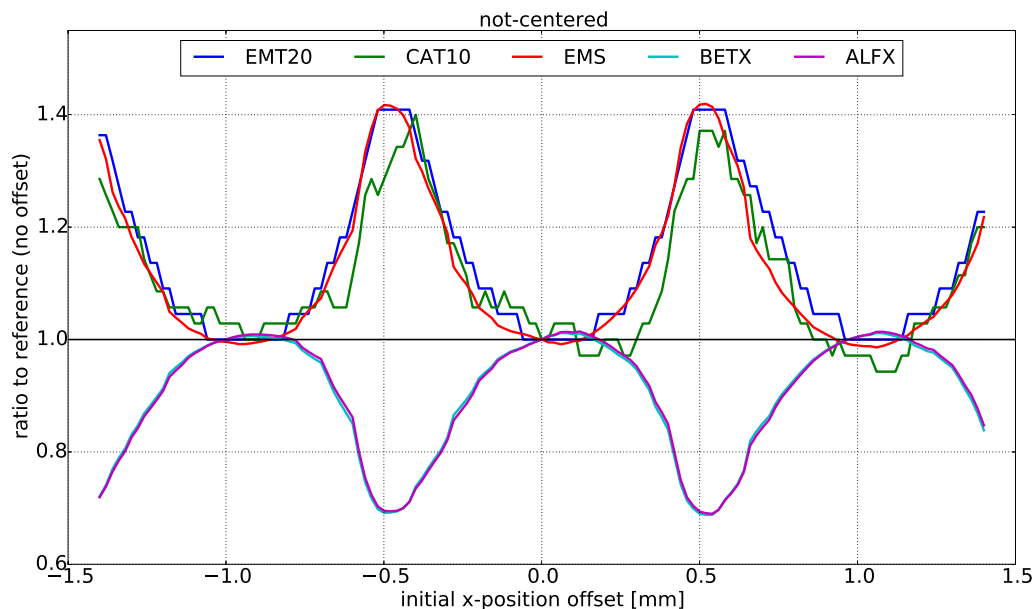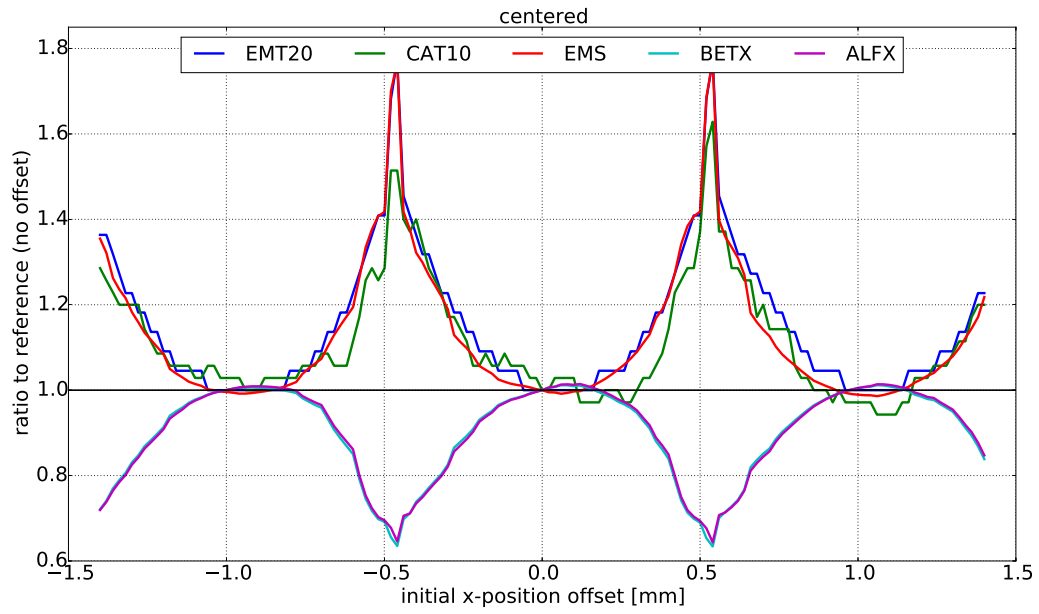
4.1. Tomogram at EX01003SFX

For the measurements, proton beams with a kinetic energy of 252MeV, a spill length of 5 seconds and an average of 9.7E9 particles per spill (standard deviation: 5.8E8) in the synchrotron were used and measured on EX01003SFX with an exposure time of 60ms per frame and 10 frames per second. In order to compensate for intensity fluctuations in the accelerator, the beam profiles intensities were normalized to the synchrotron intensity measured via a current transformer (CTS). Figure 4.1 (upper chart) shows this value as a function of phase advance[43] as well as the corresponding correction (scaling) factor. The bottom chart shows the corresponding full-width at half maximum (FWHM)[44].

---

[43]SID is an acronym for Settings IDentifier and represents the 120 different phase advance settings use for the measurement. $\mu_{(}x - SID) = 0.25 + SID * \frac{\pi}{nr.of angles}$

[44]For the measurements, the OpApps measurement framework[65] (version 1.9) was used where as the analysis of the single measurement files was performed via the measurement data analysis framework PACMAN[66] (version 1.4.1). The radiation damage of the fibers have been compensated[67].
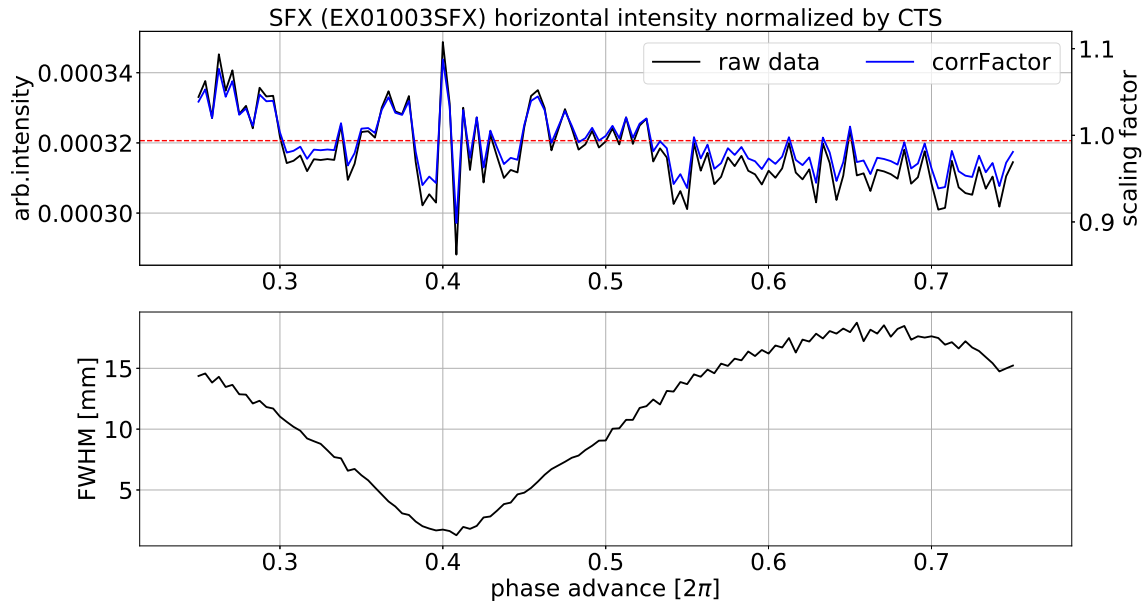
Figure 4.1.: BPM intensities normalized to synchrotron intensities and FWHM as a function of phase advance

Remark: For the phase advance = 0.40833 the FWHM is the smallest and almost all the extracted particles are accumulated in only a single fiber which seems to have saturated the according monitor camera pixel. Therefore, in this case only the intensity value of this single fiber was corrected instead of the entire profile.

Figure 4.2 shows the sinograms from the simulations as well as from the measurements (not-centered and centered via the CoG-mechanism). During commissioning of the transfer line[68] the steering of the beam trajectory for only one phase advance setting was optimized. Remaining with this single setting for all phase advances used in this study resulted in beam losses. Therefore phase advance dependent steering magnet settings were introduced to ensure that the particles of all settings reach EX01003SFX.

Comparing the sinograms of the simulations and the centered measurements, one can see that a) the minimum and maximum width of the sinograms are of very similar size, b) the intensity gradient at the highest intensity peak as a function of phase advance seems smaller for the measurement than for the simulation and c) the smallest width is shifted in phase advance.
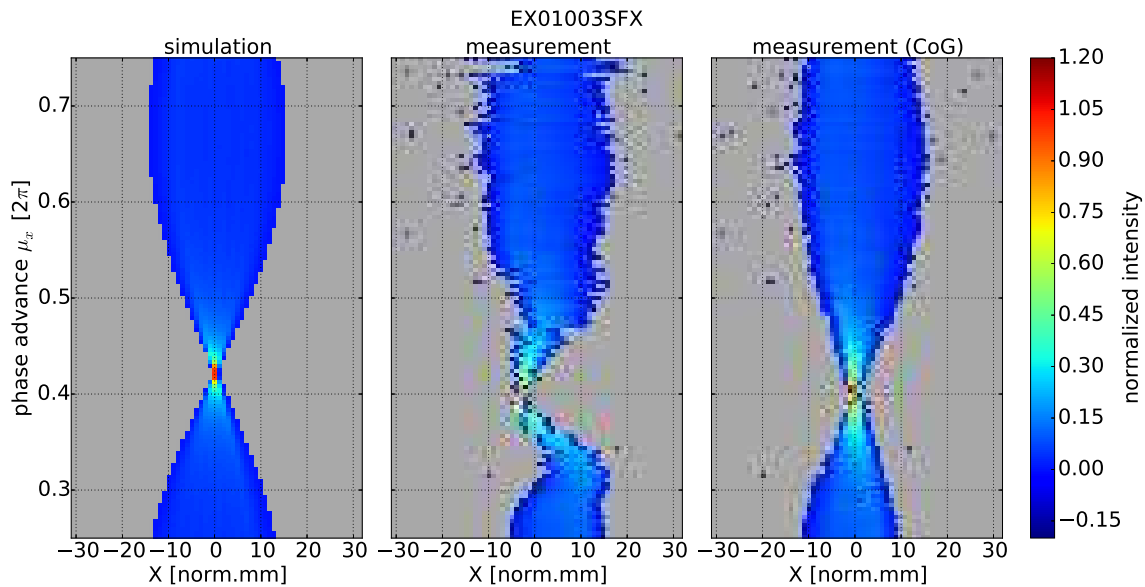
Figure 4.2.: EX01003SFX: simulation, the measurement and centered measurement sinograms

In detail, this can be seen in Figure 4.3 presenting the simulated and measured profile for the phase advance with the smallest simulated profile accumulating all particles in a single fiber (*bar of charge* standing upright). The measured profile however covers multiple fibers (see Figure 4.8 for the smallest measured beam profile).

The in-depth analysis of the sinograms are shown in figures 4.4 and 4.5. The CAT10 of the simulated (160) is very different than the measured one (491) where as the EMT20 is more similar (1364 vs 1091).
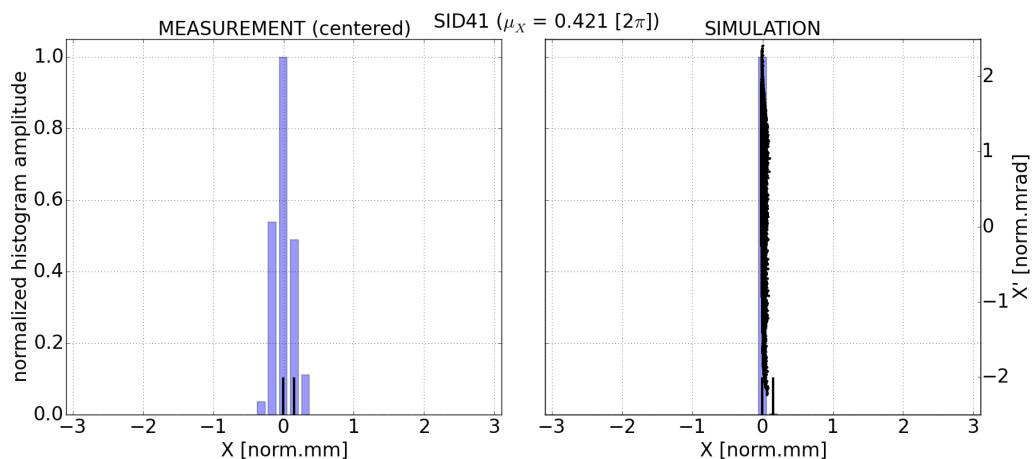
Figure 4.3.: EX01003SFX: simulated and measured profile for one phase advance

(a) Simulated sinogram

(b) Measured and CoG uncentered sinogram
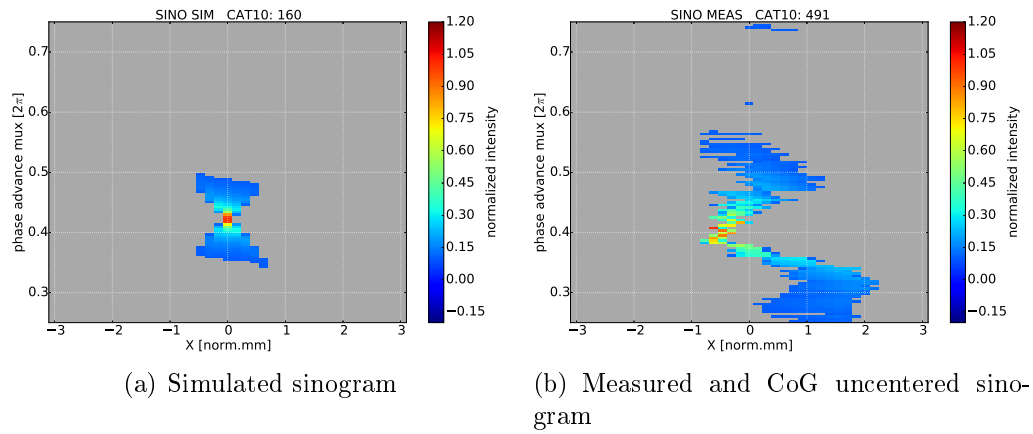
Figure 4.4.: CAT analysis of sinograms

(a) Simulated sinogram

(b) Measured and CoG centered sinogram

Figure 4.5.: EMT analysis of sinograms

Figure 4.6 shows the simulated and measured tomogram reconstructed via MULT while Figure 4.7 presents the FBP tomograms. The CAT and EMS value are almost identical whereas EMT20 is larger for the measurement. This indicates a different intensity structure inside the bar of charge with less high intensity pixels.

(a) Simulation (b) Measurement
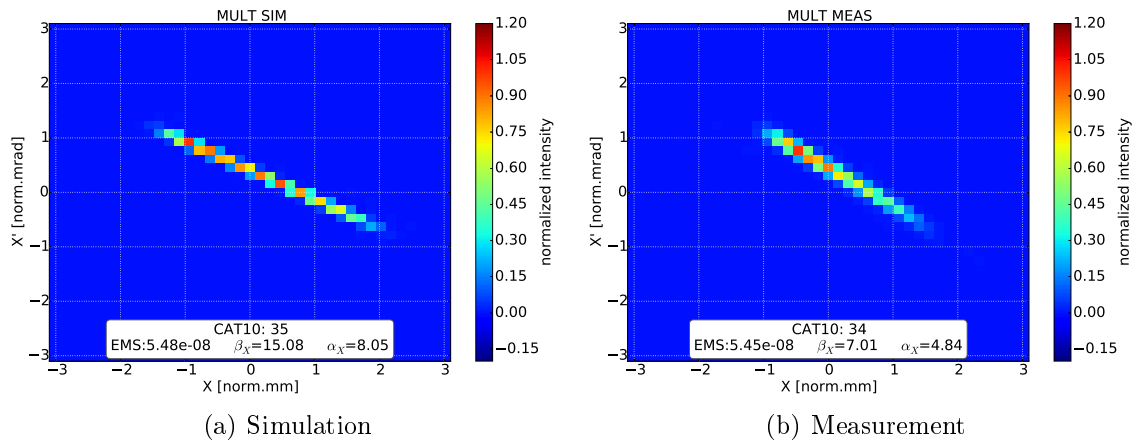
Figure 4.6.: Comparison of MULT reconstructed tomograms

(a) Simulation (b) Measurement
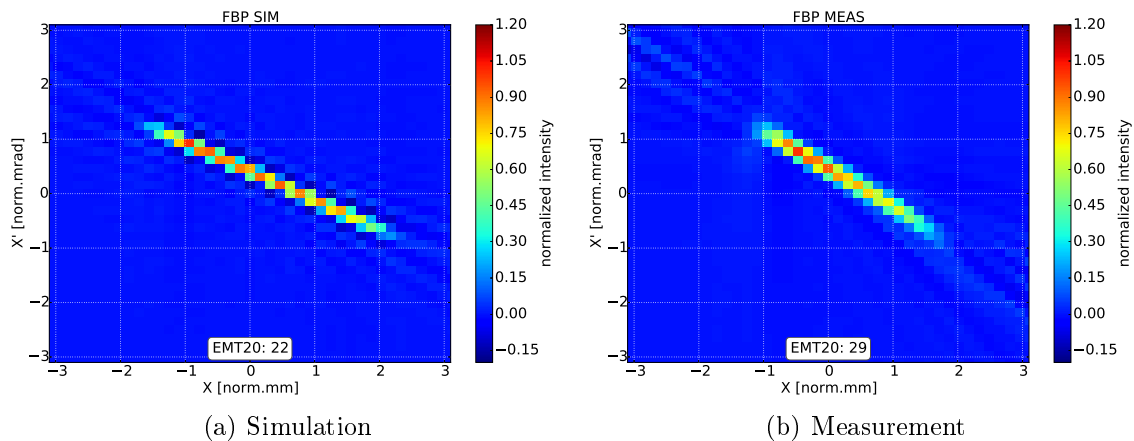
Figure 4.7.: Comparison of FBP reconstructed tomograms

Furthermore, the BETX and ALFX values are smaller for the measurement than for the simulation; also visually the bar is 'shorter' along the long axis. As CAT and EMS are about identical, the measured distribution has to be wider along the short axis. This matches with Figure 4.8 showing the smallest measured profile which contributes to more than a single fiber.

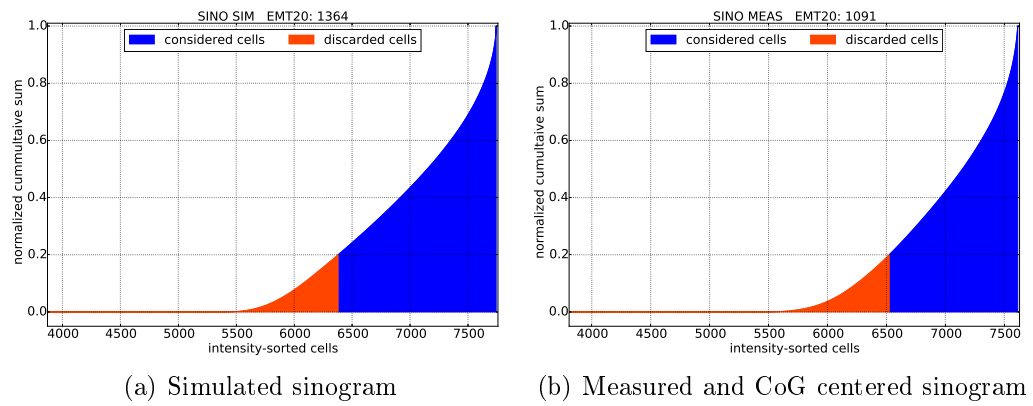Also in the tomograms one can identify a minor phase advance difference as the two bars show a slightly different rotation.
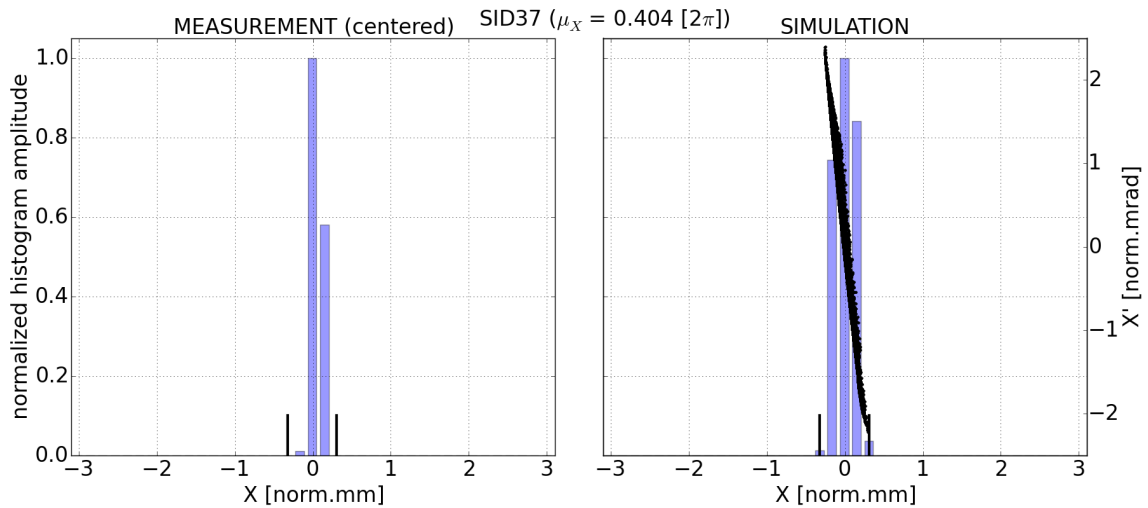
Figure 4.8.: EX01003SFX: simulated and measured profile for one phase advance setting

Finally, Figure 4.9 summarizes the described findings in a comparison of the two 3D models (simulated, measured).
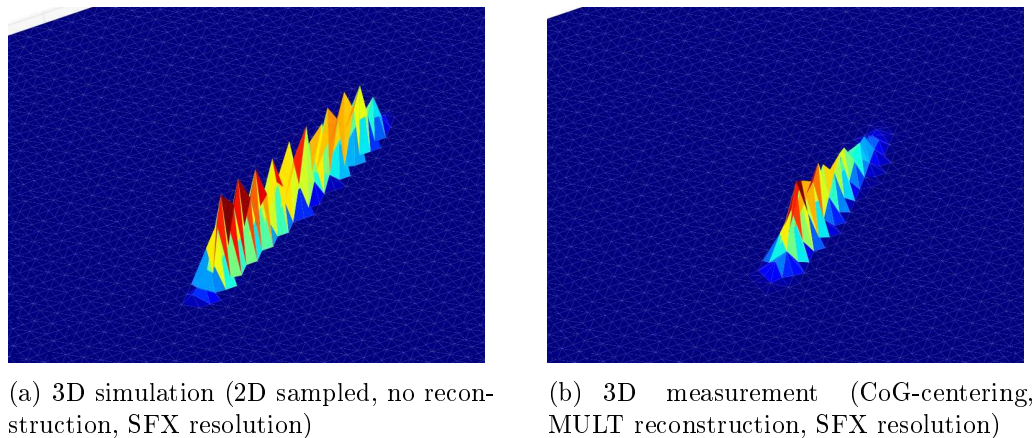
(a) 3D simulation (2D sampled, no reconstruction, SFX resolution)

(b) 3D measurement (CoG-centering, MULT reconstruction, SFX resolution)

Figure 4.9.

4.1.1. Time resolved analysis

As described, the particles were extracted from the synchrotron in a time window of 5 seconds per measurement angle while the SFX data acquisition rate was set to 10 frames per second. This results in 50 intraspill beam profiles, sinograms and therefore tomograms. Figure 4.10 shows a time resolved analysis of those tomograms.
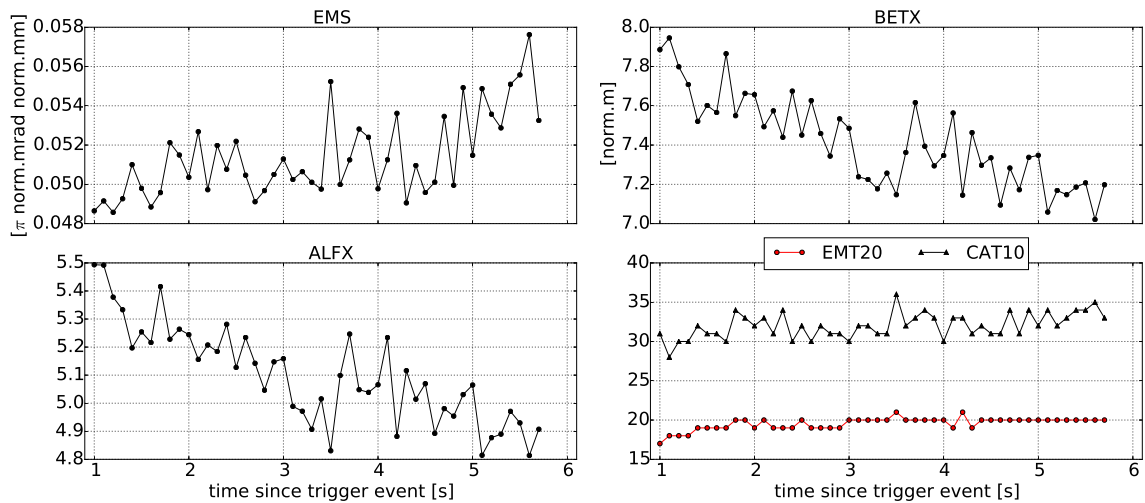
Figure 4.10.: Time resolved tomographical characterization of an extracted particle
spill

For the interpretation of this data one has to consider that 120 spills contribute to
these intraspill tomographies. Figure 4.11 shows the time resolved intraspill profiles
of four spills. Obviously the extracted flux (particles per time) varies from spill to
spill affecting the intraspill tomographical reconstructions - the resulting evaluation
parameter values have to be questioned.
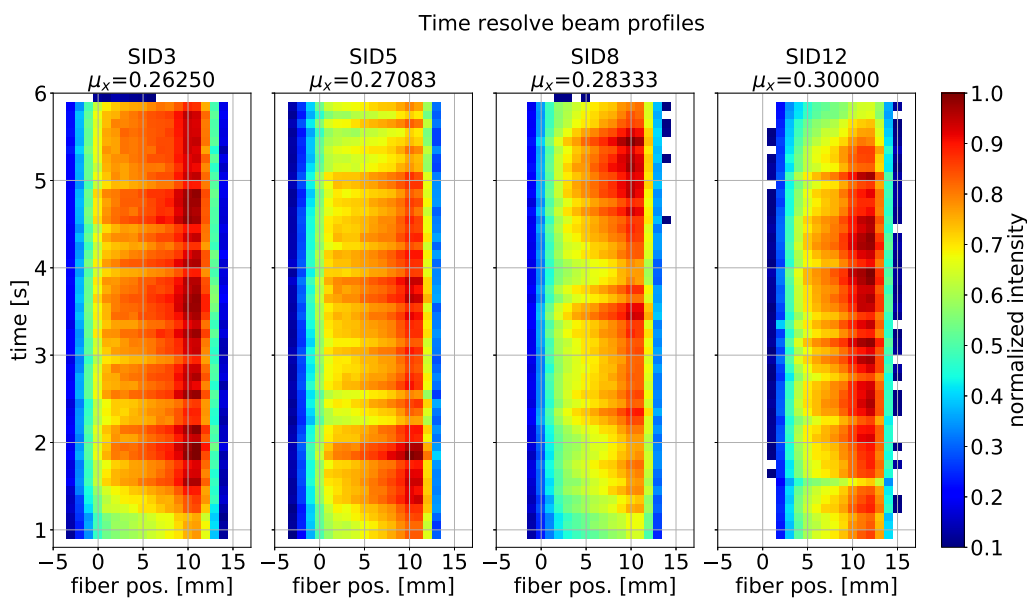
Figure 4.11.: Intraspill profiles of four spills on EX01003SFX

4.2. Beam optics considerations

Inside the phase shifter stepper module, another BPM (EX01002SFX) is installed. The phase advances and beta functions are not matched to compile a set of data ready for tomographical reconstruction. However, the profiles for the various settings for the tomoscope have been recorded for a subset of 60 phase advances (every second setting of the tomography at EX01003SFX). Figure 4.12 shows the sinograms of the simulation, the measurement and the centered measurement indicating that the pattern of wide and small beam regions approximately match[45].
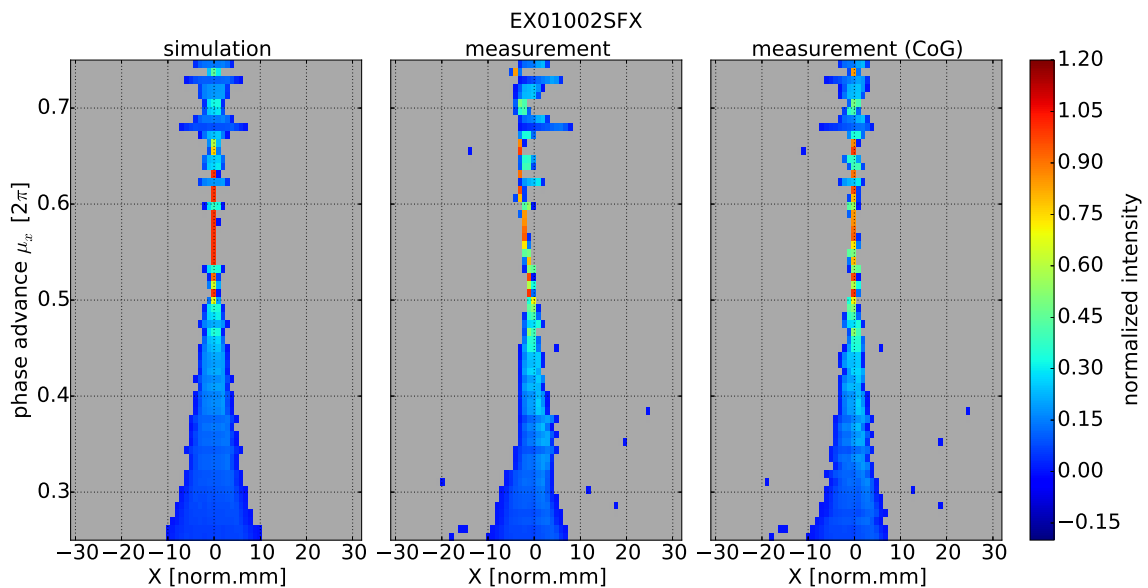
Figure 4.12.: Sinograms for simulation and measurement (not-centered and CoG-centered) for EX01002SFX (horizontal plane)

Figure 4.13 presents two curves: the vertical beta function (black) as well as the FWHM^2 of the measured beam in vertical plane (red) at EX01002SFX, both normalized to the value of the first phase advance setting[46]. As the curves match very well it can be assumed that the beta functions of the model match well the real machine behavior.

---

[45]Also, on this monitor multiple quadrupole settings result in a upright standing bar of charge accumulating all particles in a single fiber (see Figure A.15).
[46]$FWHM = 2.36 * \sqrt{\epsilon\beta} \propto \sqrt{\beta}$

Figure 4.13.: Measured (approximation) and simulated vertical beta functions for EX01002SFX, normalized to first/lowest phase advance setting)

At EX01003SFX (vertical plane) the match however looks different. The general correlation is correct but especially for larger beam sizes, but not only there, is a less well matching behavior visible. Figure 4.15 shows the beta functions of a subset of less well matching phase advance settings distributed over the entire phase advance range inside the PSS module. Especially in the vertical plane (bottom) the chart shows that also low amplitude BETY functions are part of this subgroup (as Figure A.16 shows the same for 'good' cases) indicating that the lower measured amplitudes do not originate from beam scraping.

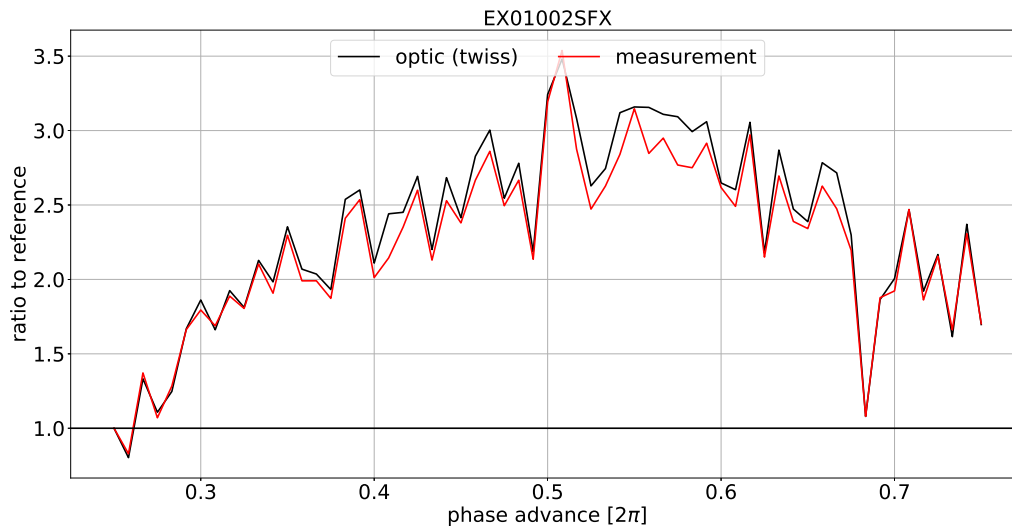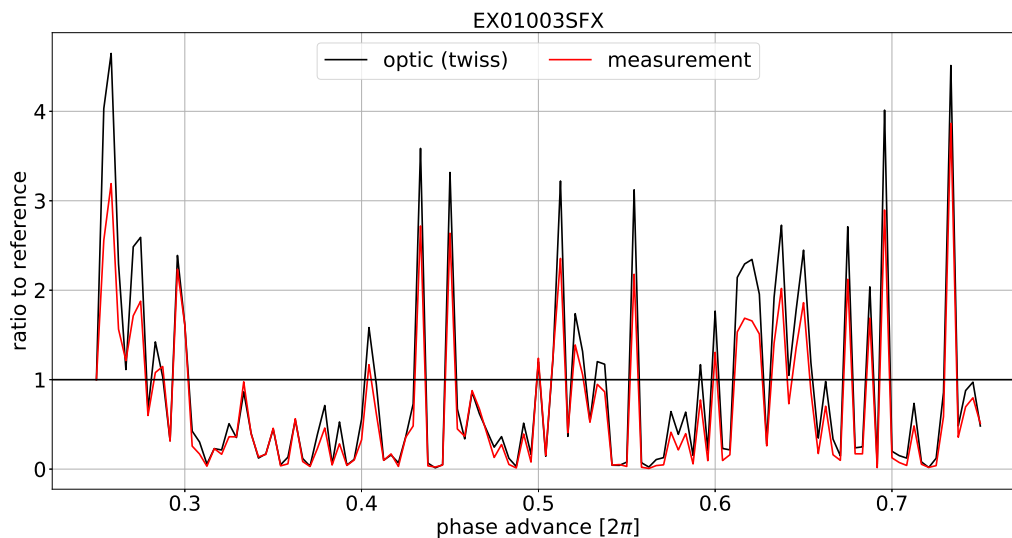Figure 4.14.: Measured (approximation) and simulated vertical beta functions for EX01003SFX, normalized to first/lowest phase advance setting)
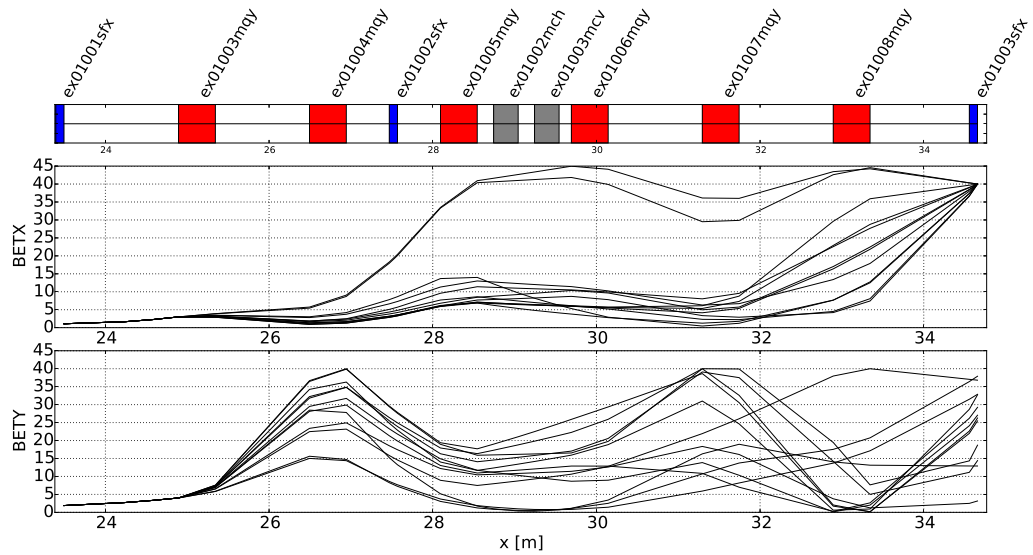
Figure 4.15.: Beta functions of 'bad' cases (w.r.t. 4.14) inside the PSS module

To conclude, it rather seems like that the theoretical optics model used for the simulations doesn't match the real lattice functions perfectly.

5. Conclusions

This research aimed to provide some empirical evidence of the 'bar of charge' concept of a slow third order slow resonant extracted particle beam from a synchrotron. The simulations and measurements were performed following a data acquisition procedure based on the PIMMS Phase Shifter Stepper concept while tomographical reconstruction techniques were used for the analysis.

The data presented in table 5.1 illustrates that important quantification parameters of the particle distribution in the horizontal phase space concur between a (simulated) reference as well as reconstructions using simulated and measured data. Figure 5.1, by way of example, visually depicts the similarity of simulated and measured reconstruction results.

Result	CAT10	EMT20	EMS	BETX	ALFX
Reference	35	22	5.5E-8	17.9	9.6
Simulation	35	22	5.5E-8	15.1	8.0
Measurement	34	29	5.45E-8	7.0	4.8

Table 5.1.: Comparison of simulation and measurement results

Therefore, this method would appear to be well suited to enlarge the range of existing commissioning procedures at MedAustron or other accelerator facilities, depending on their beam line layout. While the reconstruction based on integrated beam profiles can be used for e.g. (static) optics optimization, the time resolved analysis provides the option to study the (dynamic) intraspill behavior of the beam.
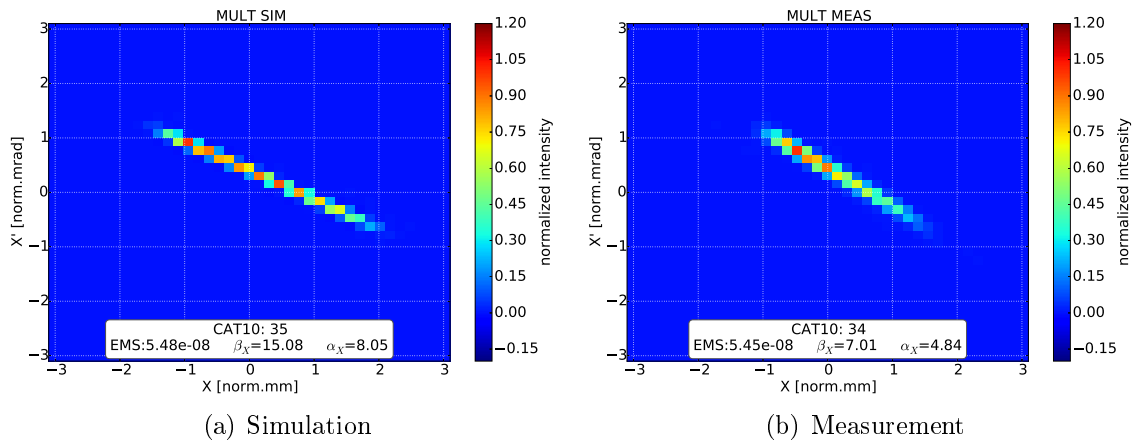
(a) Simulation
(b) Measurement

Figure 5.1.: Comparison of MULT reconstructed tomograms

However, the measurements gathered within the framework of this thesis would appear to show certain deviations from the simulation (e.g. different orientation and length of the reconstructed distribution). Also, due to the aforementioned dependency of the quantification parameters on the beam centering mechanism, the values presented in table 5.1 should be considered with reservation. To better understand the implications of such deviations and therefore limitations for the used methods, future studies should address the following potential sources of errors:

- SFX radiation damage: The fibers of the scintillating fiber grid beam profile monitors have been exposed to radiation during the commissioning of the MedAustron accelerator resulting in a loss of sensitivity of the most intensively used fibers. Figure 5.2 shows the sensitivity profiles of EX01003SFX as an estimate of two different 'in-vivo'[47] determination procedures performed by the author (AWL) and a beam diagnostic expert[67] (CKU)[48]. Besides the fact that the curves of both methods cannot substitute an appropriate calibration of the measurement device, the chart illustrates the quality of the effect as well as the uncertainty of the correction values[49].

---

[47] The device was not disassembled from the accelerator and characterized with a reference source but the proton beam in the accelerator itself was used.

[48] For this study, finally the blue curve of CKU was used to compensate for the radiation damage.

[49] This effect represents the most likely explanation for the measured distribution being 'shorter' than the simulated bar-of-charges.
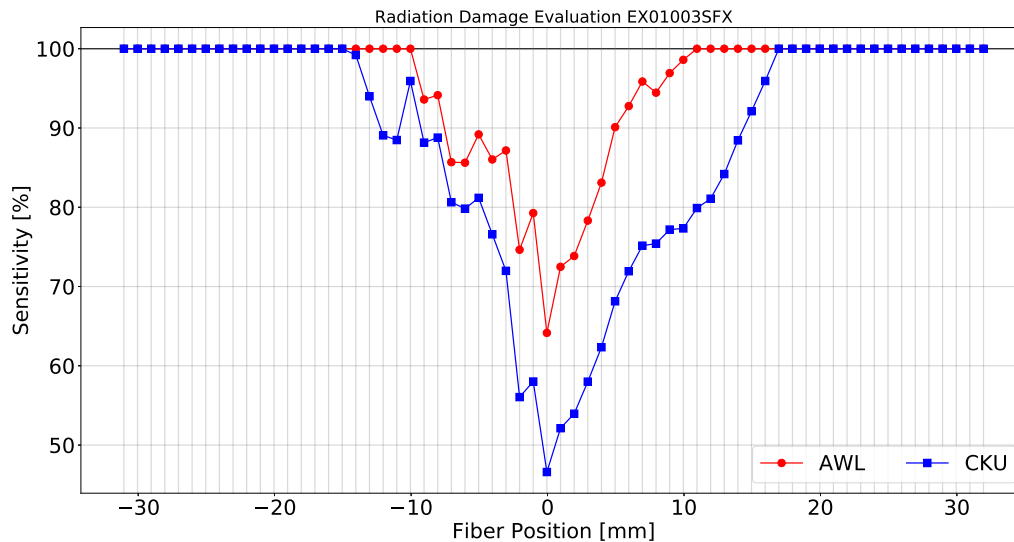
Figure 5.2.: Radiation damage of fibers on EX01003SFX, two different methods at two different points in time

- Settings of beam profile monitors: As part of the measurement procedure, the entire beam intensity once is focused onto a single BPM fiber while in the 90 degree phase advance case the intensity is distributed over more than 20 fibers. Proper settings of the exposure time and amplification gain must be found. For this thesis it seems that the scenario of fully focused beam caused a saturation of the camera pixel which was compensated by normalization of the measurement data. However, settings should be found to avoid this deficiency.

- Magnetization concept: To achieve all required measurement setups, some magnets for some phase advances were operated in focusing polarity, for other phase advances in defocusing. The current accelerator control system however only supports one current-to-field (BI) transfer function. For operation therefore the two curves of the hysteresis where averaged introducing several percent of offset between the computed and the applied magnet gradients. Those offsets affect not only the phase shifter stepper settings but all components leading to errors on the beam optics of the incoming beam, the phase shifter stepper matching as well as the normalization process of the measurement data[50].

- spill to spill reproducibility: The intraspill beam intensity fluctuations correspond to a moving patient in a hospital CT scenario. For the 'simple' reconstruction using the summed projection of the entire spill those fluctuations may be averaged out but for the time resolved analysis they have a major impact.

---

[50]Therefore for the author this is the most likely explanation for the different orientation of the phase space distribution between simulation and measurement.

- centering procedure: besides the fact that phase advance dependent steering magnet settings indicate that the incoming beam into the phase shifter stepper module is setup sub-optimally, the strong dependency of the quantification parameters on the centering mechanism can be addressed by increasing the detector resolution. Multiple measurement points along the short half-axis of the distribution would be helpful[51]. Alternatively the optics can be matched to an even larger beta function 'zoom' than 3m in - 40m out[52].

Though, even after having reflected on the mentioned limitations, the required time for an measurement is still 120 spills[53] per beam modality (e.g. particle type, particle energy, ...). Therefore this procedure seems to be rather applicable for commissioning or optimization of an accelerator or characterization of a new extraction driving mechanism than as a routinely performed QA measurement.

---

[51]Indeed, an extraction scheme fulfilling the Hardt condition resulting in an approximately 1mm wide beam distribution (like at MedAustron) is more challenging than other schemes resulting in a broader distribution.

[52]At MedAustron, the limiting factor for this is the large vertical emittance which is off w.r.t. design by more than factor 2. The large emittance limits the range of vertical beta function values inside the phase shifter stepper and therefore also the horizontal (strong quadrupole gradients affect both planes).

[53]Currently, the preparation of the accelerator (quadrupole settings) as well as the measurement of one phase advance itself takes about one minute at MedAustron.

A. Appendix

(a) 1 angle   (b) 32 angles   (c) 127 angles
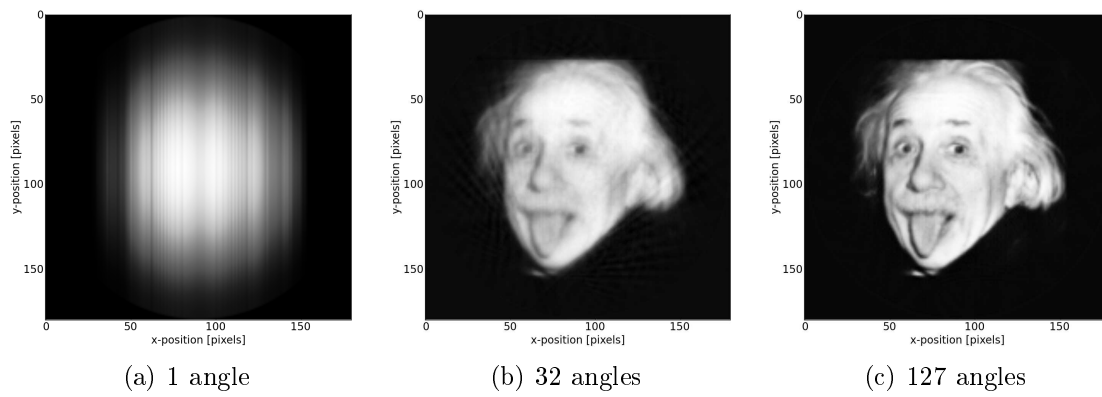
Figure A.1.: SART reconstruction for different numbers of projection angles Θ
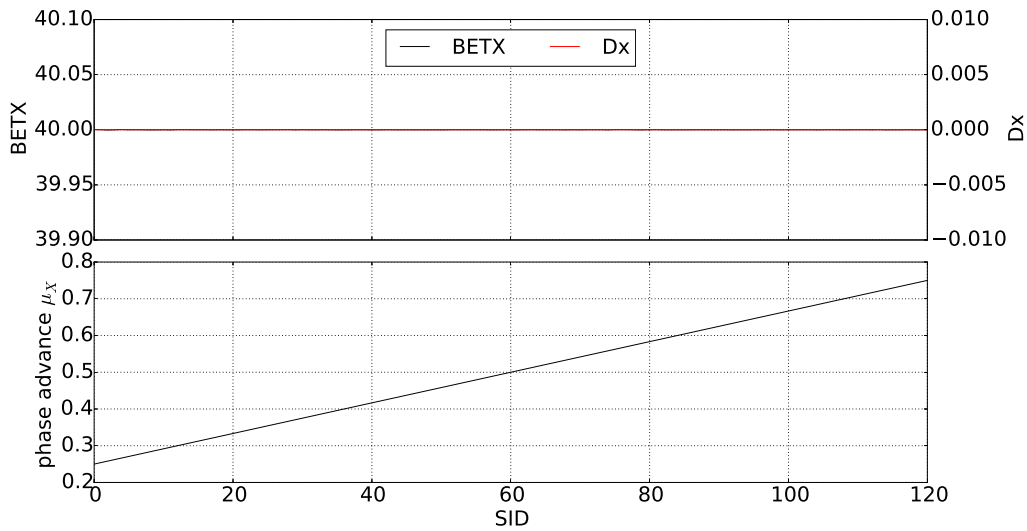
Figure A.3.: For all phase advances (numbered by SID), the BETX was matched to 40m and dispersion Dx = 0.
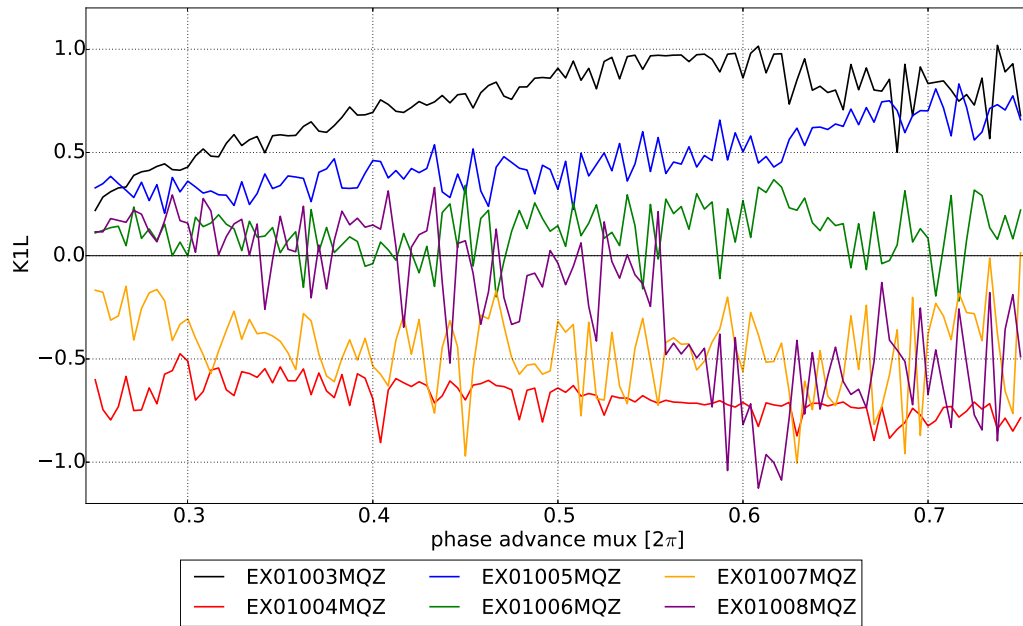
Figure A.2.: Strength settings of the six quadrupoles of the PSS for various phase advances. The change of polarity for measurements is considered via adaptation of the magnet conditioning (hysteresis). All MADX matchings have achieved a tar-value of $< E - 18$
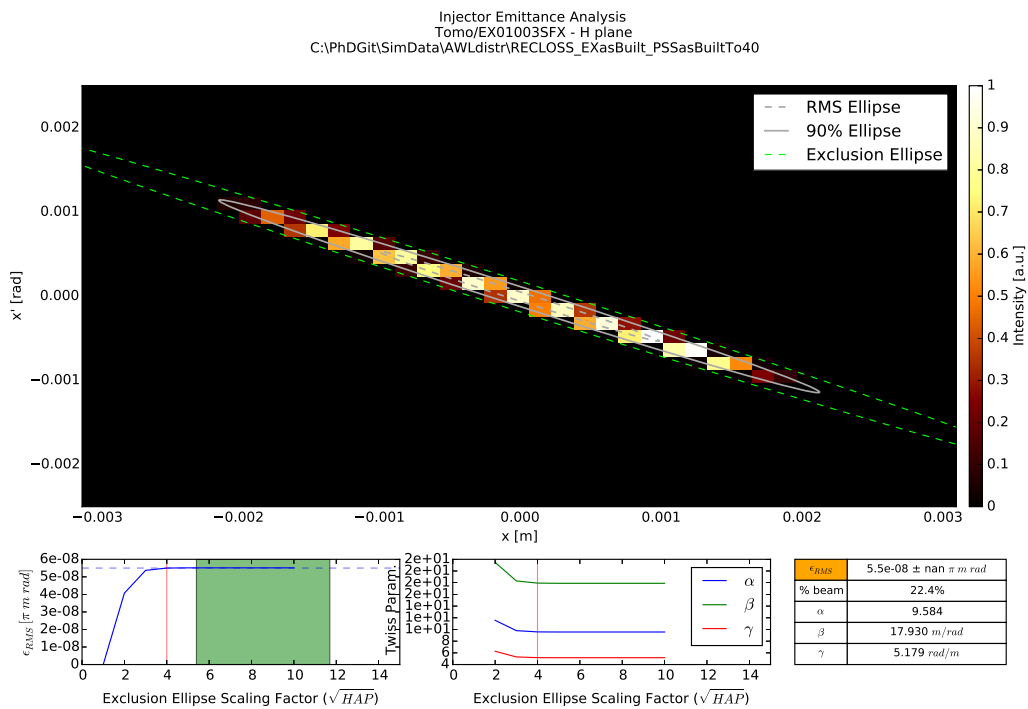
Figure A.4.: SCUBEEx analysis result of the reference distribution
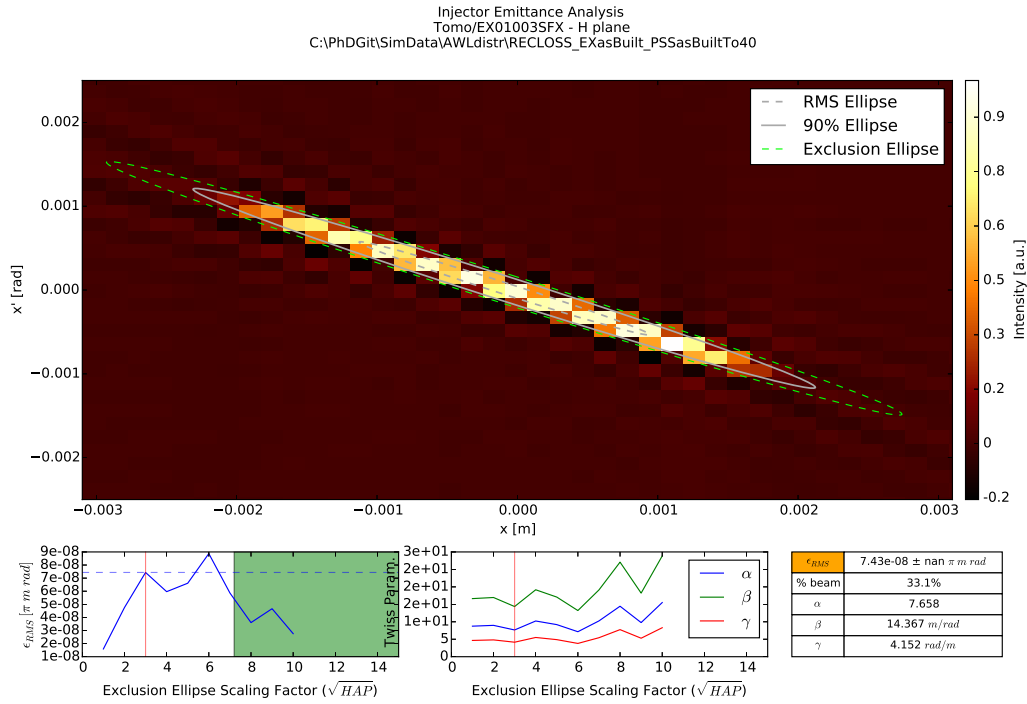
Figure A.5.: SCUBEEx analysis result of the FBP reconstruction using a ramp filter and cubic interpolation
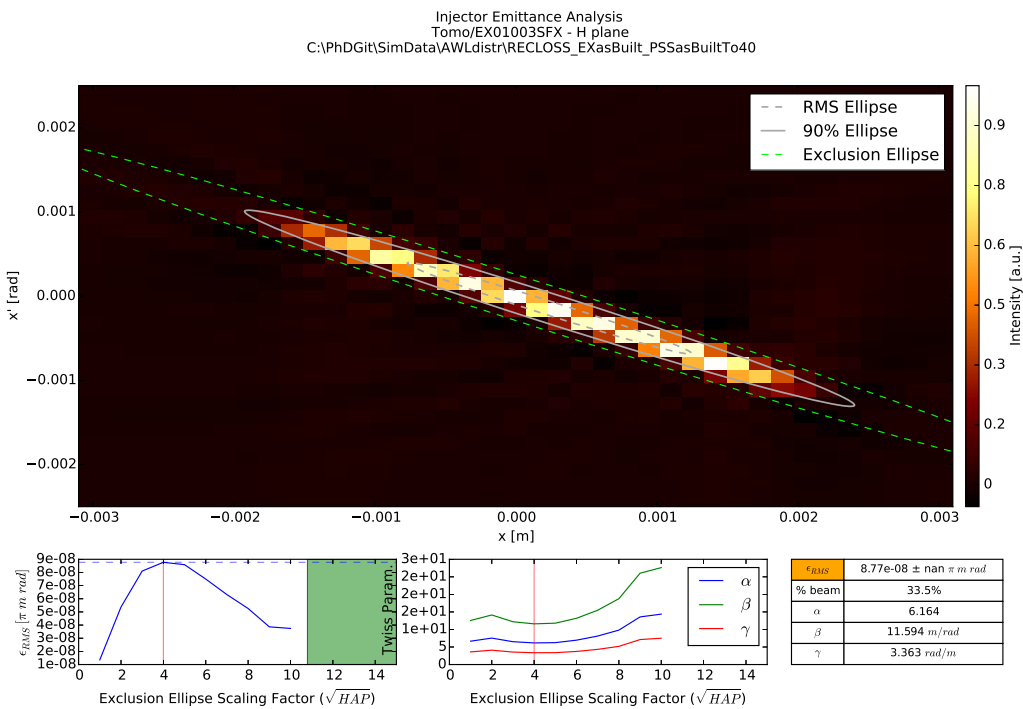
Figure A.6.: SCUBEEx analysis result of the SART reconstruction

(a) CAT1 evaluation (based on MULT) (b) EMT0 evaluation (based on FBP)

Figure A.7.

(a) CAT20 evaluation (based on MULT) (b) EMT10 evaluation (based on FBP)
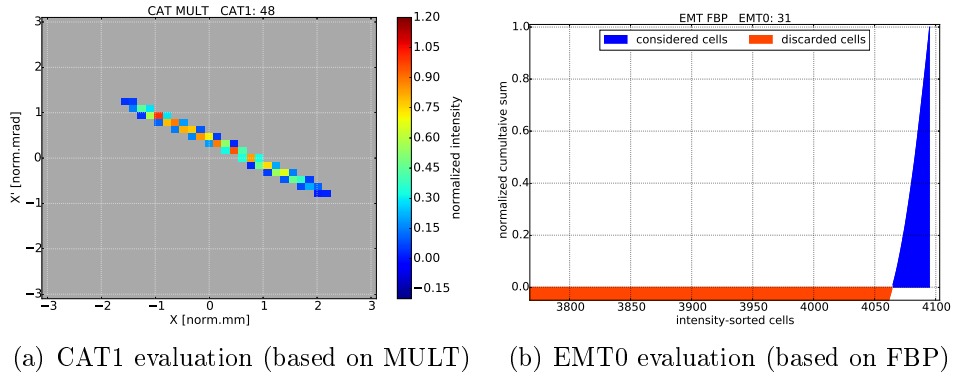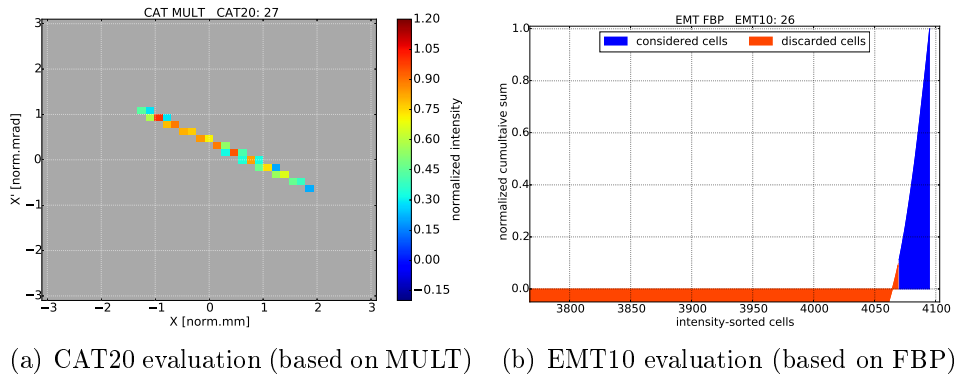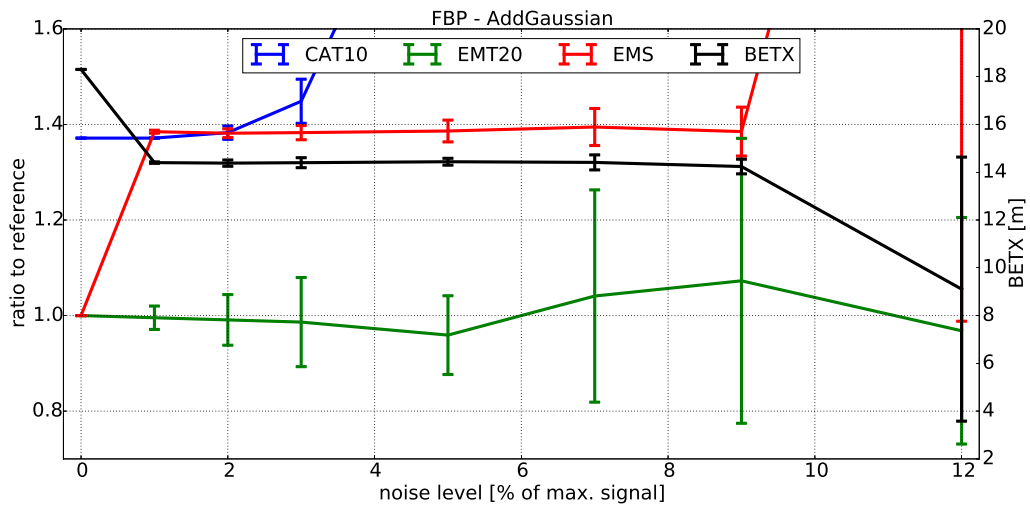
Figure A.8.

Figure A.9.: FBP evaluation parameters for increasing noise amplitudes
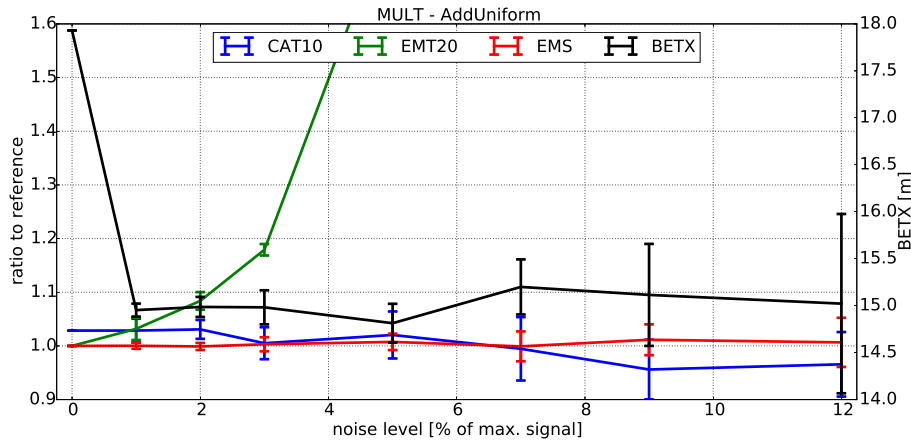
Figure A.10.: MULT evaluation parameters for increasing noise amplitudes
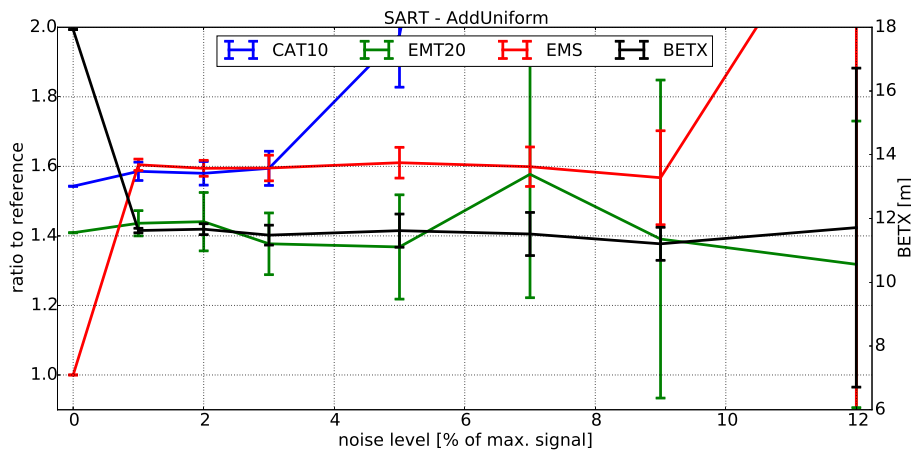
Figure A.11.: SART evaluation parameters for increasing noise amplitudes
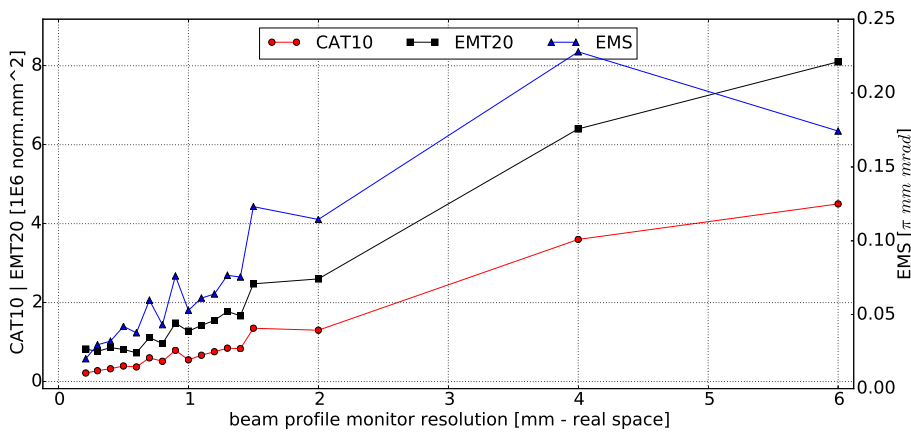
Figure A.12.: Reconstruction evaluation parameters as a function of monitor resolution
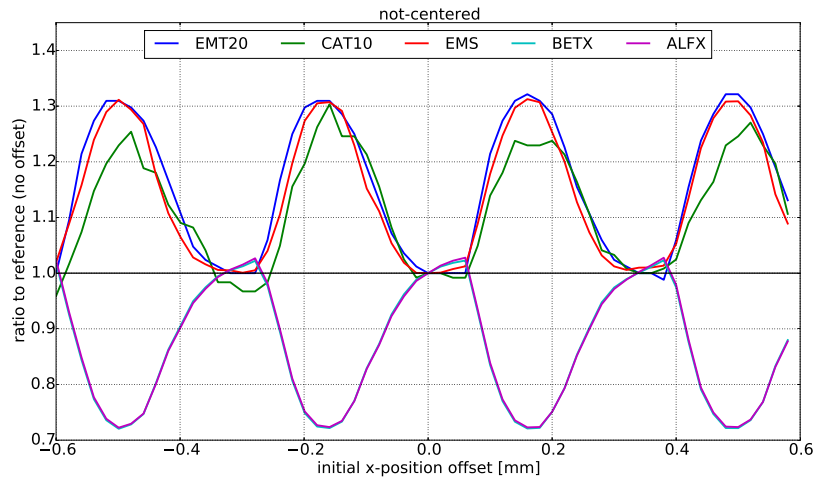
Figure A.13.: Evaluation parameters as a function of bin shift - not centered, resolution 1/3mm

(a) Simulation

(b) Measurement
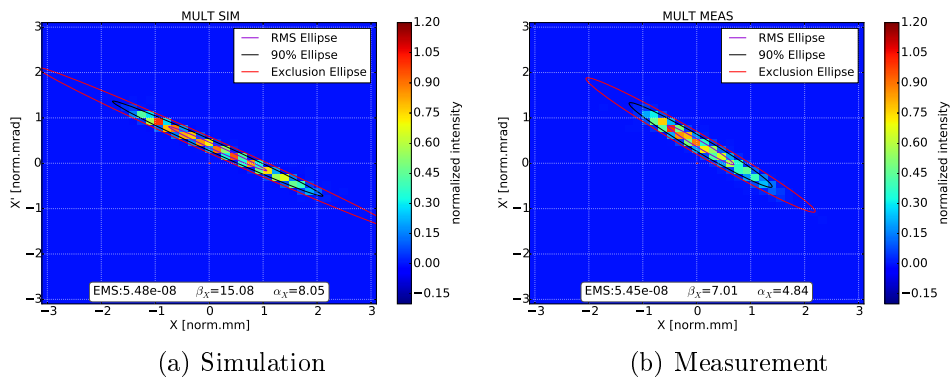
Figure A.14.: Comparison of MULT reconstructed tomograms - EMS analysis
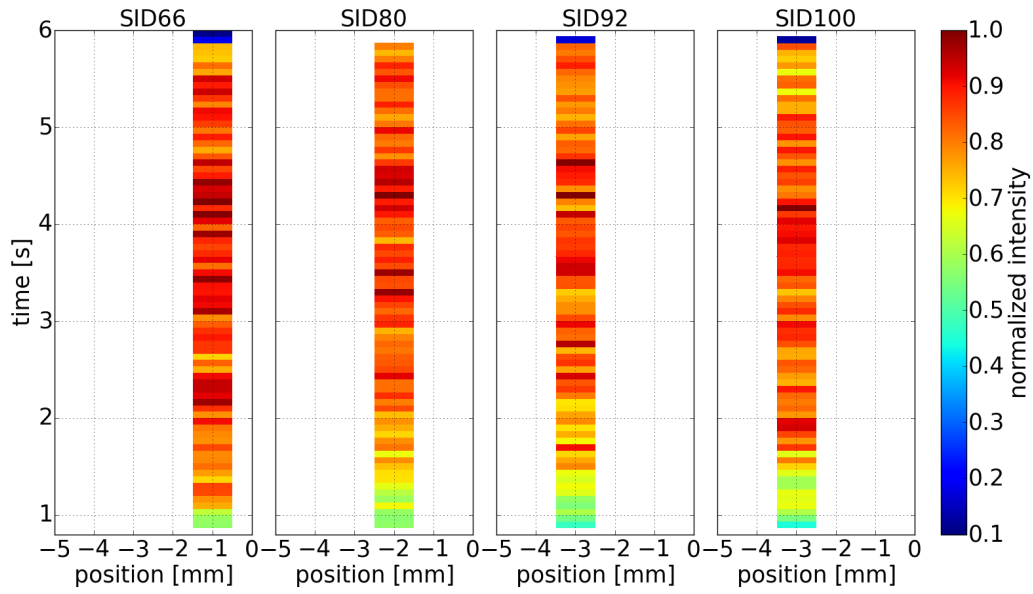
Figure A.15.: Intraspill profiles of four spills on EX01002SFX
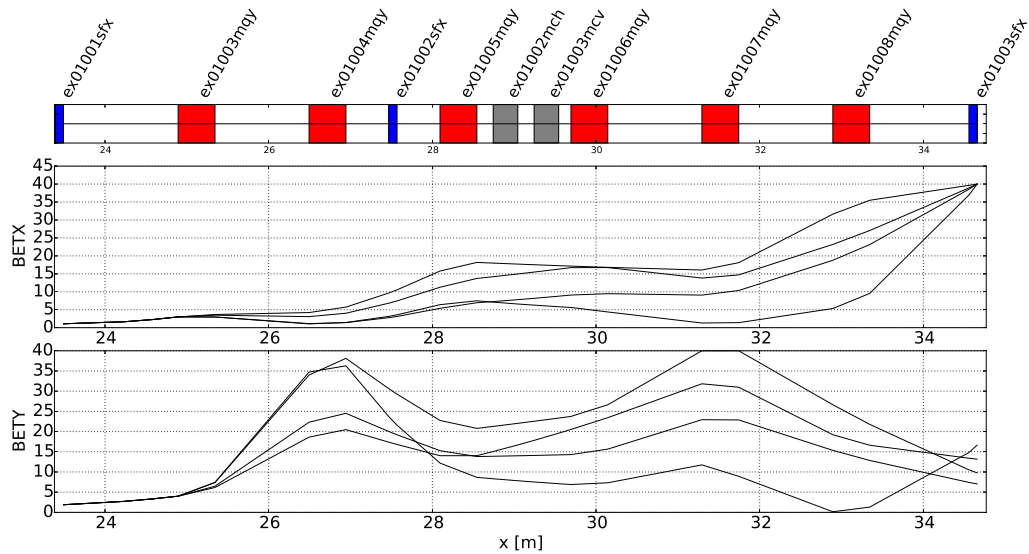
Figure A.16.: Beta functions of 'good' cases (w.r.t. 4.14) inside the PSS module

Bibliography

[1] A. Wastl, M. Benedikt, and A. Garonna, "Tomography of Horizontal Phase Space Distribution of a Slow Extracted Proton Beam in the MedAustron High Energy Beam Transfer Line," in *Proc. 6th International Particle Accelerator Conference (IPAC'15)*, (Richmond, VA, USA), 2015.

[2] Slow Extraction Workshop 2016. `https://indico.gsi.de/event/4496/overview/`. Darmstadt, Germany.

[3] Slow Extraction Workshop 2017. `https://indico.cern.ch/event/639766//`. Geneva, Switzerland.

[4] `http://www.quantumdiaries.org/2012/02/15/the-hidden-face-of-cern//`. Accessed on 19.02.2013.

[5] U. Dorda. personal communication.

[6] G. Feldbauer, "Extraction methods for the MedAustron synchrotron," Master's thesis, Vienna University of Technology, 2011.

[7] M. Palm, *Performance requirements and penumbra optimization of the MedAustron beam delivery system*. PhD thesis, Vienna University of Technology, 2013.

[8] M. Benedikt, *Optical design of a synchrotron with optimisation of the slow extraction for hadron therapy*. PhD thesis, Vienna University of Technology, 1997.

[9] T. U. Munich. `http://zfp.cbm.bgu.tum.de/mediawiki/index.php/Bildrekonstruktionsverfahren_in_der_Computer_Tomographie/`.

[10] T. Kanai, Y. Furusawa, K. Fukutsu, H. Itsukaichi, K. Eguchi-Kasai, and H. Ohora, "Irradiation of mixed beam and design of spread-out bragg peak for heavy-ion radiotherapy," *Radiation Research*, vol. 147, pp. 78–85, 1997.

[11] P. Bryant, M. Benedikt, L. Badano, M. Crescenti, P. Holy, A. Maier, M. Pullia, S. Rossi, and P. Knaus, "Proton-Ion Medical Machine Study (PIMMS), 1," Tech. Rep. CERN-PS-99-010-DI, European Organisation for Nuclear Research CERN, Geneva, Switzerland, 1999.

[12] P. Bryant, M. Benedikt, L. Badano, M. Crescenti, P. Holy, A. Maier, M. Pullia, S. Reimoser, S. Rossi, G. Borri, P. Knaus, F. Gramatica, M. Pavlovic, and L. Weisser, "Proton-Ion Medical Machine Study (PIMMS), 2," Tech. Rep. CERN-PS-2000-007-DR, European Organisation for Nuclear Research CERN, Geneva, Switzerland, 2000.

[13] Centro Nazionale di Adroterapia Oncologica per il trattamento dei tumori. `http://www.cnao.it/`. Pavia, Italy.

[14] Heidelberger Ionenstrahl-Therapiezentrum. `http://www.klinikum.uni-heidelberg.de/`.

[15] Heavy Ion Medical Accelerator in Chiba HIMAC. `http://www.nirs.go.jp/ENG/research/charged_particle/`.

[16] MedAustron. `http://www.medaustron.at/`.

[17] European Organisation for Nuclear Research CERN, *MAD-X User's Guide*, 2002.

[18] M. Benedikt and C. Carli, "Matching to gantries for medical synchrotrons," in *Proc. of the Particle Accelerator Conference (PAC'97)*, (Vancouver, Canada), 1997.

[19] M. Benedikt, "Optics design of the extraction lines for the medaustron hadron therapy centre," *Nuclear Instruments and Methods in Physics Research Section A: Accelerators, Spectrometers, Detectors and Associated Equipment*, vol. 539, no. 1, pp. 25 – 36, 2005.

[20] G. Asova, H. J Grabosch, M. Groß, L. Hakobyan, I. Isaev, Y. Ivanisenko, M. Khojoyan, G. Klemz, M. Krasilnikov, M. Mahgoub, D. Malyutin, A. Oppelt, M. Otevrel, B. Petrosyan, S. Rimjaem, A. Shapovalov, F. Stephan, and G. Vashchenko, "First results with tomographic reconstruction of the transverse phase space at pitz," 01 2011.

[21] C. McKee, P. O'Shea, and J. Madey, "Phase space tomography of relativistic electron beams," *Nuclear Instruments and Methods in Physics Research Section A: Accelerators, Spectrometers, Detectors and Associated Equipment*, vol. 358, no. 1, pp. 264 – 267, 1995.

[22] R. Connolly, R. Michnoff, T. Moore, T. Shea, and S. Tepikian, "Beam profile measurements and transverse phase-space reconstruction on the relativistic heavy ion collider," *Nuclear Instruments and Methods in Physics Research A*, vol. A443, pp. 215–222, 2000.

[23] S. Hancock, M. Lindroos, and S. Koscielniak, "Longitudinal phase space tomography with space charge," *Phys. Rev. ST Accel. Beams*, vol. 3, p. 124202, Dec 2000.

[24] K. M. Hock, M. Ibison, D. Holder, A. Wolski, and B. Muratori, "Beam tomography in transverse normalised phase space," *Nuclear Instruments and Methods in Physics Research Section A-accelerators Spectrometers Detectors and Associated Equipment*, vol. 642, pp. 36–44, 06 2011.

[25] D. Stratakis, R. Kishek, S. Bernal, R. Fiorito, I. Haber, M. Reiser, P. O'Shea, K. Tian, and J. Thangaraj, "Generalized phase-space tomography for intense beams," *Physics of Plasmas*, vol. 17, pp. 056701–056701, 02 2010.

[26] D. Stratakis, R. Kishek, R. Fiorito, K. Tian, I. Haber, P. O'Shea, M. Reiser, and J. Thangaraj, "Time-dependent phase-space characterization of intense charged particle beams," *Phys. Rev. ST Accel. Beams*, vol. 12, 02 2009.

[27] D. Stratakis, R. A. Kishek, H. Li, S. Bernal, M. Walter, B. Quinn, M. Reiser, and P. G. O'Shea, "Tomography as a diagnostic tool for phase space mapping of intense particle beams," *Phys. Rev. ST Accel. Beams*, vol. 9, 2006.

[28] D. Reggiani, M. Seidel, and C. Allen, "Transverse phase-space beam tomography at PSI and SNS proton accelerators," in *Proc. of International Particle Accelerator Conference (IPAC'10)*, (Kyoto, Japan), 2010.

[29] G. Minerbo, "Ment: A maximum entropy algorithm for reconstructing a source from projection data," *Computer Graphics and Image Processing*, vol. 10, pp. 48–68, 05 1979.

[30] C. T. Mottershead, "Maximum entropy tomography," in *Maximum Entropy and Bayesian Methods*, pp. 425–430, Springer Netherlands, 1996.

[31] A. Garonna, F. Farinon, M. Kronberger, T. Kulenkampff, C. Kurfürst, S. Myalski, S. Nowak, L. Penescu, M. Pivi, C. Schmitzer, A. Wastl, F. Osmic, and P. Urschütz, "Status of proton beam commissioning of the medaustron particle therapy accelerator," in *Proceedings of IPAC 2016*, (Busan, Korea), 2016.

[32] M. Pivi, A. D. Franco, F. Farinon, M. Kronberger, C. Kurfürst, S. Myalski, S. Nowak, F. Osmic, C. Schmitzer, A. Wastl, P. Urschütz, and L. Penescu, "Overview and status of the medaustron ion therapy center accelerator," in *Proceedings of IPAC 2017*, (Copenhagen, Denmark), 2017.

[33] C.Schmitzer, L.Adler, A. Franco, F.Farinon, N.Gambino, G.Guidoboni, M.Kronberger, C.Kurfürst, S.Myalski, S.Nowak, M.Pivi, I.Strasik, A.Wastl, and L. Penescu, "Carbon commissioning of the medaustron therapy accelerator," in *Proceedings of IPAC 2018*, (Vancouver, Canada), 2018.

[34] U. Dorda, M. Benedikt, and P.Bryant, "Layout and optics of the medaustron high energy beam transfer line," Tech. Rep. CERN-ATS-2011-075, European Organisation for Nuclear Research CERN, Geneva, Switzerland, 2011.

[35] M. Benedikt and A. Wrulich, "MedAustron - project overview and status," *The Euorpean Physical Journal Plus*, vol. 126, pp. 69–80, 2011.

[36] P. Bryant and K. Johnsen, *The principles of circular accelerators and storage rings*. Cambridge New York: Cambridge University Press, 1993.

[37] H. Wiedemann, *Particle accelerator physics*. Berlin New York: Springer, 2007.

[38] M. Conte and W. MacKay, *An introduction to the physics of particle accelerators*. World Scientific, 2008.

[39] K. Wille, *The physics of particle accelerators : an introduction*. Oxford New York: Oxford University Press, 2000.

[40] L. Yang, S. Lee, X. Huang, and B. Podobedov, "A new code for orbit response matrix analysis," in *Particle Accelerator Conference*, pp. 804 –806, 2007.

[41] CERN Accelerator School. `https://cas.web.cern.ch/`.

[42] U.S. Particle Accelerator School. `http://uspas.fnal.gov/`.

[43] E. Courant and H. Snyder, "Theory of the alternating-gradient synchrotron," *Annals of Physics*, vol. 3, pp. 1 – 48, 1958.

[44] A. Wastl, "Development of the orbit correction procedure and simulations on rf-noise driven slow resonant extraction of medaustron synchrotron," Master's thesis, Vienna University of Technology, 2013.

[45] M. Pullia, *Dynamics of slow extraction and its influence on transfer lines design*. PhD thesis, Université Claude Bernard - Lyon 1, 1999.

[46] Y. Kobayashi and H. Takahashi, "Improvement of the emittance in the resonant ejection," in *Proc. 6th Int. Conf. on High Energy Accelerators*, (Cambridge, Massachusetts, USA), pp. 347–351, 1967.

[47] A. Kak and M. Slaney, *Principles of Computerized Tomographic Imaging*. New York: IEEE Press, 1988.

[48] J. Radon, "Ueber die bestimmung von funktionen durch ihre integralwerte laengs gewisser mannigfaltigkeit," *Berichte über die Verhandlungen der Koeniglich - Saechsischen Akademie der Wissenschaften zu Leipzig*, vol. 69, pp. 262–277, 1917.

[49] R. Gordon, R. Bender, and G.Herman, "Algebraic reconstruction techniques (art) for three-dimensional electron microscopy and x-ray photography," *Journal of theoretical Biology*, vol. 29, pp. 471–481, 1970.

[50] R. Gordon, R. Bender, and G.Herman, "Angenaeherte aufloesung von systemen linearer gleichungen," *Bulletin International de l'Académie Polonaise des Sciences et des Lettres, Serie A*, vol. 35, pp. 355–357, 1937.

[51] A. Kak and A. Andersen, "Simultaneous slgebraic reconstruction technique (sart): a superior implementation of the art algorithm," *Ultrasound Imaging*, vol. 6, pp. 81–94, 1084.

[52] E. Oliveira, S. Melo, C. Dantas, D. Vasconcelos, and L.F.Cadiz, "Comparison among tomographic reconstruction algorithms with a limited data," in *Proceedings of INAC 2011*, (Belo Horizonte, Brazil), 2011.

[53] European Organization for Nuclear Research CERN. `http://www.cern.ch/`. Geneva, Switzerland.

[54] Methodical Accelerator Design, version 5.03.07. `http://madx.web.cern.ch/madx/`.

[55] python, "version 3.4.1." `http://www.python.org/`.

[56] skimage, "version 0.10.1." `http://scikit-image.org/`.

[57] T. Chai and R. R. Draxler, "Root mean square error (rmse) or mean absolute error (mae)? – arguments against avoiding rmse in the literature," *Geoscientific Model Development*, vol. 7, pp. 1247–1250, 2014.

[58] M. Stockli and R. F. Welton and R. Keller and A. P. Letchford and R. W. Thomae and J. W. G. Thomason, "Accurate Estimation of the RMS Emittance from Single Current Amplifier Data," *AIP Conference Proceedings*, vol. 639, no. 1, pp. 135–159, 2002.

[59] L. Bellan, M. Comunian, E. Fagotti, and A. Pisent, "Scubeex-ghostbuster algorithm for ghost infested emittance measurements," tech. rep., INFN, Laboratori Nazionali di Legnaro, Legnaro, Italy.

[60] R. Keller, J. Sherman, and P. Allison, "Use of a minimum-ellipse criterion in the study of ion-beam extraction systems," *IEEE Transactions on Nuclear Science*, vol. 32, no. 5, 1985.

[61] L. Bellan, *Beam Dynamics Characterization of the IFMIF/EVEDA RFQ Input Beam*. PhD thesis, Università degli Studi di Padova, Padova, Italy, 2017.

[62] B. Bazak and L. Weissman, "Minimum ellipse emittance analysis with SCUBEEx code," *Journal of Instrumentation*, vol. 3, no. 02, 2008.

[63] A. Kerschbaum, "Development and implementation of a new emittance analysis application for the medaustron injector complex," tech. rep., Atominstitut of the Technical University of Vienna, Vienna, Austria, 2018.

[64] L. Adler, "Implementation of emittance and transmission measurement and analysis procedures along the MedAustron accelerator," Master's thesis, Vienna University of Technology, 2019.

[65] A. Wastl, M. Hager, and M. Regodic, "Operational Applications - a Software Framework Used for the Commissioning of the MedAustron Accelerator," in *Proc. 6th International Particle Accelerator Conference (IPAC'15)*, (Richmond, VA, USA), 2015.

[66] A. Wastl, A. Garonna, T. Kulenkampff, and S. Nowak, "PACMAN - the MedAustron Measurement Data Analysis Framework," in *Proc. of International Particle Accelerator Conference (IPAC'16)*, (Busan, Korea), 2015.

[67] C. Kurfürst. personal communication.

[68] C. Kurfürst *et al.*, "HEBT Commissioning for Horizontal Beamline Proton Treatments at MedaAustron," in *Proc. of International Particle Accelerator Conference (IPAC'16)*, (Busan, Korea), 2016.

DI DI Alexander WASTL

Date of birth	June 12th, 1984
Place of birth	Klagenfurt, Austria
Nationality	Austria
Address	Muldenweg 14, 9170 Ferlach, Austria

Employment

2013 – Present

EBG MedAustron, Wiener Neustadt, Austria

<u>Physicist</u> in the Accelerator and Beam Physics group with focus on simulation studies, operation and commissioning procedures as well as student supervision

<u>Software developer</u> responsible for the measurement data analysis framework (in python) as well as product coordinator for the measurement acquisition suite

<u>Beam commissioner</u> responsible of optimization of the accelerator and beam quality as well as the implementation of the settings in the medical product according to the QMS SOPs

<u>Project lead</u> for commissioning a new clinically used beam modality including time line and resource allocation responsibility, requirement engineering and project controlling/reporting

2012 – 2013

European Organization for Nuclear Research CERN
Geneva, Switzerland; PhD-student

2000 – 2010

Miscellaneous jobs during summer time in various companies including Paropa Computer Point, Klagenfurt Airport Inc., Arsenal Research as well as a dive center

Education

2012 – 2020

PhD Program "Technical Sciences Technical Physics"
Vienna University of Technology, Austria; particle accelerator physics, carried out at CERN and at MedAustron

2010 – 2013

Master Program "Biomedical Engineering"
Vienna University of Technology, Austria; "Development of the orbit correction procedure and simulations on rf-noise driven slow

resonant extraction of MedAustron synchrotron", carried out at CERN within the MedAustron project, **Pass with distinction**

2010 – 2011	**Master Degree "Physical Energy and Measurement Engineering"**, Vienna University of Technology, Austria; "Multielement and spacial distribution analysis of gunshot residues using TXRF", ISO17025 cert. lab, **Pass with distinction**
2010	**Bachelor Degree "Technical Physics"** Vienna University of Technology, Austria
2003 – 2004	Military service Austrian Armed Forces
1998 – 2003	Higher technical school HTL, Klagenfurt, Austria Graduation with honors
1996 – 1998	La Cima Middle School, Tucson, Arizona, USA (eleven months in total)

Extracurricular Education

2017	**United States Particle Accelerator School**, 'Accelerator physics, rating: outstanding, Rohnert Park, California, USA
2012/2016	**CERN Accelerator School**, Granada, Spain and Vienna, Austria
2013	**Radiation Protection Training**, Courses 'Basic' and 'Sealed radioactive sources', Seibersdorf Laboratories
2013	**Participation in the European Forum Alpbach 2013** BMVIT grant 'talente@alpbach'
2011 – 2012	**Participant in TUtheTOP** – the high potential program of the Vienna University of Technology

Skills and Qualifications

Languages	German (mother tongue), English (fluent) French (basic), Spanish (basic)
Computing	Windows, Linux, Office, LaTeX
Programming	Python, MADx, LabView
Economy	European Business Competence Licence A
Red Cross	Squad leader, EMT (Notfallsanitäter)

Interests

Sports	ski touring, mountain biking, sailing
Travelling	longer period of residence in USA, Costa Rica, France/Switzerland
EMS	Austrian Red Cross - Emergency Medical Service